

PHYSICS FROM LOW FREQUENCY OBSERVATIONS OF NEARBY GALAXIES

DISSERTATION

ZUR ERLANGUNG DES DOKTORGRADES
AN DER FAKULTÄT FÜR MATHEMATIK, INFORMATIK UND NATURWISSENSCHAFTEN
FACHEREICH PHYSIK
DER UNIVERSITÄT HAMBURG

VORGELEGT VON

LOVORKA GAJOVIĆ

HAMBURG
2025

Gutachter der Dissertation: Prof. Dr. Marcus Brüggem
Dr. Francesco de Gasperin

Zusammensetzung der Prüfungskommission: Prof. Dr. Marcus Brüggem
Dr. Francesco de Gasperin
Prof. Dr. Robi Stefan Banerjee
Prof. Dr. Dieter Horns
Prof. Dr. Jochen Liske

Vorsitzender der Prüfungskommission: Prof. Dr. Jochen Liske

Datum der Disputation: 10. April 2025

Vorsitzender des Fach-Promotionsausschusses PHYSIK: Prof. Dr. Wolfgang J. Parak

Leiter des Fachbereichs PHYSIK: Prof. Dr. Markus Drescher

Dekan der Fakultät MIN: Prof. Dr.-Ing. Norbert Ritter

Declaration on oath

I hereby declare and affirm that this doctoral dissertation is my own work and that I have not used any aids and sources other than those indicated.

If electronic resources based on generative artificial intelligence (gAI) were used in the course of writing this dissertation, I confirm that my own work was the main and value-adding contribution and that complete documentation of all resources used is available in accordance with good scientific practice. I am responsible for any erroneous or distorted content, incorrect references, violations of data protection and copyright law or plagiarism that may have been generated by the gAI.

Hamburg, den 24.02.2025

Lovorka Gajović

A handwritten signature in blue ink, reading "L. Gajović", with a horizontal line underneath the name.

Zusammenfassung

Diese Arbeit konzentriert sich auf zwei Möglichkeiten, wie wir die niederfrequente Synchrotronstrahlung nutzen können, um mehr über die physikalischen Prozesse in nahen Galaxien zu erfahren. Das LOw-Frequency ARray (LOFAR) wird in dieser Arbeit als primäres Beobachtungsinstrument eingesetzt, da es über einzigartige Niederfrequenzfähigkeiten, ein grosses Gesichtsfeld, hohe Empfindlichkeit und Winkelauflösung verfügt.

Der erste Teil dieser Arbeit untersucht die Abflachung des Radiospektrums bei niedrigen Frequenzen in Spiralgalaxien. Ein gründliches Verständnis der Radioemission bei niedrigen Frequenzen ist wichtig, wenn wir Radiobeobachtungen nutzen wollen, um die Sternentstehung in Galaxien zu verfolgen. Die beobachteten Objekte sind: die Galaxie M 51 als Ganzes und die Sternentstehungsgebiete (H II-Regionen) der Galaxie M 101. Zur Analyse von M 51 verwende ich Intensitätskarten der Radiokontinuumsstrahlung zwischen 54 und 8350 MHz in acht verschiedenen Frequenzbändern. Beobachtungen mit LOFAR bei 54 MHz waren entscheidend, weil die Abflachung bei höheren Frequenzen nicht vorhanden ist. Ich finde keine räumliche Korrelation zwischen der Abflachung und dem ionisierten interstellaren Medium (ISM), was zu erwarten wäre, wenn die Abflachung durch Absorption des frei-frei Strahlungsprozesses verursacht wird. Stattdessen finde ich eine Korrelation mit dem neutralen ISM, was darauf hindeutet, dass Ionisationsverluste durch kosmische Strahlung (cosmic rays, CR) eine wichtige Rolle spielen, möglicherweise neben inverse Bremsstrahlung. In M 101 analysiere ich nur die riesigen H II-Regionen in vier Frequenzbändern zwischen 54 und 4850 MHz. Ich finde eine signifikante Abflachung bei niedrigen Frequenzen, die mit Modellen der inverse Bremsstrahlung in den Zentren der meisten ausgewählten H II-Regionen angepasst werden kann. Die Abflachung kann nur in einem kleinen Bereich im Zentrum der H II-Region nachgewiesen werden, was hochauflösende Radiobeobachtungen erfordert. Dies sind die ersten Nachweise der niederfrequenten Abflachung in durchschnittlichen Spiralgalaxien.

Der zweite Teil dieser Arbeit befasst sich mit der Suche nach annihilierender Dunkler Materie (DM), insbesondere nach schwach wechselwirkenden massiven Teilchen (weakly interacting massive particles, WIMPs). Ich beobachte sphäroidische Zwerggalaxien (dwarf spheroidal galaxies, dSph), in denen WIMPs annihilieren sollten und die dabei entstehenden Teilchen Synchrotronstrahlung im Radioband emittieren, wenn in dSph ausreichend starke Magnetfelder existieren. Da kein Signal entdeckt wird, verwende ich das Wissen über die CR-Ausbreitung und die erwartete Synchrotronstrahlung, um den WIMP-Annihilationsquerschnitt zu begrenzen. Ich verwende LOFAR-Beobachtungen von sechs dSph bei 150 MHz. Da das Magnetfeld und der Diffusionskoeffizient in dSph unsicher sind, konstruiere ich drei Szenarien mit unterschiedlichen Werten dieser Parameter: ein optimistisches, ein mittleres und ein pessimistisches Szenario. Die besten Grenzen des mittleren Szenarios schließen den thermischen Reliktquerschnitt von WIMPs ($\langle\sigma v\rangle \approx 2,2 \times 10^{-26} \text{ cm}^3 \text{ s}^{-1}$) unterhalb von 20 GeV, und die besten Grenzwerte des optimistischen Szenarios schließen thermische WIMPs unterhalb von 70 GeV aus. Meine mittleren Grenzen sind konkurrenzfähig im Vergleich zu den *Fermi*-LAT-Grenzen aus γ -Strahlenbeobachtungen mehrerer Zwerggalaxien. In diesem Teil zeige ich, wie gut niederfrequente Radiobeobachtungen die DM-Eigenschaften einschränken und wie Radiosuchen andere DM-Suchen ergänzen können.

Zusammenfassend kann man sagen, dass ich niederfrequente Radiobeobachtungen verwende,

um Ergebnisse zu erzielen, die von der grundlegenden Frage der Dunklen Materie bis hin zu der sehr spezifischen Frage der Sternentstehung in Galaxien reichen. Die Synchrotronstrahlung von CR steht im Mittelpunkt dieser Arbeit, und ich untersuche Abweichungen davon, wie sie bekanntermaßen in Galaxien erzeugt wird. Die Beobachtung von nahe gelegenen Galaxien bedeutet, dass ich mit einer hohen physikalischen Auflösung beobachten kann und ermöglicht es, bisher unbekannte Effekte zu unterscheiden und zu entdecken. In Zukunft werden das LOFAR2.0-Update, einschließlich eines umfangreichen DM-Suchprogramms, und neue theoretische Modelle zu einem besseren Verständnis von CR in Galaxien führen, unabhängig davon, ob sie bei der Sternentstehung oder bei der DM-Annihilation entstehen.

Abstract

This thesis focuses on two ways we can use the low-frequency synchrotron signal to learn about physical processes in nearby galaxies. The LOw-Frequency ARray (LOFAR) is used as the primary observational tool in this thesis, because of its unique low-frequency capabilities, wide field of view, high sensitivity and angular resolution.

The first part of this thesis studies the flattening of the radio spectrum at low frequencies in spiral galaxies. A thorough understating of radio emission at low frequencies is important if we want to use radio observations to trace star formation in galaxies. I have two observational targets: the galaxy M 51 as a whole and the star-forming (H II) regions of the galaxy M 101. To analyse M 51, I use radio continuum intensity maps between 54 and 8350 MHz at eight different frequency bands. LOFAR observations at 54 MHz were crucial because the flattening is not present at higher frequencies. I do not find any spatial correlation between the flattening and ionised interstellar medium (ISM), which is expected if the flattening is caused by free–free absorption. Instead, I find a correlation with the neutral ISM, which suggests that cosmic ray (CR) ionisation losses play an important role, possibly alongside free–free absorption. In M 101, I analyse only the giant H II regions at four frequency bands between 54 and 4850 MHz. I find a significant low-frequency flattening that can be fitted with free–free absorption models at the centres of most selected H II regions. The flattening can be detected only in a small area at the centre of the H II region, which requires high resolution radio observations. These are the first detections of the low-frequency flattening in average spiral galaxies.

The second part of this thesis is the search for annihilating dark matter (DM), specifically weakly interacting massive particles (WIMPs). I observe dwarf spheroidal galaxies (dSph) in which WIMPs should annihilate and the particles produced in this annihilation emit synchrotron radiation in the radio band, if strong enough magnetic fields exist in dSph. Since no signal is detected, I use the knowledge of CR propagation and expected synchrotron emission to put limits on the WIMP annihilation cross-section. I use LOFAR observations of six dSph at 150 MHz. Because the magnetic field and diffusion coefficient in dSph is uncertain, I construct three scenarios with different values of those parameters: optimistic, intermediate, and pessimistic scenario. The best limits from the intermediate scenario exclude the thermal relic cross section of WIMPs ($\langle\sigma v\rangle \approx 2.2 \times 10^{-26} \text{ cm}^3 \text{ s}^{-1}$) below 20 GeV, and the best limits from the optimistic scenario exclude thermal WIMPs below 70 GeV. My intermediate limits are competitive compared to the *Fermi*–LAT limits from γ -ray observations of multiple dwarf galaxies. In this part, I show the power of low frequency radio observations in constraining DM properties and how radio searches can complement other DM searches.

In summary, I use low frequency radio observations to produce results spanning from the fundamental question of dark matter to the highly specific question of star formation in galaxies. Synchrotron emission by CRs is at the centre of this work and I explore deviations from how it is known to be produced in galaxies. Observing nearby galaxies means that I can observe with a high physical resolution and makes it possible to distinguish and detect previously unknown effects. In the future, the LOFAR2.0 update, including a large DM search program, and new theoretical models will lead to better understanding of CRs in galaxies, whether they are produced in star formation or DM annihilation.

List of publications

This thesis is partly based on (but does not include all of) the following publications:

First author publications

- **Gajović, L.**, Heesen, V., Brüggén, M., Edler, H. W., Adebahr, B., Pasini, T., de Gasperin, F., Basu, A., Weżgowiec, M., Horellou, C., Bomans, D.J., Dénes, H., Vohl, D. 2025. *The low-frequency flattening of the radio spectrum of giant H II regions in M 101*. Accepted to A&A; arXiv:2502.08713. [Gajović et al. 2025]
- **Gajović, L.**, Adebahr, B., Basu, A., Heesen, V., Brüggén, M., de Gasperin, F., Lara-Lopez, M. A., Oonk, J. B. R., Edler, H. W., Bomans, D. J., Paladino, R., Garduño, L. E., López-Cruz, O., Stein, M., Fritz, J., Piotrowska, J., Sinha, A. 2024. *A spatially resolved radio spectral study of the galaxy M 51*. A&A, 689, A68. [Gajović et al. 2024]
- **Gajović, L.**, Welzmüller F., Heesen V., de Gasperin F., Vollmann M., Brüggén M., Basu A., Beck R., Schwarz D. J., Bomans D. J., Drabent A. 2023. *Weakly interacting massive particle cross section limits from LOFAR observations of dwarf spheroidal galaxies*. A&A, 673, A108. [Gajović et al. 2023]

Publications with major contributions

- Vollmann, M., Welzmüller, F., **Gajović, L.** 2024. *diffSph: a Python tool to compute diffuse signals from dwarf spheroidal galaxies*. JCAP, 2024, 046. [Vollmann et al. 2024]
- Erceg, A., Jelić, V., Haverkorn, M., **Gajović, L.**, Hardcastle, M., Shimwell, T. W., Tasse, C. 2024. *Faraday tomography of LoTSS-DR2 data. III. Revealing the Local Bubble and the complex of local interstellar clouds in the high-latitude inner Galaxy*. A&A, 688, A200 [Erceg et al. 2024]

Co-author publications

- Heesen, V., Wiegert, T., Irwin, J., Crocker, R., Kiehn, A., Li, J. T., Wang, Q. D., Stein, M., Dettmar, R. -J., Soida, M., Henriksen, R., **Gajović, L.**, Yang, Y., Brüggén, M. 2024. *CHANGES: XXXIII. A 20 kpc radio bubble in the halo of the star-forming galaxy NGC 4217*. A&A, 691, A273. [Heesen et al. 2024b]
- Edler, H.W., Roberts, I. D., Boselli, A., de Gasperin, F., Heesen, V., Brüggén, M., Ignesti, A., **Gajović, L.** 2024. *ViCTORIA project: The LOFAR-view of environmental effects in Virgo Cluster star-forming galaxies*. A&A, 683, A149. [Edler et al. 2024]
- Heesen, V., de Gasperin, F., Schulz, S., Basu, A., Beck, R., Brüggén, M., Dettmar, R. J., Stein, M., **Gajović, L.**, Tabatabaei, F. S., Reichherzer, P. 2023. *Diffusion of cosmic-ray electrons in M 51 observed with LOFAR at 54 MHz*. A&A, 672, A21. [Heesen et al. 2023]

Contents

1	Introduction	1
1.1	Aims of this thesis	2
1.2	Nearby galaxies in the context of radio observations	2
1.2.1	Interstellar medium	3
1.2.2	Magnetic fields in galaxies	4
1.2.3	The far-infrared–radio continuum correlation	5
1.2.4	H II regions	6
1.2.5	Dwarf spheroidal galaxies	6
1.3	Radio emission in galaxies	7
1.3.1	Cosmic rays and synchrotron emission	7
1.3.2	Free–free emission and absorption	10
1.3.3	Cosmic ray ionisation losses	11
1.4	Dark matter	12
1.4.1	Weakly interacting massive particles (WIMPs)	13
1.4.2	Search for WIMPs in dwarf spheroidal galaxies with radio telescopes	17
1.5	Radio-interferometry	19
1.5.1	LOFAR	19
1.5.2	GMRT	20
1.5.3	Apertif	20
1.6	Outline of this thesis	21
2	A spatially resolved radio spectral study of the galaxy M51	23
2.1	Introduction	24
2.2	Data handling	26
2.2.1	Observations with the Giant Metrewave Telescope	26
2.2.2	Archival radio continuum observations	27
2.2.3	Integral field unit (IFU) spectroscopy	29
2.3	Data analysis	29
2.3.1	Integrated spectrum	29
2.3.2	Separation of thermal and synchrotron emission	30
2.3.3	Spiral arm, inter-arm, and galaxy core regions	33
2.3.4	Non-thermal radio spectral index and curvature	33
2.3.5	Low- and high-frequency non-thermal radio spectral indices	37
2.4	Spectral index flattening and low-frequency turnovers	37
2.4.1	Cosmic-ray radiation losses	37
2.4.2	Synchrotron self-absorption	39
2.4.3	Thermal free–free absorption	39
2.4.4	Ionisation losses	43
2.5	Summary and conclusions	45

3	The low-frequency flattening of the radio spectrum of giant H II regions in M 101	49
3.1	Introduction	49
3.2	Data	52
3.2.1	LOFAR LBA observations	52
3.2.2	Apertif observations	52
3.2.3	Other radio continuum data	54
3.3	Data preparation	55
3.3.1	Data validation	56
3.3.2	H II region selection	57
3.4	Results	59
3.4.1	Spectral index maps between 54 and 144 MHz	59
3.4.2	SEDs of H II regions and fits	61
3.5	Discussion	64
3.5.1	Comparison to other EM tracers	64
3.5.2	Turnover localisation	65
3.5.3	NGC 5447 at low radio frequencies	66
3.5.4	Implication for spectral flattening and radio–FIR correlation	67
3.6	Conclusions	68
4	Weakly interacting massive particle cross section limits from LOFAR observations of dwarf spheroidal galaxies	71
4.1	Introduction	72
4.2	Dark matter calculations	73
4.2.1	Cosmic ray injection	73
4.2.2	Cosmic ray diffusion	74
4.2.3	Model scenarios	75
4.2.4	Diffusion regimes	75
4.2.5	Synchrotron signal occurrence	76
4.3	Methodology	77
4.3.1	LoTSS observations	77
4.3.2	Reimaging the LoTSS data	78
4.3.3	Calculation of the cross-section upper limits	79
4.3.4	Stacking	79
4.4	Results	81
4.4.1	Individual limits	81
4.4.2	Stacked limits	85
4.4.3	Systematic uncertainties	86
4.5	Discussion and conclusions	88
5	Conclusion and Outlook	91
5.1	Future prospects	92
6	Acknowledgments	95
7	Bibliography	97
A	Thermal subtraction	111

B	Point spectra	113
C	Mask for the integrated spectrum	115
D	Archival integrated flux density measurements for M 101	117
E	Spectral index error map	119
F	Results for the individual galaxies	121
	F.1 Radial intensity profiles	121
	F.2 Fitting plots	122
G	Reimaging parameters	123
H	Stacked limits excluding the galaxy Willman I	125

Contents

1 Introduction

Our lives and the lives of all creatures on Earth are possible because of the Sun, our nearest star. The Sun was formed in the same way as other stars within our Galaxy and outside it. Interstellar clouds collapsed under the effect of gravity, a protostellar disc was formed and once the central density was high enough to support nuclear fusion, the star was born. We are still working towards understanding this process fully and how it is affected by gas hydrodynamics, magnetic fields, supernova feedback and the galactic environment.

A good way to explore star formation is to look at different galaxies and to determine how their parameters affect star formation. In order to do that, we first need a reliable way to measure the star formation rate. This is usually done with optical or infrared observations which are affected by absorption. Absorption is a large source of uncertainty but here is a possibility to use radio emission as an alternative tracer of star formation. Massive stars end their life in supernova explosions and emit high-energy cosmic rays (CRs) which produce synchrotron emission in the magnetic field of galaxies. Therefore, more radio synchrotron emission correlates with higher star formation and we remove a source of uncertainty because radio emission is not affected by extinction.

At very low frequencies (below 100 MHz), however, the correlation between radio emission and star formation breaks down. The radio emission at those frequencies is significantly reduced in some galaxies producing the so-called low-frequency flattening or turnover. We are working on understanding why this happens and new results from radio-interferometers can enable us to do exactly that. In Sect. 1.3 we go into details of emission mechanisms at low radio frequencies and possible mechanisms behind the low-frequency flattening. In Ch. 2 we directly explore the low-frequency effects on the scale of a full galaxy by observing the galaxy M 51. In Ch. 3 we explore this in ionised H II regions of the galaxy M 101, which are formed by hot young stars and present an extreme environment.

Going back to more fundamental questions, the formation of galaxies or stars would not be possible without dark matter (DM). Without it the universe would be mostly uniform with small density perturbations. Ordinary baryonic matter is attracted by DM overdensities, therefore a significant amount of DM must exist in the universe to make the formation of galaxies possible (Balazs et al. 2024). Dark matter is still mostly a mystery. It interacts gravitationally, so we have a fairly good understanding of its distribution and we know that it makes up 80% of the matter in the universe. However, no interaction with other fundamental forces (electromagnetic, weak and strong nuclear) has ever been observed. But why would we even want to search for other interactions? Looking at baryonic matter, it is clear that we were able to learn what matter is by constructing a comprehensive theory of fundamental particles and their interaction: The Standard model of Particle Physics. If we only knew about the gravitational interactions, we would not be able to understand the interactions necessary for the formation of basic chemical elements in the universe, for stars to emit light, for molecules to form and eventually life to develop on Earth. Therefore, we have to search for non-gravitational interactions of DM in order to learn its fundamental nature.

Starting from the Standard Model, we can construct theories that extend the model and at the same time explain the interaction of DM with baryonic matter. In Sect 1.4, I go more in depth about the overwhelming evidence for DM existence, proposed DM candidates and searches for those candidates. In Ch. 4, I conduct a specific search for DM using state-of-the-art radio interferometers.

1.1 Aims of this thesis

The aim of this thesis is to utilize the very low-frequency observations to discover new physics, specifically looking at nearby galaxies. Two main topics are covered: First, I study the low-frequency radio emission of spiral galaxies. This is important for the understanding the correlation between radio continuum emission and star formation. Two different targets are observed: the spiral galaxy M 51 as a whole and the giant H II regions of the galaxy M 101.

The second topic is a radio search for a particular DM candidate called Weakly Interacting Massive Particles (WIMPs). The goal of this part is to put the limits on the self-annihilation cross section of WIMPs with a recently developed method that uses radio observations at low frequencies.

1.2 Nearby galaxies in the context of radio observations

When thinking of galaxies, people usually imagine the well-known optical images of galaxies, that essentially show the light from the billions of stars. However, stars comprise less than 10% of the total mass in galaxies (Read & Trentham 2005). The largest contribution to the mass of galaxies comes from DM. This will be part of Chapter 4 of this thesis. We know that galaxies emit in the entire electromagnetic spectrum, from the high-frequency gamma-rays down to the low-frequency radio waves. Each wavelength reveals their own physical constituents and processes. In this thesis, I will focus on the low-frequency radio waves (with frequencies below 150 MHz), which have only recently become accessible with the latest generation of digital radio interferometers. Here, I have mostly made use of the LOw-Frequency ARray (LOFAR; van Haarlem et al. 2013) that spreads across several European countries (see Sec. 1.5.1). Low-frequency radio waves are produced by relativistic electrons in the magnetic fields that pervade galaxies (see Sec. 1.3.1). These relativistic electrons, also called cosmic ray electrons (CRes), are accelerated by the explosions of massive stars at the end of their lifetime, so-called supernovae, which thus relate to star formation which mostly occurs in spiral galaxies.

Spiral galaxies usually form stars at rates of the order of magnitude of one solar mass per year (M_{\odot}/yr) (Bendo et al. 2002; Elia et al. 2022). Extreme starburst galaxies, however, can have significantly higher star formation rates (SFR), reaching up to $100 M_{\odot}/\text{yr}$ (see e.g. Dopita et al. 2002). There are numerous ways of measuring the SFR. First, continuum observations in specific spectral band such as near- or far-ultraviolet (UV), multiple different infrared (IR) bands, X-ray or radio. Second, observations of nebular recombination spectral lines such as $H\alpha$ and forbidden lines such as $O\text{II}$. Third, observations of spectral features such as the colour or more specifically the spectral break at 4000 \AA (Poggianti & Barbaro 1997). Fourth, in nearby galaxies young stellar objects (YSOs) can be counted directly in order to measure the SFR. Finally, information from multiple tracers can be combined to exploit the complementary strengths of different wavelengths. For reviews on the SFR measurements see Kennicutt (1998) and Kennicutt & Evans (2012). Observations at different frequencies trace star formation on different timescales so combining them makes it possible to study the star formation history in galaxies (Förster Schreiber et al. 2003; Boquien et al. 2014).

Studies on nearby galaxies are particularly important because they enable us to study processes inside galaxies at very high angular resolution and study low-luminosity components that cannot be detected in distant galaxies. We specifically study two well-known galaxies, M 51 (also known as Whirlpool galaxy or NGC 5194) and M 101 (also known as Pinwheel galaxy or NGC 5457). They are located in the northern sky, close to the constellation Ursa Major, at distances of 8.5 Mpc (McQuinn et al. 2016) and 6.64 Mpc (Hiramatsu et al. 2023), respectively. The locations of the two galaxies

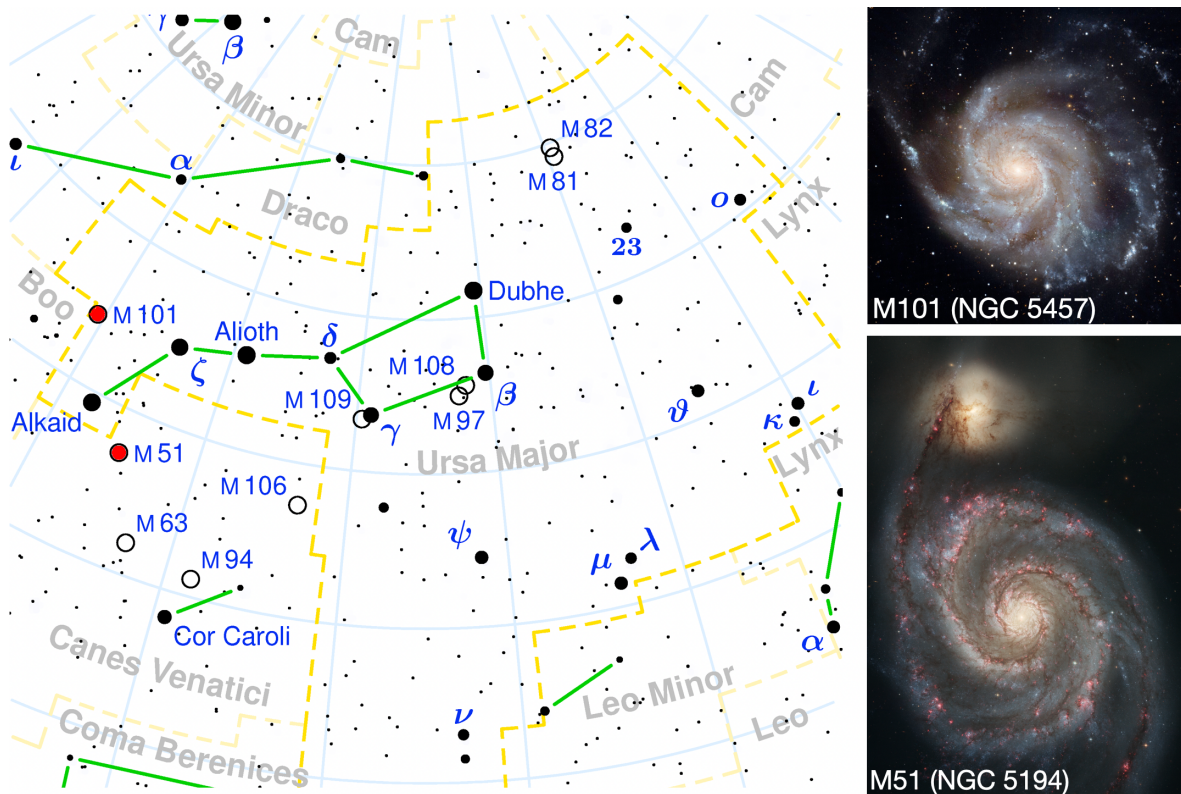


Figure 1.1: Constellation Ursa Major (left; Bronger 2003) and optical images of the two galaxies we study at radio frequencies: M101 (top right; NASA et al. 2009) and M51 (bottom right; NASA et al. 2005).

on the sky and their optical images are shown in Fig. 1.1. Both of those galaxies are in the face-on orientation, which means that we are seeing their discs from "above" instead of "from the side". This makes it easy to distinguish the spiral arms, inter-arm regions and the galactic centre. These galaxies were detected at radio frequencies in the First Cambridge Catalogue of Radio Sources (1C; Ryle et al. 1950) and have been intensely studied ever since (see e.g. Israel et al. 1975; van der Kruit 1977; Graeve et al. 1990; Fletcher et al. 2011; Weżgowiec et al. 2022; Venkattu et al. 2023).

The main difference between the two galaxies is the structure of the spiral arms. M51 is a grand design spiral so it has only two regular spiral arms with embedded H II regions, which are clumps ionised interstellar medium and young stars. It also interacts with a smaller galaxy NGC 5194 that is approaching it from the north. M101 has multiple spiral arms which are more spread out and contain distinct H II regions. M101 is known for having massive giant H II regions which we study at low radio frequencies in Ch. 3.

1.2.1 Interstellar medium

The interstellar medium (ISM) is the baryonic matter located in the space between the stars in galaxies (for a detailed description of ISM see Draine 2011). The ISM accounts for approximately 20% of galactic mass (Read & Trentham 2005). Observations show that the ISM can exist in a few different distinct phases Cox (2005). The majority of the ISM in galactic discs (around 40%) is in the form of warm neutral medium consisting of hydrogen atoms (H I) at temperatures around $T \approx 10^{3.7}$ K. The density of warm neutral medium is around 0.6 atoms per cubic centimetre ($n_H \approx 0.6 \text{ cm}^{-3}$). The

1 Introduction

neutral hydrogen can be traced by observing the spectral line at 1.4 GHz produced by the spin-flip transition in H I atoms. The second most abundant phase (around 15%) is the warm ionised medium, which consists mainly of H II (ionised hydrogen) and it is ionised by the UV emission from hot stars. The temperature of the warm ionised medium is $T \approx 10^4$ K and the density of free thermal electrons is around $n_e \approx 0.25 \text{ cm}^{-3}$. The ionised ISM is primarily traced by observing of the H α recombination line, but fainter emission lines from other atoms and ions are also used to examine the properties of the gas and the ionising radiation (Reynolds 2004). The ionised regions around sites of massive star formation are called H II regions. Radio observations of H II regions are one of the main topics of this work (Ch. 3) and we introduce them further in Sect. 1.2.4. Cold neutral ISM is less abundant in galaxies at about 1%. It consists of the neutral hydrogen but at much lower temperatures ($T \approx 10^2$ K) and higher densities ($n_H \approx 30 \text{ cm}^{-3}$). As the ISM cools down to temperatures around $T \approx 50$ K, H₂ molecules form, creating molecular gas. Molecular gas is most commonly traced using CO emission lines which are strong and easy to observe (Kennicutt & Evans 2012). Molecular clouds can collapse under the effect of gravity reaching densities of the order of $n_H \gtrsim 10^3 \text{ cm}^{-3}$. This is where stars are formed. These dense molecular clouds also include dust grains and have high extinction which means they absorb visible light.

ISM is dynamic and it is influenced by magnetic fields, stellar wind, supernova explosions, and cosmic rays. The energy densities of CRs, the radiation field, the thermal gas, and the magnetic field are approximately equal in the ISM (Beck & Krause 2005; Yoast-Hull et al. 2016). The exact role of the magnetic field is still being explored but it is predicted that it is responsible for ordering the ISM on small scales (Jelić et al. 2015). There is a feedback loop between the ionised ISM which produces a magnetic field which in turn shapes the ionised ISM. We cover the topic of magnetic fields in galaxies in the next section (Sec. 1.2.2). Stellar winds and supernova explosion produce shock waves which move and compress the different ISM phases causing transitions between phases (Heiles & Haverkorn 2012). CRs influence the ISM in numerous ways: heating, ionising, initiating formation of complex molecules and interacting with the magnetic field (e.g. Viti et al. 2013). The combination of all the effects on the ISM is responsible for the rate of star formation in galaxies, which is smaller than expected from the amount of cold gas available in galaxies (Federrath 2015).

1.2.2 Magnetic fields in galaxies

There is a joke among astrophysicists, that if you do not know what question to ask at a talk, you should ask about magnetic fields. This is because not much is usually known about magnetic fields and their influence is often neglected, especially when considering galaxy evolution. However, we know that magnetic field plays an important role in controlling the SFR (Birnboim et al. 2015), gas dynamics of molecular clouds (Planck Collaboration et al. 2016a), density and propagation of CRs, outflows of hot gas (Hanasz et al. 2013), and cosmic-ray heating of ionised gas (Wiener et al. 2013).

The production of magnetic fields in galaxies can be explained in multiple steps: seeding, amplifying, ordering and sustaining. Fields are either seeded in the early universe (Durrer & Neronov 2013) or generated in the later stages of galaxy evolution through processes involving the ionised ISM, stars, or black holes (Beck 2015). The magnetic fields are efficiently amplified by the small-scale dynamo which is caused by turbulence in the ISM. The small-scale dynamo can amplify the strength of seed fields from below 5 nG (Planck Collaboration et al. 2016b) to several μG in less than 10^8 yr (e.g. Schleicher et al. 2010). The amplified turbulent fields are then ordered and sustained by differential rotation of galaxies, expanding gas affected by the Coriolis force and magnetic diffusion driven by turbulence (Beck et al. 1996). According to galactic dynamo models, turbulent magnetic fields are transformed into large-scale regular fields on a timescale of the order of 10^9 yr (Beck et al. 1994).

1.2 Nearby galaxies in the context of radio observations

One of the reasons for our ignorance about magnetic fields in galaxies is that they cannot be measured directly and each method can only trace some components of the total magnetic field. See Klein & Fletcher (2015) for a more complete and detailed review of magnetic field measurements.

The first method of measuring magnetic fields takes advantage of elongated dust grains in the ISM that tend to align perpendicularly to the field. Optical and infrared starlight gets polarised by those dust grains allowing us to trace the direction of the magnetic field in the plane of the sky. The same dust grains emit polarised light at infrared and submillimeter wavelengths.

The second method relies on CRs emitting synchrotron radiation, which dominates at radio frequencies (see Sect. 1.3.1). Equipartition is expected between the energy densities of CRs and the total magnetic field in galaxies (Beck & Krause 2005), this makes it possible to use the total radio intensity to estimate the total magnetic field strength. Also, synchrotron emission is polarised perpendicularly to the magnetic field so we can determine the direction of the magnetic field in the plane of the sky, if it is regular within the telescope beam. Additionally, polarised emission passing through magnetised ionised ISM experiences a frequency-dependant rotation of the polarisation angle. This effect is called Faraday rotation and it can help us trace the line-of-sight magnetic field component.

Finally, the magnetic field along the line of sight can be measured through the Zeeman splitting of spectral lines, which is a weak effect that requires high line intensities and careful correction of instrumental polarisation.

The average magnetic field strength has been determined from equipartition for multiple galaxy samples. Niklas (1995) measured an average total field of $B_{tot} = 7 \pm 2 \mu\text{G}$ for a sample of 74 spiral galaxies and Fletcher (2010) compiled observations of 21 bright galaxies to calculate the average total field of $B_{tot} = 17 \pm 14 \mu\text{G}$ and the average regular field of $B = 5 \pm 3 \mu\text{G}$. In the spiral arms of gas-rich spiral galaxies with high star-formation rates, like M 51, the total field strength is $20 - 30 \mu\text{G}$ (Beck 2015). The ordered fields in the plane of the sky in M 51 are $10 - 15 \mu\text{G}$ (Beck 2015).

1.2.3 The far-infrared–radio continuum correlation

There is an unusually tight correlation between the far-infrared (FIR) and radio continuum emission in "normal" star-forming galaxies (Helou et al. 1985; de Jong et al. 1985). This relation has a very low scatter and holds for over 5 orders of magnitude in luminosity (Yun et al. 2001). It holds for entire galaxies, as well as their parts in case where they are spatially resolved (e.g. Murphy et al. 2006). The FIR-radio correlation, however, does not hold for galaxies with additional ways of accelerating electrons, such as in active galactic nuclei (AGN) (Delhaize et al. 2017).

The explanation for this correlation is that both FIR and radio emission is driven by massive stars and both quantities correlate with the SFR. Massive stars end their life as supernovas which accelerate CR electrons that produce radio synchrotron emission. Also, the small-scale magnetic field in which CRs emit is turbulently amplified by star formation. On the other hand, FIR is emitted by dust which is heated by massive stars (Murphy 2009).

In local galaxies there is also a direct correlation between radio continuum emission and the SFR (Heesen et al. 2022). SFR is often traced with $\text{H}\alpha$ emission, but $\text{H}\alpha$ suffers from dust extinction so it has to be corrected and that leads to uncertainties. Radio emission, on the other hand, is not affected by extinction so it could be an independent tracer of SFR. The problem is that this relation is not thoroughly understood yet because of the different CR energy loss mechanisms.

Following are some open questions about the FIR-radio and radio-SFR relations. A common explanation for the FIR-radio correlation is the calorimeter theory (Voelk 1989) in which all the energy transferred from the massive stars to the ISM is emitted as radiation and does not escape the galaxy. In particular, all of the UV from massive stars is absorbed by dust and re-emitted in FIR, also the CRs

1 Introduction

lose all their energy due to synchrotron emission before diffusing out of the galaxy. This would easily explain the correlation because all the energy from star formation would be re-emitted. However, it is known that CRs escape from the galaxies and the radio spectral index predicted by the calorimeter model does not match observations. Other models were proposed as a solution (Murphy 2009; Lacki et al. 2010) but they often rely on a certain alignment of processes which is not necessarily physically motivated. These models also try to resolve the question of why the FIR-radio correlation holds at high redshift even though it should be broken due to the increased IC losses because of stronger cosmic microwave background (CMB) radiation.

Some of the proposed solutions rely on CR ionisation losses (Sect. 1.3.3) or free–free absorption (Sect. 1.3.2) to maintain the correlation. Both of those processes have very subtle effects at GHz frequencies in normal galaxies but could become relevant below 100 MHz or in starburst galaxies. If we can constrain these processes at low frequencies we can use it to confirm the proposed models. Also, it is important to find where exactly the power law behaviour breaks at low frequencies because those frequencies are not suitable for direct use as a SFR tracer. This is the main motivation for the work in Ch. 2 and 3.

For more details see section "The Far-Infrared-Radio Correlation in Galaxies" of Acosta-Pulido et al. (2015) starting at page 101 and the references within.

1.2.4 H II regions

H II regions are areas of ionised hydrogen (H II) which surround massive hot stars. They are described by the Strömgren sphere model (Strömgren 1939). The stars of the spectral type O and B are the hottest and bluest stars, which emit ionising ultraviolet radiation. This radiation ionises the surrounding neutral hydrogen H I, creating a region of only ionised H II with a very thin boundary. Inside of the region the ionising photons propagate freely because all the hydrogen atoms are ionised and they will not absorb the photons. When the photons leave the H II region and enter the surrounding H I, they are very quickly absorbed, ionising the H I atoms. The boundary of the Strömgren sphere is formed at the distance where ionisation and recombination are in equilibrium (Condon & Ransom 2016).

The formation of an H II region starts from a molecular cloud in which stars are born, and then they ionise their surroundings. This process of H II region formation lasts of the order of 10^5 years (Sabatini et al. 2021). Each H II region consists of thousands of stars that each produce a roughly spherical Strömgren sphere. The ionisation spheres of different stars interact with one another and the surrounding gas, resulting in complex shapes and inhomogeneity at all scales.

H II regions can be found by observing the $H\alpha$ spectral line (e.g. Santoro et al. 2022). They only appear in spiral and irregular galaxies and each galaxy can have from hundreds to thousands of H II regions (e.g. González Delgado & Pérez 1997; Petit et al. 1996). Large galaxies with high star formation, such as M101, have multiple thousands of H II regions (e.g. Hodge et al. 1990; Knapen 1998). H II regions have a wide range of diameters spanning from 0.03 pc up to hundreds of pc in the case of giant H II regions (Martín-Hernández et al. 2003; Kennicutt & Hodge 1986).

At radio frequencies, H II regions mostly produce free–free emission (see Sect. 1.3.2) which can be used to calculate properties of the H II region, such as the electron temperature, emission measure (EM) and the star formation rate (Condon & Ransom 2016).

1.2.5 Dwarf spheroidal galaxies

Dwarf spheroidal galaxies (dSph) are one of the most promising targets for DM searches so we observe them in Ch. 4. They are among the faintest galaxies, historically defined as having the absolute

magnitude below $M_B \approx -18^{\text{mag}}$ (Sandage & Binggeli 1984). Their small mass ($\sim 10^7 M_\odot$; Strigari et al. 2008) leads to a low gravitational potential. As a result, dSph quickly lose almost all their interstellar gas and they do not form new stars. This is their first advantage for DM searches, typical astrophysical signals associated with star formation are not produced in dSph so the backgrounds for DM searches is very low. Specifically in case of DM searches with radio, there are only old stars in dSph which do not produce supernovae so there are no new CR electrons which would produce synchrotron emission (see Sect. 1.3.1 for more on this process).

The second advantage in DM searches is that dSph are DM dominated, shown by their mass-to-light ratio between 1 and $120 M_\odot/L_\odot$ (Penny et al. 2009). The highest mass-to-light ratios are more than a hundred times higher than for the Sun and 20 to 50 times higher than for spiral galaxies (Mo et al. 2010). This means that the DM signal expected from dSph is brighter than from other astronomical objects (Strigari 2018).

dSph are located in roughly spherically symmetric DM halos which can be described with multiple different models (Navarro et al. 1997; Einasto & Haud 1989; Burkert 1995, etc.). The parameters of the DM halo have to be determined independently, because the expected DM signal depends in them. Usually this is achieved by stellar-kinematic observations. The velocities of individual stars in the dSph are measured from their spectra and used to fit the DM halo parameters (e.g. Geringer-Sameth et al. 2015).

Dwarf spheroidal galaxies are fairly common and many of them are satellites of our Milky Way galaxy. This is their third advantage as a target for DM searches. Because they are nearby, the stars in dSph galaxies can be resolved and their velocities can be independently measured. In the case of radio observations, dSph can be resolved and the shape of the radio signal can be used as an additional defining property of the DM signal. Also, there is a large sample of dSph that can be selected for a specific search and the signals from different galaxies can be stacked to improve limits.

1.3 Radio emission in galaxies

The optical light in galaxies comes from stars, but galaxies also emit in other parts of the electromagnetic spectrum, specifically radio waves. The total radio power of star-forming galaxies at 1.4 GHz is between 10^{19} and 10^{23} W/Hz (Hummel 1980), which is equal or up to 10 times lower compared to the optical luminosity of the same galaxies. Galaxies containing AGN, on the other hand, have significantly higher radio powers compared to their optical powers (Tadhunter 2016).

Radio waves in galaxies are produced either by spectral line or continuum emission. Line emission is mostly from neutral hydrogen at 1.4 GHz. The processes contributing to the radio continuum emission of spiral galaxies, depending on frequency, are shown in Fig. 1.2. The main contributions below 1 GHz are the synchrotron emission from CRs and free-free emission from the ionised ISM. These processes are described below, along with free-free absorption and CR ionisation losses which could be responsible for the low-frequency flattening of the radio spectrum.

1.3.1 Cosmic rays and synchrotron emission

The majority of continuum radio emission comes from the CRs that fill galaxies. CRs are high-energy particles: electrons, protons, alpha particles etc. Cosmic rays are produced in galaxies, they lose energy due to interactions and they diffuse throughout the galaxy and escape into intergalactic space. Mathematically this can be explained by the diffusion-loss equation which we present in Sect. 4.2 along with an approximate solution for a spherically symmetric case.

1 Introduction

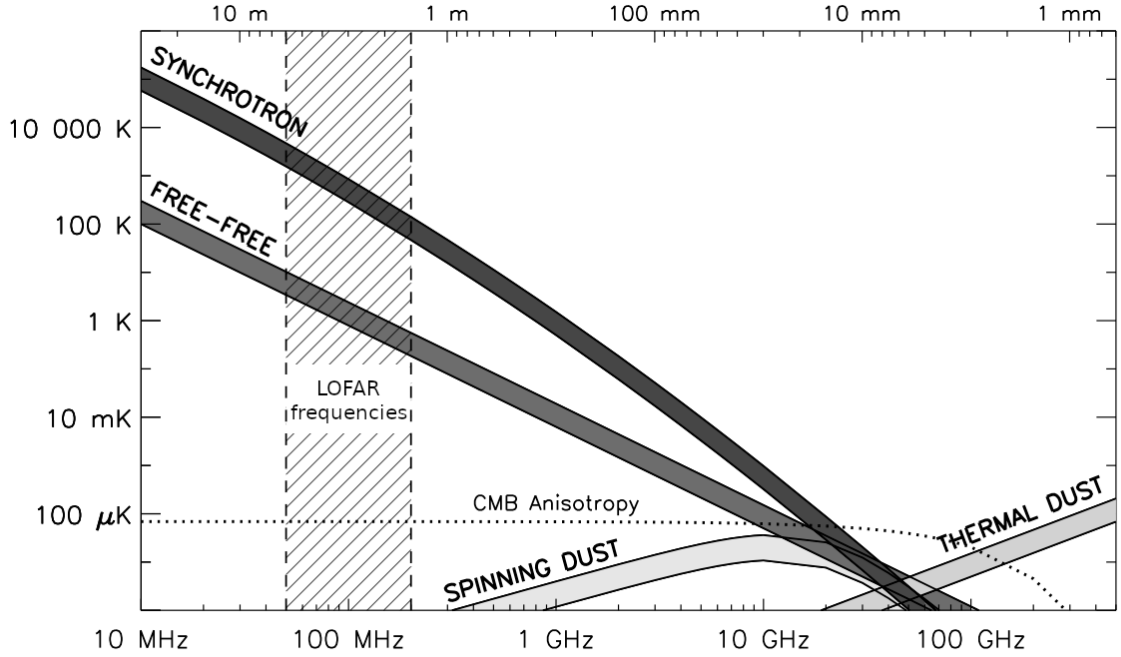


Figure 1.2: The contributions to the continuum emission of the Milky Way galaxy at low frequencies. Frequencies observed by LOFAR are highlighted (Chapman & Jelić 2019).

In galaxies CRs are produced by first-order Fermi acceleration of particles in supernova explosions. Therefore, CRs are generally produced in the regions of high star formation such as spiral arms and diffuse towards other parts of the galaxy. Of the order of 10% of energy produced in supernovas is transferred to CRs (Blasi 2013), the majority of that energy is used to accelerate heavier particles such as protons. CRs are $\sim 98\%$ nucleons, stripped of all their orbital electrons, and $\sim 2\%$ electrons. Even though they are considerably less abundant, we focus on CR electrons (CRe) because they have much lower mass and thus accelerate and produce radio emission more easily.

Supernova explosion produces a shock wave that accelerates the surrounding material and compresses the surrounding ISM. Particles gain energy by crossing the shock front since they are sped up by the shock. Due to turbulent magnetic fields, they can scatter back towards the shock front with a certain probability and cross it multiple times, thus gaining more and more energy every time. In a slightly simplified view, the amount of energy increase in each crossing of the shock front is proportional to the current CR energy and the probability of scattering back towards the shock is the same after every scattering (Gaisser et al. 2016). This results in a power-law energy distribution of CRs with a power-law index δ :

$$n_{CR}(E) dE \propto E^{-\delta} dE, \quad (1.1)$$

where $n_{CR}(E)dE$ is the number of CRe with energies between E and $E+dE$. This distribution is a power law at the time of acceleration and it evolves over time due to CR energy losses. The cosmic-ray energy spectrum measured in the Solar system is a mostly featureless power law ranging from around 10^{10} eV, below which CRs do not reach us due to the solar wind, to around 10^{20} eV, above which only a very small number of CRs can be accelerated (Hofmann & Hinton 2020).

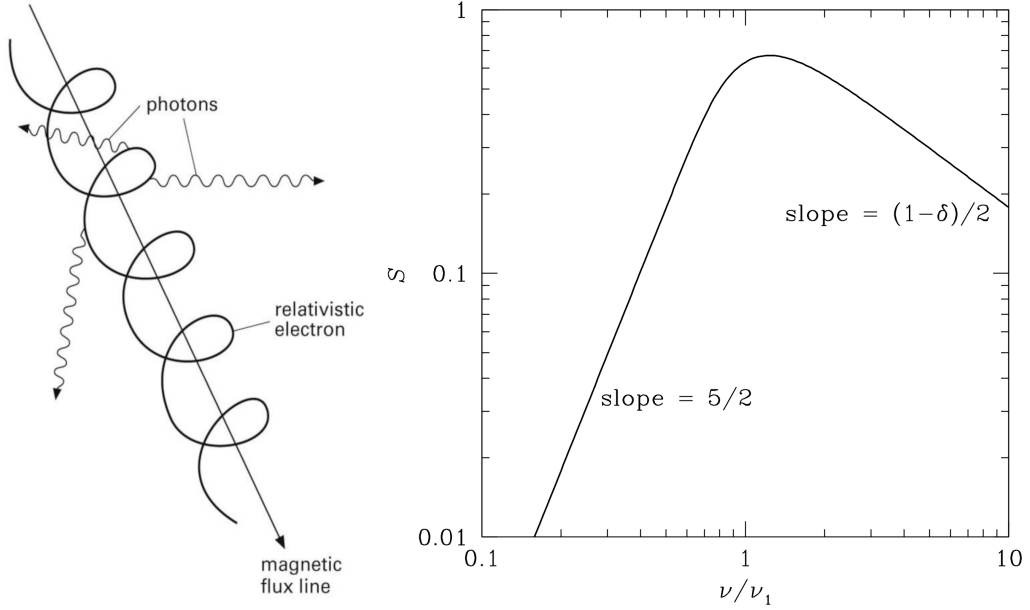


Figure 1.3: Left: Relativistic electrons spiralling around the magnetic field line and emitting synchrotron radiation (Collins Dictionary of Astronomy 2006). Right: The spectrum of synchrotron emission at relatively low frequencies which includes the synchrotron self absorption (Condon & Ransom 2016).

Cosmic rays lose energy mainly due to inverse Compton (IC) scattering, synchrotron emission, and ionisation. IC losses result from the scattering of low-energy photons on high-energy CReS, in which the energy is transferred to the photon making the CReS lose energy. The low-energy photons come from the CMB radiation and from the stars in the galaxy. Synchrotron emission is the main signal observed at radio frequencies so we explain it in detail below. Ionisation losses, introduced in Sect. 1.3.3, are a proposed way of explain the low-frequency flattening in galaxies.

In general, synchrotron radiation is emitted by relativistic charged particles which are accelerated in a direction perpendicular to their velocity. In galaxies, this happens when CReS travel on spiral trajectories around magnetic field lines (Fig. 1.3, left). For a single electron, synchrotron emission peaks around a critical frequency (Rybicki & Lightman 1986; Murphy 2009):

$$\nu_c = \frac{3eBE^2}{2\pi m_e^3 c^5} = 1.3 \cdot 10^{-2} \text{ GHz} \left(\frac{B}{\mu\text{G}} \right) \left(\frac{E}{\text{GeV}} \right)^2 \quad (1.2)$$

where B is the magnetic field strength and E is the CRe energy. Typical CRe energies are between 1 and 100 GeV and the magnetic field in galaxies is of the order of μG (Sec. 1.2.2). The resulting emission is between tens of MHz and hundreds of GHz.

To get the total spectrum of synchrotron emission we have to sum up the contributions from individual electrons whose energies follow a power law (Eq. 1.1). The resulting spectrum is a power law in terms of frequency ν :

$$S_\nu \propto \nu^\alpha, \quad (1.3)$$

where $\alpha = (1 - \delta)/2$ is the radio spectral index. The spectral index is one of the most important quantities in radio observations because it relates to the CR distribution in the observed object and it can be very easily calculated from observations on at least two different frequencies. The injection

1 Introduction

spectrum of CRes from supernovae is $\alpha \approx -0.5$ (Blandford & Eichler 1987) and it steepens (becomes more negative) as the CRes propagate and lose energy. High-energy CRes, emitting at around 8350 MHz, take around 7 Myr to lose energy from synchrotron emission, and they reach distances around 1 kpc. Low-energy CRes, emitting at around 54 MHz, take longer (around 90 Myr) to lose energy from synchrotron emission, and they reach distances around 5 kpc (Heesen et al. 2023). CRes can also be re-accelerated, which flattens the spectrum (makes the spectral index less negative), for example by shocks produced in galaxy cluster mergers (e.g. Ensslin et al. 1998). The typical values of the spectral index α in star-forming galaxies are between -1.2 and -0.5 (e.g. Gioia et al. 1982; Li et al. 2016; Tabatabaei et al. 2017). Significant deviations from those values or significant variations with frequency are evidence for additional processes in the galaxy, either affecting the CRe population or the radio signal through emission and absorption.

An additional property of synchrotron radiation is that it is partially linearly polarised in the direction perpendicular to the magnetic field (Rybicki & Lightman 1986). The polarisation angle of the emitted radiation is affected by the medium that it passes through which provides an additional source of information about the ISM (Heald 2015).

The intensity of synchrotron radiation increases with decreasing frequency until it becomes sufficiently high to be re-absorbed by the same charged particles in the magnetic field that emitted it. This process is called synchrotron-self absorption (SSA) and it causes a saturation of synchrotron emission below a turnover frequency ν_{SSA} , as shown on the right panel of Fig. 1.3 (Condon & Ransom 2016). For typical μG magnetic fields in star-forming galaxies, SSA does not become relevant until the frequency is decreased below 1 MHz (see Sect. 2.4.2 for a more detailed calculation). However, SSA is relevant in AGN where the magnetic field and synchrotron intensity is several orders of magnitude higher than in star-forming galaxies (Ishibashi & Courvoisier 2011).

1.3.2 Free–free emission and absorption

Free–free emission is produced by free electrons scattering on ions inside an ionised interstellar medium (Fig. 1.4, left). The electrons are not captured by the ions so they are free both before and after the interaction. Free–free emission is thermal because the electrons and ions interact often enough to come into local thermal equilibrium.

Free–free radiation is a type of bremsstrahlung (from German "breaking radiation"), radiation produced by charged particles accelerating (or decelerating). In case of free–free emission, the acceleration is due to electrostatic forces, in contrast to synchrotron emission which can be understood as magnetobremsstrahlung or "magnetic braking radiation".

Interactions of free electrons and ions can cause both emission and absorption. Because of that, the relevant quantity is the optical depth τ , which is defined as the logarithmic ratio between the incident and transmitted radiant power through a material. Depending on the value of τ , two regimes can be identified. If $\tau \ll 1$, the medium is transparent and emission from the entire volume can reach the observer. In case of free–free emission, this results in a power law spectrum with $\alpha \approx -1$. If $\tau \gg 1$, then most of the radiation is being re-absorbed before it reaches the observer and they only receive the radiation emitted in the part that is close to the border of the ionised ISM region. The spectrum in the optically thick regime is that of a blackbody with brightness temperature approaching the electron temperature (Condon & Ransom 2016). Example spectra are plotted on the right in Fig. 1.4, both regimes can be seen along with the turnover at $\tau = 1$.

The optical depth depends on the frequency ν of radiation and can be calculated for electrons in thermal equilibrium, which have a Maxwellian distribution of velocities corresponding to temperature T_e (Lequeux 2005). At the radio wavelengths, an approximate expression for the free–free optical

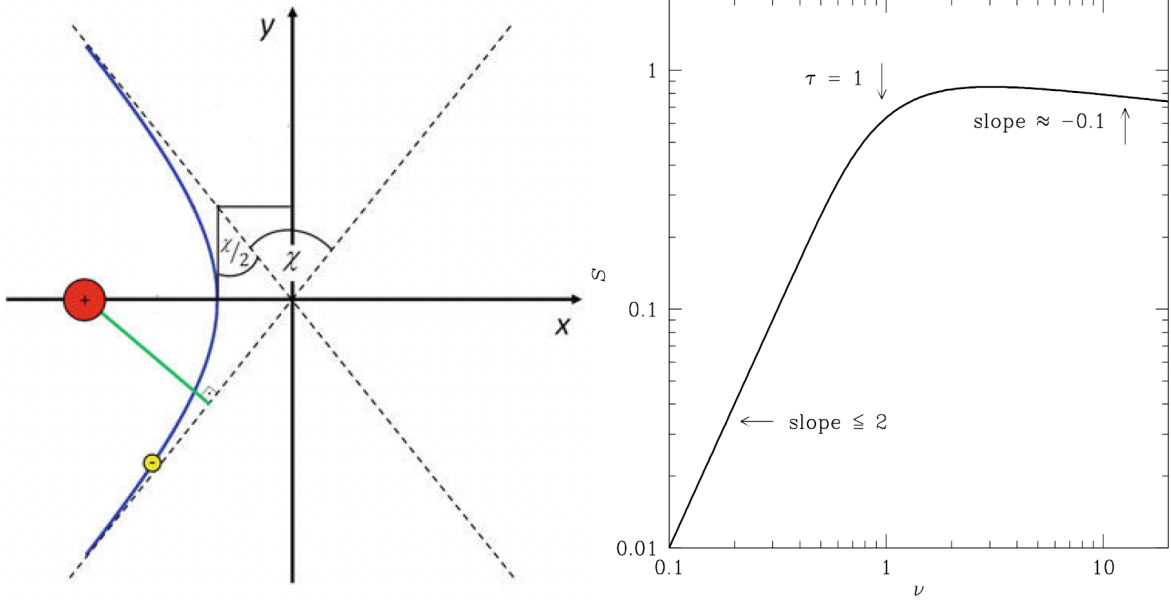


Figure 1.4: Left: The trajectory of the electron near the atom that results in free–free emission production (Klein & Fletcher 2015). Right: The spectrum of free–free emission, the frequency is expressed in terms of the turnover frequency (Condon & Ransom 2016).

depth τ is (Brussaard & van de Hulst 1962):

$$\tau_{\text{ff}} = 8.2 \times 10^{-2} \nu^{-2.1} T_e^{-1.35} \text{EM}, \quad (1.4)$$

where ν is the frequency in GHz, T_e is the electron temperature in K and EM is the emission measure in units of $\text{cm}^{-6} \text{pc}$. The EM is defined as

$$\left(\frac{\text{EM}}{\text{pc cm}^{-6}} \right) = \int_0^{s_0} \left(\frac{n_e}{\text{cm}^{-3}} \right)^2 \left(\frac{ds}{\text{pc}} \right), \quad (1.5)$$

where n_e is the free thermal electron density, and ds is the infinitesimal depth element along the line of sight between the source at s_0 and an observer at $s = 0$ (Lequeux 2005).

In the optically thick regime, the ionised ISM is absorbing all radio emission, specifically it absorbs synchrotron emission. The resulting spectrum is a synchrotron power law for frequencies above the turnover frequency where $\tau = 1$ and below this frequency the flux steeply decreases. The turnover frequency depends on the electron temperature and the EM (Eq. 1.4). Also, different spectral models are necessary if the synchrotron radiation is emitted throughout the same medium that absorbs it, compared to synchrotron being emitted independently and only passing through free–free absorbing medium (e.g. Wills et al. 1997; Tingay & de Kool 2003; Kapińska et al. 2017). Spectral models for free–free absorbed synchrotron radiation are expressed and applied in Sect. 2.4.3 and 3.4.2.

1.3.3 Cosmic ray ionisation losses

Cosmic rays in galaxies, among other processes, lose energy by ionising the neutral atoms in the medium that they pass through. The majority of the neutral atoms in galaxies are hydrogen atoms and the energy loss of electrons is directly proportional to the number density of neutral atoms n . In simple words, the expression for the energy loss is derived by calculating the energy loss in a single

1 Introduction

collision between a CRe and a neutral atom and then integrating this to get the average energy loss per unit time. The final equation is (Longair 2011):

$$-\left(\frac{dE}{dt}\right)_{\text{ion}} = 7.64 \times 10^{-15} n (3 \ln \gamma + 19.8) \text{ eV s}^{-1}, \quad (1.6)$$

where γ is the Lorentz factor which is directly proportional to the energy E for relativistic CR particles. We see that the ionisation loss dependence on the energy is only logarithmic, which is a very weak dependence, so the ionisation energy loss can be approximated as energy independent. In a set time frame, the high- and low-energy CRs lose the same absolute amount of energy due to ionisation. After that, the low-energy CRs are left with just a fraction of their initial energy while the high-energy CRs are barely affected. Thus, the time in which the CRs lose all their energy is much shorter for low-energy CRs compared to the high-energy CRs (Thompson et al. 2006). This dependence is almost linear, as can be seen in Eq. (2.16). Equation (1.2) shows that the frequency of synchrotron radiation emitted by a single CRe is proportional to the CRe energy squared. This means that if the low-energy CRes lose energy fast enough due to ionisation, then the synchrotron emission at very low frequencies is going to be suppressed.

To determine the frequencies where that becomes relevant, we have to also consider synchrotron and IC losses which have an opposite energy dependence compared to ionisation losses. In a star forming galaxy, the synchrotron and IC loss time scale is much shorter compared to the ionisation loss time scale for CRs emitting at GHz frequencies. Those CRs will lose all their energy due to synchrotron and IC way before the ionisation loss becomes relevant (Basu et al. 2015). For a normal galaxy with the magnetic field $B = 10 \mu\text{G}$ and HI number density $n = 1 \text{ cm}^{-3}$, the ionisation losses dominate below approximately 100 MHz and cause the spectrum to flatten (see Fig. 1 in Murphy 2009).

Let us now compare the low-frequency flattening due to ionisation losses to the low-frequency turnover due to free–free absorption. First, the ionisation losses affect the CRe distribution which causes less synchrotron to be emitted, while free–free absorption affects the radio-waves that have already been emitted, either through synchrotron or another process. Because of that, the way they affect the spectrum is different. The ionisation losses can only flatten the spectrum at low frequencies, making the spectral index less negative. On the other hand, free–free absorption can cause a turnover in the spectrum and make the spectral index positive at low frequencies. In practice, as we go down in frequency we will first just observe a flattening which can be attributed to either process, only further decreasing the frequency can reveal the turnover associated with free–free absorption. The second difference, that can help us to distinguish which process is flattening the spectrum, is that the two processes occur in different ISM phases. Ionisation loss is relevant in the neutral medium because neutral atoms have to be present in order to be ionised by CRs. Free–free absorption is relevant in the ionised medium because the electrons and ions need to be separate for them to be able to interact and absorb the radio emission. In Sect. 2.4.3 and 2.4.4, we use this difference to pinpoint the process responsible for the low-frequency flattening in the galaxy M51.

1.4 Dark matter

Observations at scales from dwarf galaxies to the entire universe indicate that there exists an additional invisible matter component called dark matter. Some of the evidence for the existence of DM is: velocities of galaxies in clusters (Zwicky 1933), galactic rotation curves (Rubin & Ford 1970), the power spectrum of the cosmic microwave background radiation (Spergel et al. 2003; Aghanim

et al. 2020), the abundance of elements in the universe (Hinshaw et al. 2013), the distribution of mass in merging galaxy clusters; specifically the Bullet cluster (Markevitch et al. 2004), and gravitational lensing (Massey et al. 2010). From the CMB spectrum, the abundance of DM in the universe is calculated to be 84% of all matter (Aghanim et al. 2020). Studying the velocity dispersion and gravitational lensing enables us to get a more precise DM distribution down to galactic scales.

DM evolves under the influence of gravity and no other interactions, except for gravity, have ever been detected. Non-gravitational interactions of DM would leave signatures on the cosmic microwave background radiation, observed cosmic structure, and the abundances of light elements in the universe. From this we know that DM is not baryonic, meaning that if it interacts with the strong, weak or electromagnetic force, this interaction is very weak and does not affect DM evolution on astrophysical scales. However, this still does not offer a clear answer to the nature of DM, and for that reason we are motivated to search for this potentially very weak interactions. To start, we have two (potentially three) possibilities: DM is a particle or DM is a macroscopic object (or DM does not exist and our fundamental kinematic theories have to be re-examined). Both possibilities have to satisfy the same conditions: DM should be stable on the timescale of the universe and there has to exist a mechanism to produce enough DM in the early universe to account for its present abundance.

If DM is a particle, we start from the Standard model of particle physics (SM). The SM explains the interactions of known baryonic matter, but it also leaves some open questions which can be solved by introducing new particles, although it is not always trivial to prove that these particles can be abundant enough to constitute all DM. The main DM candidate we focus on in this work are WIMPs, the weakly interacting massive particles (Jungman et al. 1996). They solve the questions of the difference between force and matter by introducing a supersymmetric particle to each standard model particle. The supersymmetric counterparts of half spin particles have whole number spins and vice versa, thus introducing a symmetry between force carriers and other particles. For more about how WIMPs could be produced in the universe and the searches for them see the next section (Sect. 1.4.1). Other notable particle DM candidates are axions (Peccei & Quinn 1977a,b; Weinberg 1978; Wilczek 1978), axion like particles (Kim 1987; Jaeckel & Ringwald 2010), sterile neutrinos (Ibarra 2015), dark photons (Fabbrichesi et al. 2021), and fuzzy cold DM (Hu et al. 2000).

The macroscopic DM candidates are referred to as a massive compact halo objects (MACHO; Paczynski 1986; Griest 1991). Among them are also primordial black holes (Hawking 1971). As an alternative theory, it has also been suggested that DM does not exist as such and the effects that we attribute to it can be explained by modified Newtonian dynamics (MOND; Milgrom 1983). This modification would be very slight and would only produce substantial effects at astrophysical scales. However, MOND struggles to explain all the observational evidence (Clowe et al. 2006; McGaugh 2015; Nieuwenhuizen 2017).

1.4.1 Weakly interacting massive particles (WIMPs)

WIMP abundance in the universe is explained by the freeze out scenario. In the early universe the DM particles and standard model particles were in thermal equilibrium and they easily converted into one another. As the universe expanded and cooled, the conversion rate decreased until it became almost negligibly small. The number density of WIMPs froze out and from that point evolved with the expansion of the universe independently of baryonic matter. If WIMPs are DM, we can calculate the annihilation cross section necessary to account for the current DM density: the thermal relic cross section. This cross section is $\langle\sigma v\rangle \approx 2.2 \times 10^{-26} \text{ cm}^3 \text{ s}^{-1}$ for WIMP masses above 10 GeV and it increases slightly at lower masses (Steigman et al. 2012). Coincidentally, this cross section is of the same order of magnitude as the Standard model weak interactions, so the role of WIMPs

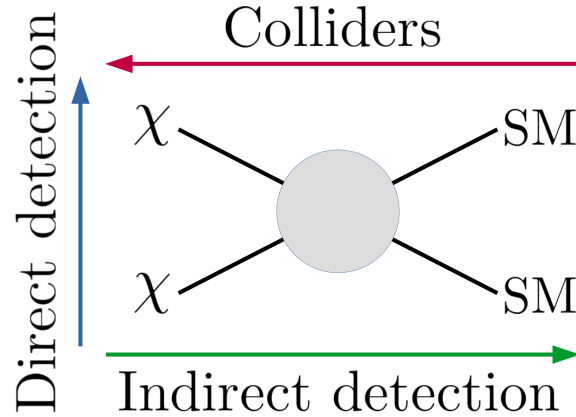


Figure 1.5: Types of WIMP searches and the channels of interaction they are probing.

could be filled by a particle that extends the Standard model and interacts via the weak nuclear force. This coincidence is called "the WIMP miracle" and presents an additional argument for WIMP DM (Jungman et al. 1996).

Let us now shift our focus to searches for WIMPs. DM searches can be divided in two categories: direct and indirect searches. They probe different channels of interaction between WIMPs and SM particles as shown in Fig. 1.5. Direct searches aim to detect signals from DM interactions with the SM particles. For WIMPs this is most commonly the spin-independent WIMP-nucleon interaction cross section σ_{SI} . On the other hand, indirect searches are attempting to detect the SM particles produced from DM or their signal. The quantity constrained by indirect searches is the velocity averaged cross section for WIMP self-annihilation $\langle\sigma v\rangle$. Direct searches are conducted on a laboratories on Earth, while indirect searches look for signals from the astrophysical objects. In addition, WIMP searches can be conducted in particle colliders by identifying if DM is produced in collisions of SM particles.

The idea for direct WIMP searches originates from neutrino detectors (Drukier & Stodolsky 1984). There is a large quantity of material that WIMPs could interact with and very sensitive detectors to record this interaction. The material and detector depend on the type of interaction: scintillation, ionisation, or phonons (Bismark 2019). In Fig. 1.6, the direct detection methods are summarised along with the most prominent experiments. Scintillation detectors use photomultiplier tubes to detect light from WIMPs interacting with solid crystals or liquid noble gases. Ionisation detectors use CCDs to look for charge produced by WIMP interactions. Most detectors with liquid noble gases (argon or xenon) can detect both ionisation and scintillation. Phonon detectors are primarily bubble chambers where the heat induced by nuclear recoil from WIMPs causes bubble formation in Fluorine-rich target liquids (Kuźniak 2023).

Direct detection experiments have significantly limited the parameter spaces for WIMP-nucleon interaction, especially for WIMP masses above 10 GeV (Fig. 1.7). The strongest limits are about two orders of magnitude from the neutrino fog, the theoretical lower limit for direct detection below which the DM signals is indistinguishable from the neutrino background.

Indirect DM searches have the advantage of targeting astronomical systems which are rich in DM and they are not limited by the DM density on Earth or the size of detectors which are possible to build. However, the expected signals and backgrounds are much harder to constrain. The DM distribution and other relevant parameters have to be determined through observations. There are also other processes in galaxies that can produce a similar signal to WIMP annihilation. The best

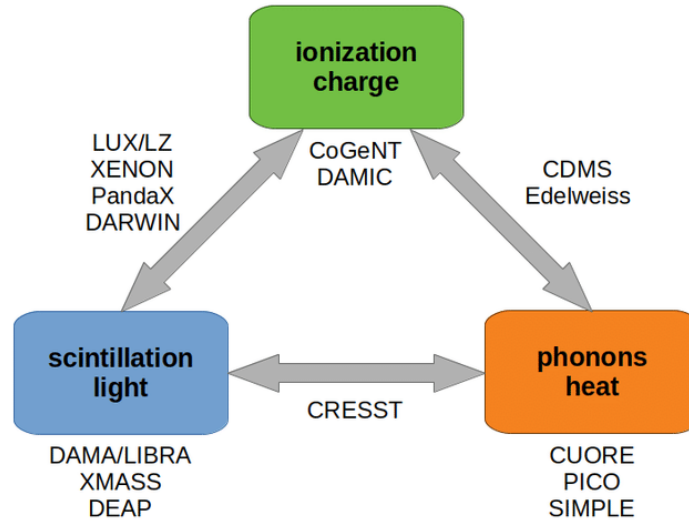


Figure 1.6: WIMP direct detection methods and most prominent experiments using each method or combination of methods (Bismark 2019).

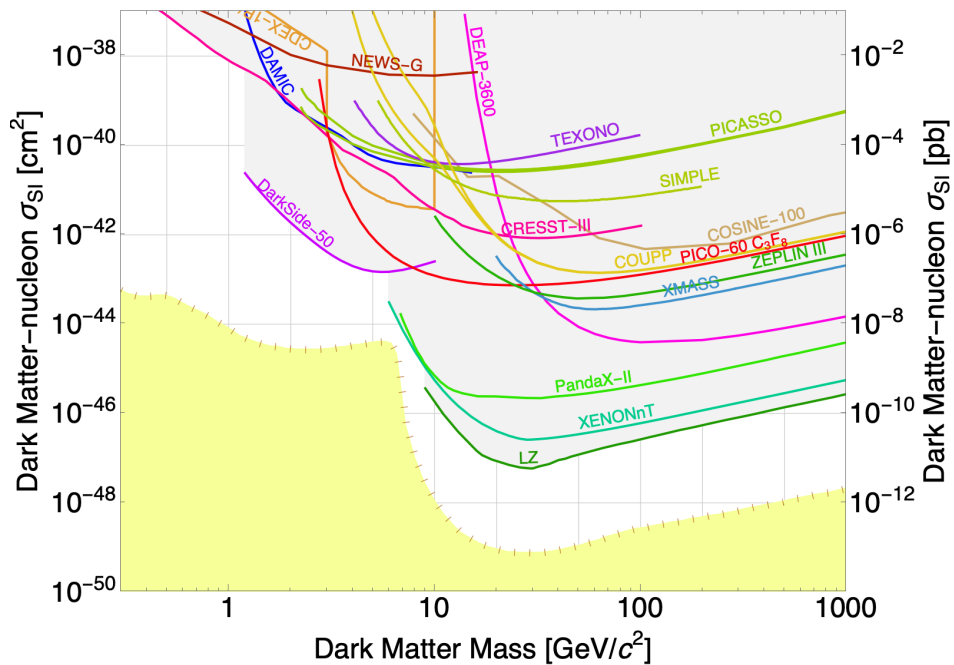


Figure 1.7: Limits on the spin-independent WIMP-nucleon scattering from direct WIMP searches. The neutrino fog is shown in yellow. Generated with DMLimit Plotter.

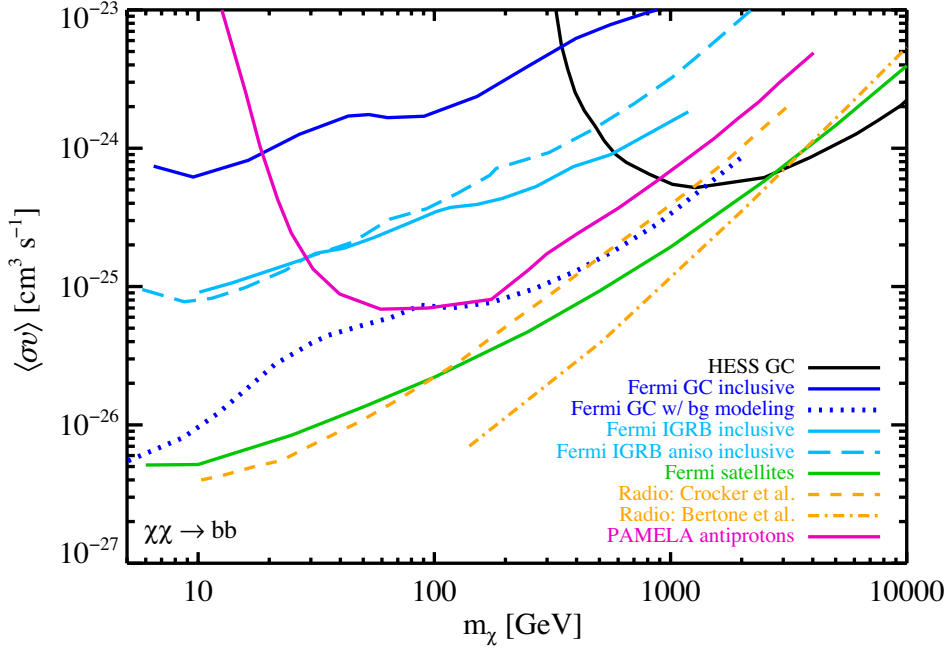


Figure 1.8: Limits on the WIMP self-annihilation cross-section $\langle\sigma v\rangle$ from indirect WIMP searches (Gaskins 2016).

observational targets are astronomical systems which have a high density of DM and relatively low backgrounds such as dwarf spheroidal galaxies (Sect. 1.2.5), the centre and halo of the Milky Way, galaxy clusters, the Sun, the Earth etc. For a detailed review of indirect DM searches see Gaskins (2016).

The products of WIMP self-annihilation that could reach Earth are stable particles or electromagnetic waves produced by the interaction of those particles with the environment where they are produced. Most commonly, indirect searches are looking to detect gamma-rays. They propagate directly from their source, unlike CRs, and carry spectral information. Gamma-rays can be detected directly on satellites such as *Fermi* Large Area Telescope (*Fermi*-LAT; Ackermann et al. 2015; Hoof et al. 2020) or Earth based telescopes such as H.E.S.S. (Abramowski et al. 2011), MAGIC (MAGIC Collaboration 2016; Maggio 2021) and the CTA (Cherenkov Telescope Array Consortium et al. 2019). The Earth based telescopes detect the Cherenkov radiation from the particle showers gamma-rays produce in the Earth's atmosphere. Data from different telescopes can also be combined in order to achieve stronger limits (like it was done by MAGIC Collaboration 2016, who combined *Fermi*-LAT and MAGIC data). Limits on the WIMP annihilation cross section from recent indirect searches are in Fig. 1.8. The strongest single-instrument limits come from *Fermi*-LAT observations of 27 dSph over 11 years (Hoof et al. 2020). They exclude thermal WIMPs (the freeze-out cross section) with masses of $\lesssim 100$ GeV annihilating through the $b\bar{b}$ channel and WIMPs with masses of $\lesssim 20$ GeV annihilating through the e^+e^- channel. Other important gamma-ray limits are from the observations of the Galactic centre (Gómez-Vargas et al. 2013; Hooper et al. 2013) and the isotropic gamma-ray background (Abdo et al. 2010; Gómez-Vargas et al. 2014).

Searches for cosmic rays from WIMP annihilation are being conducted by PAMELA, *Fermi* LAT, AMS-02, ATIC and GAPS. Cosmic rays can not be traced back to their origin because their trajectories change in the magnetic fields so it is not possible to select an individual target. Astrophysical CR sources only produce particles, while WIMP annihilation produces particle-antiparticle pairs. There-

fore, antiparticles in CRs are the main target of CR WIMP searches. Measurements of the anti-proton flux have produced strong limits on WIMP annihilation, but an excess of positrons incompatible with those limits has been detected by several instruments (Adriani et al. 2009; Ackermann et al. 2012; Aguilar et al. 2013). Searches for anti-deuterons and anti-helium are also being conducted (Gaskins 2016).

The final particle for indirect searches are neutrinos. In addition to the other sources, neutrinos are used to search for WIMPs annihilation in the Sun and the Earth, because only neutrinos are able to escape after WIMP annihilation in these objects. The IceCube, ANTARES, and Super-K facilities have published WIMP limits from neutrino non-detections (Gaskins 2016).

Searches for signals emitted by particles produced in WIMP annihilation are primarily conducted by radio telescopes. This is the main focus of our research and our targets are dSph. Other targets have also been observed before, such as the Galactic centre (Bertone et al. 2009; Crocker et al. 2010) and galaxy clusters (Lavis et al. 2023).

1.4.2 Search for WIMPs in dwarf spheroidal galaxies with radio telescopes

WIMPs self-annihilate into standard model particle pairs, namely e^+e^- , $\mu^+\mu^-$, $\tau^+\tau^- \nu\bar{\nu}$, $q\bar{q}$, $c\bar{c}$, $b\bar{b}$, $t\bar{t}$, W^+W^- , ZZ , hh . In these annihilation channels, electron-positron pairs are produced in the final state. Since the proposed WIMP mass is much bigger than the electron mass, the electrons produced this way have a high kinetic energy, which means that they can be treated as CRs in an astrophysical environment (Colafrancesco et al. 2007). In the presence of magnetic fields the CRe produce synchrotron emission. This emission is expected to peak at low radio frequencies. As an order of magnitude calculation, for WIMP masses of the order of 10 GeV and microgauss (μG) magnetic fields, the critical frequency of synchrotron radiation produced by the CRe (Eq. 1.2) is of the order of a few gigahertz (Rybicki & Lightman 1986), which means that it emits at frequencies lower than that. There are several extremely sensitive radio telescopes in that frequency range which are being used to search for DM signals in dSph and galaxy clusters.

No radio signal from DM has been detected, but even a non-detection provides information about WIMPs. We can calculate expected signal depending on the WIMP mass and cross section (Vollmann et al. 2020). For the WIMP mass and cross section in a certain range, the signal is high enough that we should detect it with the radio telescope. If we do not detect anything, that means that the WIMPs within this mass and cross section range do not exist. In practice this is expressed as an upper limit on the self-annihilation cross section that depends on the WIMP mass. Put simply, for each possible WIMP mass (in a certain range), we know that the cross section must be below the upper limit value. The usefulness of this result comes from the freeze-out mechanism, it has been calculated that the cross section of WIMPs has to be at least $\langle\sigma v\rangle \approx 2.2 \times 10^{-26} \text{ cm}^3 \text{ s}^{-1}$ for WIMPs to make up DM (Steigman et al. 2012). If our upper limit is lower than the freeze-out cross section in a certain WIMP range, that excludes thermally produced WIMPs in that range.

Of course, this is not simple to do and there are inherent uncertainties because of the way we calculate the expected radio signal from WIMPs. In this work, we focus on dwarf spheroidal galaxies as the main target for WIMP detection (see Sect. 1.2.5). The expected signal can be calculated by solving the diffusion loss equation for the CR electrons in the dSph. This equation connects the injection of CRs from WIMP self-annihilation, diffusion throughout the galaxy, and the energy losses due to synchrotron and inverse Compton radiation. The details of finding an approximate solution are described in Sec. 4.2 and Vollmann et al. (2020). An exact solution as well as a computing tool has since been developed by Vollmann et al. (2024).

As an introduction, let us focus on the main information needed and assumptions made to obtain

1 Introduction

the radio signal expected from a DM halo of a dSph galaxy. As the initial starting point, spherical symmetry is assumed. The solution can then be separated into the halo function, which describes the DM halo depending on the distance from the galactic centre r , and the spectral function depending on frequency ν . For the halo function it is assumed that the DM halo is described by the NFW profile (Eq. 4.2, Navarro et al. 1997) and the parameters of the profile have been measured from the velocity dispersion of the stars in the dSph (Geringer-Sameth et al. 2015). The spectral function contains the particle physics side of the problem, for simplicity we assume that WIMPs only annihilate into e^\pm pairs.

To calculate the signal we need to know the magnetic field and the diffusion coefficient in dSph. Neither of those quantities have been measured in dSph, so we have to rely on measurements from other galaxies and that leads to uncertainties. For the magnetic field we assume equipartition between the magnetic field energy density and the CR energy density (Beck & Krause 2005). The resulting magnetic field is of the order of $1 \mu\text{G}$ but with an order of magnitude uncertainty. For the diffusion coefficient, we adopted a value of $10^{27} \text{ cm}^2 \text{ s}^{-1}$, which is in agreement with observations of nearby dwarf irregular systems (Murphy et al. 2012; Heesen et al. 2018) and the Milky Way (Korsmeier & Cuoco 2016). For further discussion of the selected values of these parameters and the resulting uncertainties see Sect. 4.2.3 and 4.4.3, respectively.

The first explorations of this method were purely theoretical, presenting the expected upper limits that could be achieved by current radio telescopes (Colafrancesco et al. 2007; Colafrancesco et al. 2015; Storm et al. 2017). A proof-of-concept study by Vollmann et al. (2020) showed that these observations were possible with the LOFAR radio telescope. They used LOFAR high band antennas (HBA) to observe in the dSph galaxy Canes Venatici I and found that for an individual galaxy, the

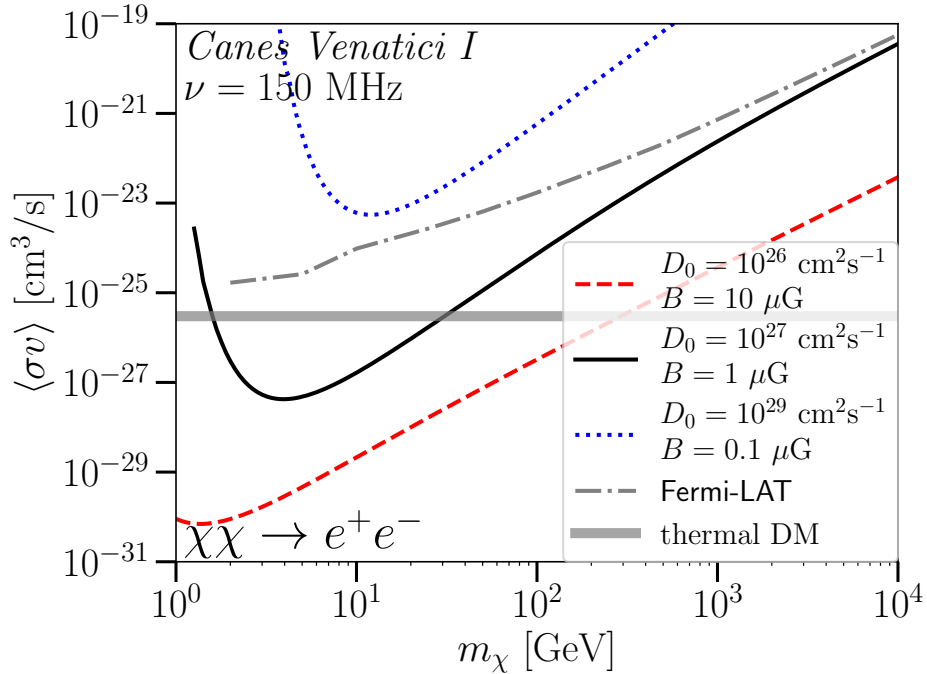


Figure 1.9: Limits on the WIMP annihilation cross section from radio observations of the galaxy Canes Venatici I compared to the thermal relic cross section and the *Fermi*-LAT gamma-ray limits for the same galaxy Vollmann et al. (2020).

limits are comparable to or even better than that from *Fermi*–LAT, assuming reasonable values for the magnetic field strength and diffusion coefficient. Their limits are shown in Fig. 1.9. We expanded on this result in Ch. 4, by observing a set of six dSph galaxies and stacking the results.

1.5 Radio-interferometry

Interferometers work by combining the signal from multiple antennas with the correct phase difference. The phase difference is determined from the time delay between the different antennas when looking at a specific direction. At long radio wavelengths, the phase of the electromagnetic wave can be recorded and the phase difference is applied digitally (Condon & Ransom 2016).

The angular scale on the sky to which an interferometer is sensitive is inversely proportional to the distance between the antennas. This means that interferometers can achieve significantly higher resolution compared to single dish telescopes because interferometer antennas can be further apart on the surface of the Earth compared to the size of a single telescope dish (Condon & Ransom 2016). However, this can be a disadvantage in case there is smooth radio emission on large angular scales. An interferometer is not sensitive to large scale emission if there are not enough short baselines available (Binney & Merrifield 1999). In this case it is possible to combine interferometric and single-dish data to achieve both high resolution and sensitivity to large scale emission (e.g. Fletcher et al. 2011; Weżgowiec et al. 2022).

1.5.1 LOFAR

LOFAR (LOw-Frequency ARray; van Haarlem et al. 2013) is a radio-interferometer centred in the Netherlands with stations in northern Europe. LOFAR uses two types of simple dipole antennas receive signals: the low band antennas (LBA) sensitive from 10 to 90 MHz and the high band antennas (HBA) sensitive from 110 to 250 MHz. The antenna design is optimised to reduce systematic noise, withstand weather conditions and have low production costs.

LOFAR consists of 24 core stations, 16 remote stations and 14 international stations. The core stations each have 96 LBA and two sets of 24 HBA receivers. The very centre of the array is the LOFAR Superterp (Fig. 1.10) consisting of six densely packed stations. The remote stations are located at larger distances within the Netherlands and consist of 96 LBA and 48 HBA receivers. The international stations are located in 7 European countries: six in Germany, three in Poland and one each in France, Ireland, Latvia, Sweden, and the United Kingdom. Additional stations in Bulgaria and Italy are funded to be built soon. To observe nearby objects with relatively low surface brightness, this work only uses the core and remote stations, since the higher sensitivity to diffuse emission and easier calibration is an advantage compared to the high resolution achievable with international stations.

A lot of new science was made possible by two large LOFAR surveys aiming to observe the entire northern sky: the LOFAR LBA Sky Survey (LoLSS; de Gasperin et al. 2021, 2023) at 54 MHz, and LOFAR Two-metre Sky Survey (LoTSS; Shimwell et al. 2017, 2019, 2022) which uses the HBA at 144 MHz. The survey team developed a standardised observation and calibration procedures for each type of antennas. The large amount of science ready data resulting from the surveys is used to study a variety of targets from the Milky Way and nearby galaxies to galaxy clusters and the cosmic web.

In this thesis, LOFAR is used because it is the only instrument observing below 100 MHz with a resolution of tens of arc-seconds. The low-frequency LOFAR observations are uniquely important for this work because the effects of free–free absorption and ionisation losses are only visible at low

1 Introduction



Figure 1.10: The LOFAR Superterp at the centre of the array (van Haarlem et al. 2013).

frequencies in normal spiral galaxies. The high resolution (below $25''$) was necessary to spatially locate the areas where these processes happen. LOFAR is also ideal for WIMP searches in the low mass range, because the frequency of produced synchrotron radiation depends on the square of the WIMP mass (see Sect. 1.4.2 and Eq. 1.2).

1.5.2 GMRT

GMRT (Giant Meterwave Radio Telescope; Swarup et al. 1991) is a radio-interferometer located in India about 80 km north of Pune. It consists of 30 fully steerable 45-m diameter parabolic dishes. Twelve of the dishes form a central core about $1 \text{ km} \times 1 \text{ km}$ in size and the remaining 18 are placed along the three arms in a Y-shaped configuration extending up to 14 km from the core. The original GMRT system operated in five frequency bands centred at 150, 230, 325, 610, and 1420 MHz. The system underwent a major upgrade in March 2019 and the upgraded GMRT (uGMRT; Gupta et al. 2017) now has four wide-band receivers. Our data, however, was taken before the upgrade. For more information on the features of the GMRT design, I would recommend the work by Kapahi & Ananthakrishnan (1995).

For our studies, the GMRT provides the maps of M 51 at intermediate frequencies of 240 and 333 MHz. These frequencies allow us to constrain the frequency range of the low-frequency flattening because they are not affected by the flattening. The dense core of the GMRT is especially important because it enables observations of large-scale diffuse emission of galaxies.

1.5.3 Apertif

Apertif (APERTure Tile In Focus; van Cappellen et al. 2022) is a Phased Array Feed (PAF) receiver mounted on the dishes of the Westerbork Synthesis Radio Telescope (WSRT). The instantaneous bandwidth is 300 MHz and it was centred at the frequency of 1280 MHz until January 2021 after which the central frequency was moved to 1370 MHz. This allows Apertif to observe H I out to a

redshift of 0.26. The PAF increases the field of view of the telescope by a factor of twenty-five and allows simultaneous observations of 40 individual compound beams covering an area of 6.6 deg^2 . This makes Apertif a very efficient survey instrument.

The Apertif legacy surveys began in July 2019 and consisted of: a shallow imaging survey, a medium-deep imaging survey, and a pulsars and fast transients survey. The imaging surveys provide H I, radio continuum and polarisation data products. I am specifically interested in the radio continuum results. The Apertif map of M 101 was important as a higher frequency reference to compare the 54 MHz flux to, in order to detect the low-frequency flattening. For more detail about the imaging surveys see Adams et al. (2022).

1.6 Outline of this thesis

The underlying main scientific questions that this research seeks to answer are:

- What are the processes shaping the very low-frequency radio emission in star forming galaxies?
- Are the processes shaping the very low-frequency radio emission different in H II regions?
- What are the consequences of the low-frequency flattening for the use of radio emission as an extinction-free tracer of star formation?
- Is dark matter made of WIMPs? Can we use radio observations to confirm that or put limits on WIMP interactions?

The work on these questions resulted in the following three publications:

Publication I **Gajović, L.**, Adebahr B., Basu A., Heesen, V., Brüggem M., de Gasperin F., Lara-Lopez M. A., Onk J. B. R., Edler H. W., Bomans D. J., Paladino R., Garduño L. E., López-Cruz O., Stein M., Fritz J., Piotrowska J., Sinha A. 2024. *A spatially resolved radio spectral study of the galaxy M 51*. A&A, 689, A68.

Publication II **Gajović L.**, Heesen V., Brüggem M., Edler H. W., Adebahr B., Pasini T., de Gasperin F., Basu A., Weżgowiec M., Horellou C., Bomans D.J., Dénes H., Vohl D. 2025. *The low-frequency flattening of the radio spectrum of giant H II regions in M 101*. Accepted to A&A; arXiv:2502.08713.

Publication III **L. Gajović**, Welzmüller F., Heesen V., de Gasperin F., Vollmann M., Brüggem M., Basu A., Beck R., Schwarz D. J., Bomans D. J., Drabent A. 2023. *Weakly interacting massive particle cross section limits from LOFAR observations of dwarf spheroidal galaxies*. A&A, 673, A108.

The content of these publications is presented in the following chapters of this thesis. The order of the chapters does not reflect the chronological order of publication.

The study of the low-frequency flattening in the spiral galaxy M 51 was performed at eight frequencies between 54 and 8350 MHz. The low-frequency flattening was shown in spectral index maps and integrated spectra for spiral arms and interarm regions. The spatial correlation of the flattening with ionised and neutral medium was tested in order to recognise the effect of free-free absorption and ionisation losses. This study makes up publication I and it is presented in Ch. 2. I am the lead author of this work and I was responsible for the main scientific analysis, getting the manuscript in

1 Introduction

the current shape and reaching the conclusions. This work was started independently and was later supplemented by an old project of B. Adebahr and A. Basu. The analysis of the 240 MHz GMRT data and the writing of the corresponding section was done by A. Basu. The members of the Metal-THINGS team (M. A. Lara-Lopez, L. E. Garduño and O. López-Cruz) produced the IFU spectroscopy map. The method for the separation of thermal and synchrotron emission as well as the separation of spiral arm, inter-arm, and galaxy core regions was prepared by B. A. and A. B. The manuscript by B. A. and A. B. was used as a starting point but I rewrote most of the text because new LOFAR data and the exploration of ionisation losses produced new results. I was also responsible for coordinating the work of different co-authors, re-analysing all the data and ensuring that the results are accurate by correcting mistakes. The other co-authors, especially V. Heesen, contributed to the manuscript and collaborative discussion of the results.

The low-frequency flattening was studied in giant H II regions of M 101 using observations at four frequencies between 54 and 4850 MHz. The spectra of six H II regions were examined and fitted with a free-free absorption model leading to findings about the localisation of the low-frequency turnovers and the consequences for the radio-FIR correlation. The study of M 101 H II regions makes up publication II and it is presented in Ch. 3. I am the lead author of this work and I was responsible for the manuscript and the scientific analysis. H. W. Edler produced the 54 MHz LBA map and wrote the accompanying section of the manuscript. B. Adebahr produced the 1370 MHz Apertif map and wrote the accompanying section of the manuscript. V. Heesen contributed the discussion on the implication for the radio-FIR correlation. The other co-authors contributed to the manuscript, data acquisition and collaborative discussion of the results.

The search for WIMPs in dwarf galaxies was performed by LOFAR HBA at 144 MHz. The data for six dwarf spheroidal galaxies was used to get separate and stacked upper limits on the WIMP self-annihilation cross-section. The limits were obtained by injecting an artificial DM signal into the LOFAR data before re-imaging and testing how high the signal needs to be for us to detect it with 2σ certainty. Two types of stacking the data from different galaxies was tested: stacking the radial profiles and stacking the radio maps. The uncertainties in these limits are discussed thoroughly and the final stacked limits are compared to other methods in the literature. The search for WIMP DM with LOFAR makes up publication III and it is presented in Ch. 4. I am the lead author of this work and I was responsible for the majority of the manuscript and scientific analysis. I closely collaborated with F. Welzmüller who developed the software for re-imaging the dwarf galaxy data and calculated the individual limits as a part of his master thesis, we also collaborated on the manuscript. I was responsible for the stacking results and the final shape of the manuscript. The theoretical calculations are based on the work of M. Vollmann (2021) and he provided the code used calculate cross-section limits from the Gaussian amplitudes of the sources. The other co-authors contributed to the manuscript and collaborative discussion of the results, uncertainties and implications.

The results are finally summarized and contextualized in Ch. 5. In this section, the connection between the two topics is highlighted and an outlook on future opportunities is provided.

2 A spatially resolved radio spectral study of the galaxy M 51

L. Gajović, B. Adebahr, A. Basu, V. Heesen, M. Brüggen, F. de Gasperin, M. A. Lara-Lopez, J. B. R. Oonk, H. W. Edler, D. J. Bomans, R. Paladino, L. E. Garduño, O. López-Cruz, M. Stein, J. Fritz, J. Piotrowska, A. Sinha, *Astronomy & Astrophysics*, 689, p.A68 (2024)

Abstract

Context. Radio continuum emission from galaxies at gigahertz frequencies can be used as an extinction-free tracer of star formation. However, at frequencies of a few hundred megahertz, there is evidence for low-frequency spectral flattening.

Aims. We wish to understand the origin of this low-frequency flattening better, and to this end, we performed a spatially resolved study of the nearby spiral galaxy M 51. We explored the different effects that can cause a flattening of the spectrum towards lower frequencies, such as free-free absorption and cosmic-ray ionisation losses.

Methods. We used radio continuum intensity maps between 54 and 8350 MHz at eight different frequencies, with observations at 240 MHz from the Giant Metrewave Radio Telescope presented for the first time. We corrected for the contribution from thermal free-free emission using an $H\alpha$ map that was corrected for extinction with $24\ \mu\text{m}$ data. We fitted free-free absorption models to the radio spectra to determine the emission measure (EM) as well as polynomial functions to measure the non-thermal spectral curvature. We also obtained a new extinction-corrected $H\alpha$ intensity map from the Metal-THINGS survey using integral field unit spectroscopy.

Results. The non-thermal low-frequency radio continuum spectrum between 54 and 144 MHz is very flat and even partially inverted, particularly in the spiral arms; in contrast, the spectrum at higher frequencies is typical for a non-thermal radio continuum spectrum. However, we did not find any correlation between the EMs calculated from radio and from $H\alpha$ observations; instead, the non-thermal spectral curvature weakly correlates with the $H\text{I}$ gas-mass surface density. This suggests that cosmic-ray ionisation losses play an important role in the low-frequency spectral flattening.

Conclusions. The observed spectral flattening towards low frequencies in M 51 is caused by a combination of ionisation losses and free-free absorption. The reasons for this flattening need to be understood in order to use sub-gigahertz frequencies as a tracer of star formation.

2.1 Introduction

At radio frequencies of a few gigahertz and below, the majority of continuum emission from galaxies is non-thermal synchrotron radiation, produced by cosmic-ray electrons (Niklas et al. 1997; Basu et al. 2012; Tabatabaei et al. 2017). These cosmic rays are accelerated in the shock-front of supernova explosions, and therefore, they originate from regions with higher star formation (Green 2014). The integrated spectrum of nearby galaxies at gigahertz frequencies (approximately 0.5–10 GHz) mostly follows a power law, where the flux density scales with frequency as $S_\nu \propto \nu^\alpha$; the radio spectral index α has values between -1.2 and -0.5 (Gioia et al. 1982; Li et al. 2016; Tabatabaei et al. 2017). If frequencies below approximately 300 MHz are included, however, the observed spectra are curved with a spectral curvature of $\beta = -0.2$, which denotes the change in spectral index per logarithmic frequency decade assuming constant curvature (Marvil et al. 2015).

While the value for the radio spectral index generally agrees with models of the overall injection spectrum of cosmic rays from supernovae ($\alpha \approx -0.5$; Blandford & Eichler 1987), including their energy losses mainly due to synchrotron and inverse-Compton radiation while propagating away from their origin (Gioia et al. 1982; Beck & Wielebinski 2013; Han 2017), the origin of the curvature is still a matter of debate (Basu et al. 2015; Mulcahy et al. 2018). Pohl & Schlickeiser (1990) and Pohl et al. (1991a,b) provided an explanation for curved spectra by combining ionisation and electronic excitation (Gould 1975), inverse-Compton radiation, synchrotron radiation, and relativistic bremsstrahlung, which would cause a smooth change in the spectral index of $\Delta\alpha = 0.5$ from higher to lower radio frequencies. On the other hand, Israel & Mahoney (1990) observed a dependence of the curvature on the inclination of the galaxies and concluded that a fragmented cool ionised medium with temperatures of 500–1000 K causes the curvature by thermally absorbing a part of the emitted synchrotron emission at lower frequencies. However, Hummel (1991) used the same data as Israel & Mahoney (1990) and were unable to find any correlation between the curvature in the sampled galaxies and their inclinations. A more recent study by Chyży et al. (2018) using additional data from the LO-FAR¹ Multifrequency Snapshot Sky Survey (MSSS) at 150 MHz (Heald 2015) confirmed the results by Hummel (1991).

Furthermore, integrated spectra of star-forming galaxies encompass a mixture of the complex interplay between thermal and non-thermal components and different energy loss and propagation effects in the most likely non-isotropic and inhomogeneous medium (Basu et al. 2015; Lisenfeld & Völk 2000). Studies of large samples of these objects are therefore limited by obtaining high-quality high-resolution observations at low radio frequencies ($\lesssim 300$ MHz). Advancements in data calibration and imaging techniques at these low-frequencies, especially for radio interferometers such as LOFAR (Tasse 2014; Tasse et al. 2018) and the Giant Metrewave Telescope (GMRT; Intema et al. 2009; Intema 2014; Intema et al. 2017), now allow the production of images with a high dynamic range with resolutions matching those of observations performed at gigahertz frequencies.

Spatially resolved studies are currently limited to nearby objects where individual star-forming regions can be analysed, and the radio emission of spiral-arm, inter-arm, and surrounding regions can be separated. Roy & Pramesh Rao (2006) showed that thermal absorption plays a key role in shaping the spectra of the centre of the Milky Way below 500 MHz, while its integrated-spectrum turns over at about 3 MHz (Brown 1973). Turnovers have also been detected for individual sources in the starburst galaxy M 82 (Adebahr et al. 2017) and in the integrated flux densities for the core regions of M 82 (Adebahr et al. 2013) and Arp 220 (Varenus et al. 2016) at around 1000 MHz. For these two objects, a flattening was also observed for the integrated (global) radio spectra (Klein et al.

¹LOw Frequency ARray

Table 2.1: Basic properties of M51.

Name	M 51
Alternative names	NGC 5194/5155
RA ₂₀₀₀	13 ^h 29 ^m 56 ^s 2
DEC ₂₀₀₀	+47°13′50″
Type	Galaxy Pair (Sa + Sc) ^a
Apparent size (D ₂₅)	9′
Distance	8.58 ± 0.10 Mpc ^b
Position angle	12°0′ ^c
Inclination angle	−20°3′ ^c

References. ^(a)Karachentsev et al. (1985), ^(b)McQuinn et al. (2016), ^(c)Hu et al. (2013)

1988; Condon 1992; Anantharamaiah et al. 2000), just like in the starburst galaxy NGC 253 (Marvil et al. 2015). Several of the compact H II-regions in the dwarf galaxy IC 10 show evidence of thermal free–free absorption in the radio spectra of the 320 MHz observations (Basu et al. 2017). Recently, evidence of low-frequency absorption was also found in the region of the edge-on galaxy NGC 4631 with a very flat radio spectrum (Stein et al. 2023). Local spectral turnovers were also observed in jellyfish galaxies, where they might be due to gas compression and subsequent ionisation losses (Lal et al. 2022; Ignesti et al. 2022; Roberts et al. 2024).

We chose M 51 as the target primarily because it benefits from multi-frequency radio continuum data. The face-on orientation and its proximity were also important because they facilitate resolving and separating the spiral arms. The other properties of M 51 are listed in Table 2.1. The entire galaxy is now mapped at 54 and 144 MHz with LOFAR (de Gasperin et al. 2019; Shimwell et al. 2022). Furthermore, data at 1370 and 1699 MHz were taken with the Westerbork Synthesis Radio Telescope (WSRT; Braun et al. 2007). At even higher frequencies, Fletcher et al. (2011) presented maps taken with the Very Large Array (VLA) at 4850 and 8350 MHz. The VLA maps were combined with maps observed with the 100 m Effelsberg telescope in order to observe all angular scales. These data were analysed by Heesen et al. (2023), who studied the transport of cosmic-ray electrons at kiloparsec scales and found it to be energy-independent diffusion for electrons with energies below 10 GeV.

In this paper, we extend the data with a new 240 MHz map from the GMRT. We used eight datasets observed at five different radio facilities (LOFAR, GMRT, WSRT, VLA, and Effelsberg) over the frequency range 54–8350 MHz to perform a spatially resolved radio spectrum study of the nearby spiral galaxy M 51. For the first time, we were able to separate the actively star-forming and non-star-forming regions of a nearby galaxy down to frequencies as low as 54 MHz. This allowed us to investigate the relation between the star formation and the flattening of the radio spectrum, and also to examine the origin of the flattening.

This article is structured as follows. In Sect. 2.2 we present our dataset spanning nine frequency windows. Section 2.3 describes the main data analysis, which included the subtraction of thermal emission (Sect. 2.3.2), the separation of galaxy regions (Sect. 2.3.3), spectral index maps (Sect. 2.3.4), and a comparison of low- and high-frequency spectral indices (Sect. 2.3.5). Spectral index flattening and low-frequency turnovers are investigated in Sect. 2.4. We summarise and conclude in Sect. 2.5.

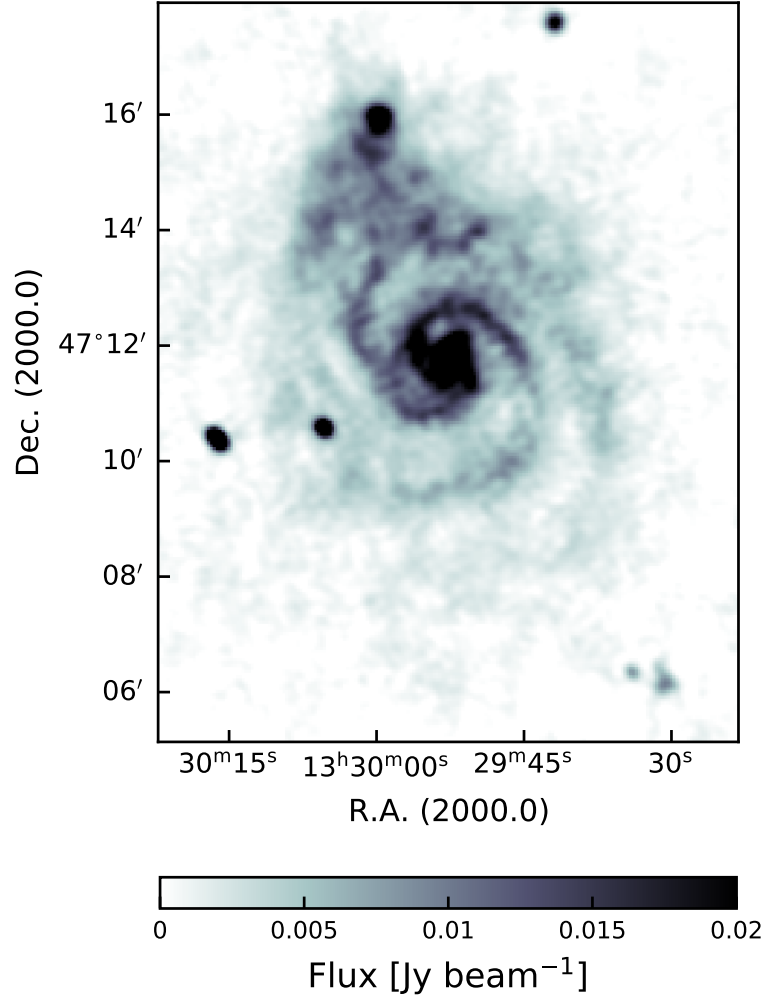


Figure 2.1: Radio continuum map of M 51 at 240 MHz observed with the GMRT. The map has an angular resolution of $14''.0 \times 12''.2$ and an rms noise of $500 \mu\text{Jy beam}^{-1}$.

2.2 Data handling

2.2.1 Observations with the Giant Metrewave Telescope

We analysed archival so far unpublished data of M 51 at 240 MHz, observed with the GMRT (Swarup et al. 1991) using the old hardware correlator (project code: 10AFA01). The map is presented here for the first time (see Fig. 2.1). The data were recorded by splitting the 16 MHz bandwidth into two bands of 8 MHz each, covered using 64 125 kHz wide channels, the upper and lower side bands, USB and LSB, respectively. We analysed only the USB data centred at 241.25 MHz because the LSB data were unusable due to radio frequency interference (RFI) and correlator-related errors. The total duration of these observations is 11 h, wherein 4 min scans on a nearby bright point source, 3C 286, were interleaved every 25 min. 3C 286 was used to calibrate the flux scale, bandpass, and phase. An additional 15 min scans on 3C 286 were performed at the beginning and end of the observations run.

In these observations, a total of 8.3 h was spent on M 51. The data were analysed in AIPS² using the standard analysis protocol at low frequencies. The data were manually inspected, and data that were affected by RFI and bad baselines were flagged using the TVFLG, WIPER, and SPFLG tasks. The task FLGIT was used to automatically remove RFI-affected frequency channels, which have a residual spectral flux above 4σ level. In these observations, less than $\approx 35\%$ of the data were found to be corrupted in the USB overall, including three non-working antennas and corrupted baselines. We used the Baars et al. (1977) absolute flux-density scale to determine a flux density of 29.5 ± 1.6 Jy at 241.25 MHz for 3C 286.³ RFI-removal and determining gain solutions were iteratively performed, and when the closure-phase errors determined using 3C 286 were below 1%, solutions were applied to the target M 51.

The task IMAGR was used to deconvolve the calibrated data. In order to minimise the effect of wide-field imaging with non-coplanar baselines, we used polyhedron imaging (Cornwell & Perley 1992) by subdividing the field of view ($\approx 3.7^\circ$) into $9 \times 9 = 81$ smaller facets. After flagging the first and last two channels, we vector-averaged four adjacent frequency channels of 125 kHz each into 15 500 kHz channels to ensure that the bandwidth smearing near 240 MHz was smaller than the size of the synthesized beam. Thus, the final image was made using a 7.5 MHz bandwidth. Five rounds of phase-only self-calibration were performed by choosing point sources above 8σ using the task CCSEL. The solution interval was progressively reduced during each round, starting from 3 min at the start to 0.5 min in the last round. Additional flagging was also performed after each round until in the fifth round, the closure-phase error was below 0.5%. To prepare the final image, we employed the SDI clean algorithm (Steer et al. 1984) to deconvolve the extended emission in M 51. After ensuring that point-like emission was cleaned using the BGC clean algorithm, SDI clean was used, and the clean-box masks were manually changed in order to deconvolve different scales. The final image at 240 MHz used in this work was produced at an angular resolution of $14''.0 \times 12''.2$ with an rms noise of $\approx 500 \mu\text{Jy beam}^{-1}$. While not a very sensitive map, it suffices for our analysis. The galaxy-integrated flux density of M 51 at 240 MHz within the 3σ contour is found to be 6.07 ± 0.63 Jy. Fig. 2.3 shows that the total flux density of M 51 agrees well with the flux densities in the literature when interpolated from higher- and lower-frequency observations.

The uncertainties on the estimated flux density depend on the absolute flux scale error and on the errors associated with uncalibrated system temperature (T_{sys}) variations (Basu et al. 2012). The absolute flux scale error for 3C 286 is found to be 5.4% (Baars et al. 1977), and the T_{sys} variation for the old GMRT system, as used for the observations in this paper, was estimated to be $\approx 5\%$ (Roy & Rao 2004). The overall systematic error, added in quadrature, is therefore expected to be $\approx 7.5\%$. We used a slightly more conservative value of 10% for the systematic flux error of the GMRT data. The statistical measurement error due to the rms noise in the map was added to this, but this contribution is relatively small.

2.2.2 Archival radio continuum observations

In total, radio continuum image data of M 51 were collected in nine different frequency bands between 54 MHz and 8350 MHz (see Table 2.2). All retrieved images were inspected for artefacts, and their integrated fluxes were cross-checked with literature values. Preferentially, single-dish or compact interferometric measurements were used to ensure that our images were not affected by the problem

²AIPS, the Astronomical Image Processing System, is free software available from the National Radio Astronomy Observatory.

³The flux density of 3C 286 obtained by Baars et al. (1977) is consistent with 28.15 Jy from the Perley & Butler (2017) absolute scale within the errors.

2 A spatially resolved radio spectral study of the galaxy M 51

Table 2.2: Observation parameters for the nine radio maps used in the analysis.

Telescope (Survey)	Central frequency [MHz]	Beam size	σ rms noise [μ Jy]	convolved σ_c rms noise [μ Jy]	Flux uncertainty ε_v [%]	Reference
LOFAR (LoLSS)	54	15''0 \times 15''0	1500	1500	10	1
LOFAR (LoTSS)	144	6''0 \times 6''0	45	100	10	2
GMRT	240	14''0 \times 12''2	500	850	10	3
GMRT	333	15''0 \times 15''0	200	350	10	4
GMRT ^a	619	5''7 \times 4''6	27	125	10	5
WSRT (SINGS)	1370	17''5 \times 12''5	22	25	5	6
WSRT (SINGS)	1699	13''5 \times 10''0	27	30	5	6
VLA + Effelsberg	4850	15''0 \times 15''0	30	30	5	7
VLA + Effelsberg	8350	15''0 \times 15''0	20	20	5	7

References: (1) de Gasperin et al. (2021); (2) Shimwell et al. (2022); (3) This work; (4) Mulcahy et al. (2016); (5) Farnes et al. (2013); (6) Braun et al. (2007); (7) Fletcher et al. (2011).

^(a) Map not used in the analysis due to possible deconvolution errors.

of missing spacing.

The lowest-frequency image at 54 MHz is from the LOFAR LBA Sky Survey (LoLSS; de Gasperin et al. 2021) using the low-band antennas. Flux calibrators were used to calibrate direction-independent effects as well as the bandpass response of the instrument. Additionally, the flux density of sources in the survey was compared to the Rees survey (8C; Hales et al. 1995) at 38 MHz, the VLA Low-Frequency Sky Survey redux (VLSSr; Lane et al. 2012) at 74 MHz, the LOFAR Two-metre Sky Survey data release 2 (LoTSS-DR2; Shimwell et al. 2022) at 144 MHz, and the NRAO VLA Sky Survey (NVSS; Condon et al. 1998) at 1400 MHz. A conclusive estimate of the flux density accuracy could not be derived, but it is suggested that assuming a conservative 10 % error on the LoLSS flux density scale is beneficial (de Gasperin et al. 2021). Heesen et al. (2022) investigated 45 nearby galaxies in LoTSS-DR2 that included M 51. We used their re-processed map of M 51. They confirmed that the integrated flux densities of the 6'' and 20'' maps are identical for the same integration area. This ensures that the high-resolution map that we used is sufficiently deconvolved. The flux densities from Heesen et al. (2022) were matched with the LoTSS-DR2 scale, whose error is below 10% (Shimwell et al. 2022). Therefore, we assumed a flux uncertainty of 10% for the LoTSS map.

The GMRT map at 333 MHz was already presented by Mulcahy et al. (2016). They used it for an analysis of the large-scale diffuse emission of M 51 and found no issues in relation to missing emission for the inner part of the disc. In contrast, the 619 MHz GMRT image of Farnes et al. (2013) showed a negative bowl around the diffuse emission of M 51, indicating deconvolution errors arising from missing emission. We therefore refrained from using the diffuse emission for further quantitative analyses. However, the bright emissions on small-scales, especially in the inner parts of the galaxy, might be less affected by missing-flux issues. The WSRT images at 1370 and 1699 MHz from Braun et al. (2007) were cross-checked with the VLA image at 1400 MHz published in Fletcher et al. (2011) and with literature flux density values. No differences in flux densities or morphology were

found. The WSRT-SINGS observations were bracketed by observations of the total intensity calibration sources, yielding an absolute flux density calibration accuracy better than 5% Braun et al. (2007). We therefore assume a 5% flux uncertainty for the WSRT maps here. Finally, the VLA images at 4850 and 8350 MHz were previously combined with single-dish Effelsberg telescope data, as described in Fletcher et al. (2011), so that we do not expect any missing flux. The flux measurement errors are usually assumed to be 5% for VLA data (Konar et al. 2013).

We convolved all images to the largest common beam of $17''.5 \times 15''.0$ (see Table 2.2) using the routine CONVOL of the software package called multichannel image reconstruction, image analysis, and display (MIRIAD, Sault et al. 1995). All images were then aligned to a common world coordinate system, re-gridded to a pixel size of $3''$, and transformed into the reference pixel and image size. This was achieved using the REGRID routine of MIRIAD. The rms noise, σ , of each individual image was determined by calculating the standard deviation over an emission-free area. For the further analysis, only pixels above 4.5σ were considered.

We assumed an absolute flux-scale uncertainty of 10% for the low-frequency data (for LOFAR and GMRT) and 5% for all other data (see Table 2.2). These estimates incorporate all errors and are conservative. There are several contributions. First, there is the accuracy of the absolute flux density of the calibrator models. This is 3–5% (Perley & Butler 2017). However, for spectral index studies like our work, the relative scale is more relevant, the uncertainty of which is about 1%. Deconvolution errors are about 1%, but increase at low signal-to-noise ratios (Offringa et al. 2014). The background noise can be neglected except for local measurements, where we added the rms noise in quadrature. Other errors, such as the uncertainty of the primary beam correction, can be also neglected as the primary beam size is much larger than the size of source. For the combined VLA and Effelsberg maps, the uncertainty is limited by the feathering procedure, with which the interferometric and single-dish images can be combined (Cotton 2017). Their uncertainty may be higher in areas of low signal-to-noise ratios, but we restrict most of our analysis to areas where this is not expected to cause a strong difference.

2.2.3 Integral field unit (IFU) spectroscopy

We complemented our radio continuum data with new optical IFU spectroscopy data from the Metal-THINGS survey (Lara-López et al. 2021). Metal-THINGS is a survey of nearby galaxies observing with the George Mitchell and Cynthia Spectrograph (GCMS; formerly known as VIRUS-P), mounted to the 2.7 m Harlan J. Smith telescope located at the McDonald Observatory in Texas. The IFU has a field of view of $100'' \times 102''$. Due to the large angular size of M51, a total of 12 pointings were needed to cover the entire galaxy. The spectroscopic data were processed with the spectral synthesis code STARLIGHT (Cid Fernandes et al. 2011) as described in Lara-López et al. (2021, 2023). We used an $H\alpha$ flux map corrected for extinction, where the correction was performed using the Balmer decrement. The map is shown in figure 2.2.

2.3 Data analysis

2.3.1 Integrated spectrum

We started our analysis by calculating the integrated spectrum, which helped us to assess the robustness of the data. The spectrum is plotted and compared to the integrated spectrum from Mulcahy et al. (2014) in Fig. 2.3. The integrated spectrum follows a power law with a spectral index of $\alpha = -0.80 \pm 0.05$ without any flattening at low frequencies. This is consistent with the spectral index

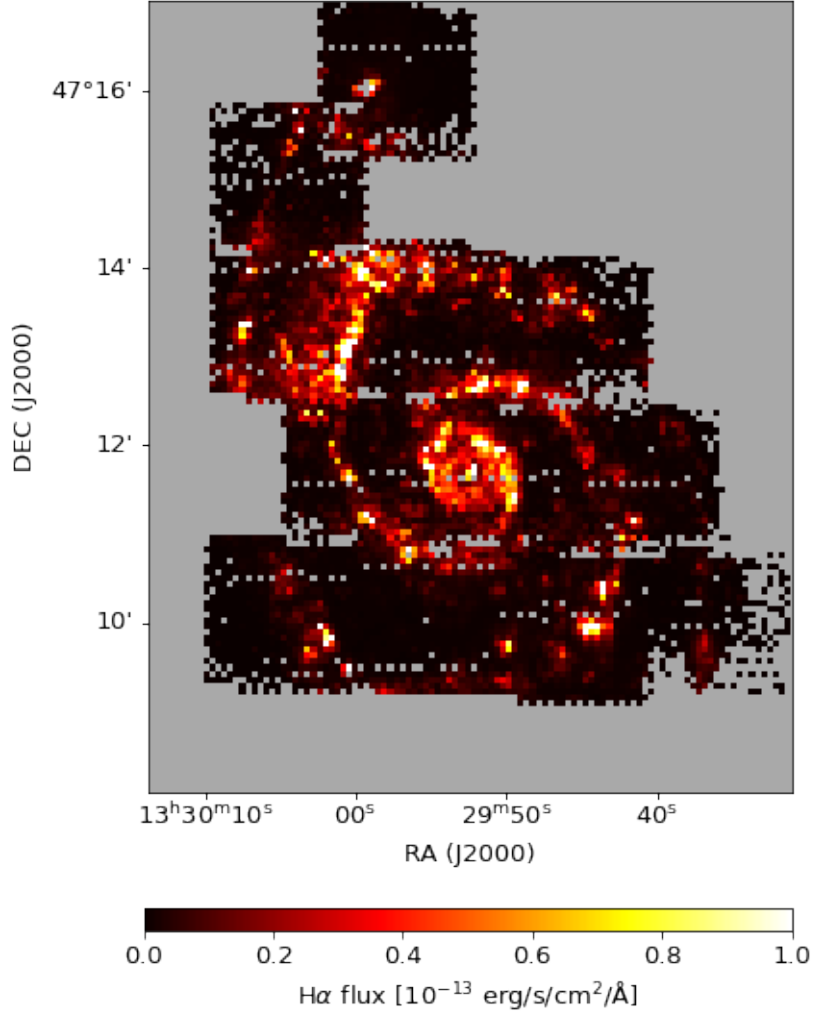


Figure 2.2: $H\alpha$ flux density map of M51 from the Metal-THINGS survey, corrected for extinction using the Balmer decrement. The grey pixels were not observed.

of -0.79 ± 0.02 calculated by Mulcahy et al. (2014). This test confirms that the integrated flux density of M51 in our maps matches previous observations.

2.3.2 Separation of thermal and synchrotron emission

To better determine the contribution of the thermal emission and separate the thermal from the non-thermal emission, we used $H\alpha$ to estimate the free-free emission in M51. To do this, we used a continuum-subtracted $H\alpha$ map obtained with the Kitt Peak National Observatory 2.1 m telescope using the narrow-band $H\alpha$ -filter KP1563 (Kennicutt et al. 2003a). The map was downloaded from the ancillary data at the SINGS webpage.⁴ The $H\alpha$ image, shown in Appendix A, has an angular resolution of $1''.35 \times 1''.35$ and an rms noise of $\approx 50 \mu\text{Jy beam}^{-1}$. Because the $H\alpha$ emission is easily absorbed by the dust, the observed $H\alpha$ intensity $I_{H\alpha, \text{obs}}$ needs to be corrected for foreground and internal extinction.

⁴<http://irsa.ipac.caltech.edu/data/SPITZER/SINGS/>

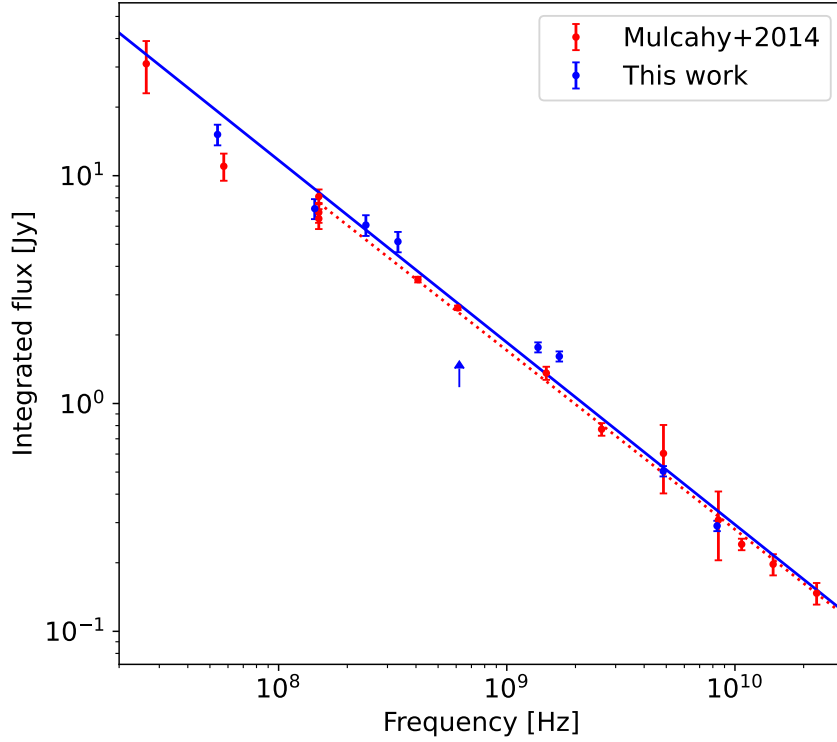


Figure 2.3: Global radio continuum spectrum of M 51. We show integrated flux densities calculated from our data and compare them with literature data compiled by Mulcahy et al. (2014). Power-law fits correspond to radio spectral indices of -0.80 ± 0.05 for our data (blue data points and solid line) and -0.79 ± 0.02 for the literature data (red data points and dotted line). The flux density at 619 MHz is only given as a lower limit and was not included in the fit.

The foreground extinction is low in the direction of M 51 (Schlafly & Finkbeiner 2011), and we therefore neglected it. The internal extinction within M 51 was corrected for with a $24 \mu\text{m}$ mid-infrared map to obtain an extinction-corrected $\text{H}\alpha$ emission line flux (Kennicutt et al. 2009),

$$F_{\text{H}\alpha} = F_{\text{H}\alpha, \text{obs}} + 0.02 \nu_{24\mu\text{m}} I_{24\mu\text{m}}. \quad (2.1)$$

Here, $I_{24\mu\text{m}}$ is the intensity at $24 \mu\text{m}$, and it was obtained from a *Spitzer* map observed as a part of the SIRTf Nearby Galaxies Survey (SINGS; Kennicutt et al. 2003a). The $24 \mu\text{m}$ map has an angular resolution of $6''$. We convolved the observed $\text{H}\alpha$ map to $6''$ and aligned it to the the same coordinate system as the $24 \mu\text{m}$ map.

The thermal contribution to the radio continuum emission at a given frequency ν can then be calculated using (Deeg et al. 1997)

$$\frac{S_{\text{th}}(\nu)}{\text{erg cm}^{-2} \text{s}^{-1} \text{Hz}^{-1}} = 1.14 \times 10^{-14} \left(\frac{\nu}{1000 \text{ MHz}} \right)^{-0.1} \left(\frac{T_e}{10^4 \text{ K}} \right)^{0.34} \left(\frac{F_{\text{H}\alpha}}{\text{erg cm}^{-2} \text{s}^{-1}} \right), \quad (2.2)$$

where T_e is the thermal electron temperature.

The electron temperature of the ionised gas phase is usually anti-correlated with the metallicity of the corresponding H II regions (Alloin et al. 1979; Pagel et al. 1979; Stasińska et al. 1981). Since

2 A spatially resolved radio spectral study of the galaxy M 51

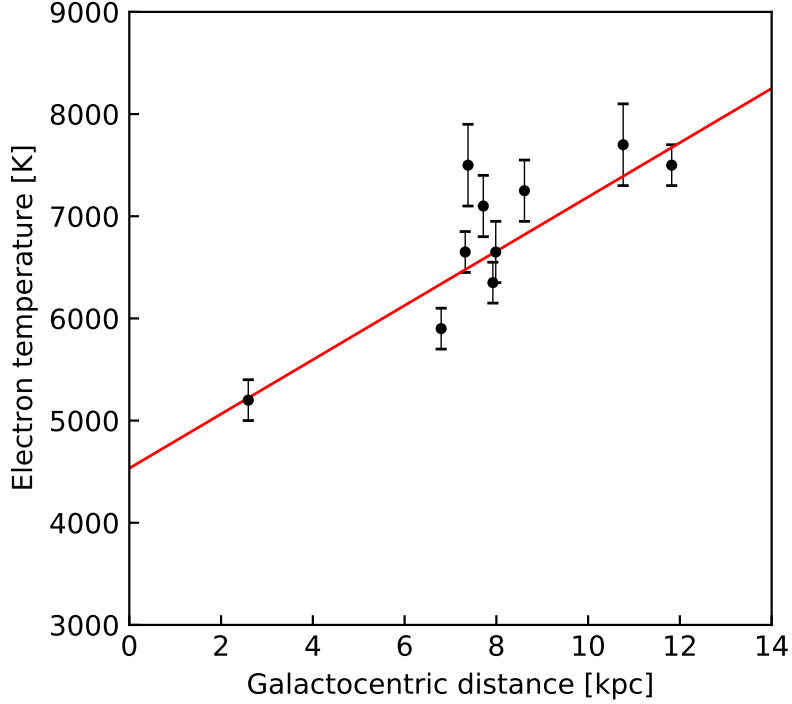


Figure 2.4: Electron temperature T_e measured in H II regions as a function of galactocentric distance R_{gal} . The data are taken from Bresolin et al. (2004). The red line represents the best linear fit.

the metallicity usually increases towards the galaxy centre, T_e decreases. In order to address the radial variation in T_e , we used the catalogue of H II regions in M 51 from Bresolin et al. (2004) and followed the linear fitting procedure of Tremblin et al. (2014) to calculate its radial profile. The data with the fit are shown in Fig. 2.4. The electron temperature T_e is found to follow the relation

$$\frac{T_e}{\text{K}} = (266 \pm 47) \left(\frac{R_{\text{gal}}}{\text{kpc}} \right) + (4533 \pm 374), \quad (2.3)$$

where R_{gal} is the galactocentric distance. We note here that the T_e measured in Bresolin et al. (2004) was derived from auroral lines, which can only be detected in low-metallicity H II regions. This could cause a bias towards higher temperatures in our profile because temperature and gas metallicity are anti-correlated, and for higher metallicities, auroral lines can no longer be detected. However, the overall radial dependence should still represent the average electron temperature in the H α gas.

The extinction-corrected H α map was then convolved to our common beam of $17''.5 \times 15''.0$, and re-gridded to the same coordinate system as the radio maps. For each pixel of a radio continuum map at a given frequency ν , the thermal flux density was calculated using Eq. (2.2) and T_e from Eq. (2.3). The calculated thermal flux densities (Appendix A) were subtracted from the total flux densities in our radio maps. The resulting non-thermal maps were used for the majority of the following analysis.

We found thermal contributions between 0.98% and 4.8% at 54 MHz, and between 12% and 14% at 8350 MHz. For a relative error of ε_{th} in the estimated thermal fraction f_{th} , the relative error in the synchrotron emission fraction ($\sigma_{f_{\text{nth}}}$; where $f_{\text{nth}} = 1 - f_{\text{th}}$) is given by $\sigma_{f_{\text{nth}}} = [1 - (1 \pm \varepsilon_{\text{th}}) f_{\text{th}}] / [1 - f_{\text{th}}]$ (Basu et al. 2017).⁵ This means that an error of up to 20% ($\varepsilon_{\text{th}} = 0.2$) in a region with $f_{\text{th}} =$

⁵The relative error of the thermal fraction f_{th} is defined as $\varepsilon_{\text{th}} = \sigma_{f_{\text{th}}} / f_{\text{th}}$, where $\sigma_{f_{\text{th}}}$ is the absolute error of f_{th} .

0.15 (0.05) will propagate to an error of about 5 (2) % in the estimated synchrotron emission. Adding this (in quadrature) to the flux uncertainty will increase it from 5(10) % to 6.6(10.2) % assuming an exaggerated error of 20% on the thermal fraction. Because of this, the error on the thermal fraction does not significantly affect the results presented in the rest of this paper.

2.3.3 Spiral arm, inter-arm, and galaxy core regions

Previous work (Fletcher et al. 2011) has shown the radio continuum spectrum to be different depending on the location in the galaxy. In spiral arms, the radio spectral index indicates a flat non-thermal spectrum, whereas the inter-arm regions have steeper spectra. Moreover, the radio continuum emission depends on the star formation rate (SFR), and this relation of radio to SFR is different in the arm and inter-arm regions. We therefore now define arm- and inter-arm regions using the distribution of the atomic and molecular gas.

We decided to follow the approach of Hitschfeld et al. (2009) using a combination of H I and CO maps to generate a gas surface density map, which then represented the spiral arm structure tracing the density waves (Colombo et al. 2014). To this end, we used the integrated H I map (moment 0) from Walter et al. (2008) and the integrated ^{12}CO 2-1 map from Schuster et al. (2007). Both maps were convolved to our common resolution of $17''.5 \times 15''.0$. We calculated the H I column density N_{HI} using (Meyer et al. 2017)

$$N_{\text{HI}} = 1.10 \times 10^{24} \text{ cm}^{-2} \left(\frac{S_{\text{HI}}}{\text{Jy km s}^{-1}} \right) \left(\frac{a \times b}{\text{arcsec}^2} \right)^{-1}, \quad (2.4)$$

where S_{HI} is the velocity-integrated H I flux density, and a and b are the major and minor axis of the synthesised beam, defined as the full width at half maximum, respectively.

In order to convert the CO map into an H₂ column density map, we used (Schuster et al. 2007)

$$N_{\text{H}_2} = 0.25 \frac{X_{\text{MW}}}{0.8} \frac{T_{\text{CO}}}{\text{K km s}^{-1}}, \quad (2.5)$$

where $X_{\text{MW}} = 2.3 \times 10^{20} \text{ cm}^{-2} (\text{K km s}^{-1})^{-1}$ is the CO-to-H₂ conversion factor as determined for the Milky Way (Schuster et al. 2007), and T_{CO} is the velocity-integrated CO intensity, given as main beam antenna temperature. The factor 0.8 reflects the assumed 2-1/1-0 CO intensity ratio.

The atomic and molecular gas maps were first converted into their corresponding mass surface densities. To convert from the observed integrated intensities into the total gas surface densities, we used the relation $\Sigma_{\text{gas}} = 1.36 (\Sigma_{\text{HI}} + \Sigma_{\text{H}_2})$, which takes the mass contribution from He into account. The distribution of Σ_{gas} is presented in Fig. 2.5. As in Hitschfeld et al. (2009), we used a total mass surface density threshold in order to define the spiral arm regions. These regions were chosen to be similar to those in interferometric CO maps, in H α maps, and in 1400 MHz radio continuum maps. All pixels with $\Sigma_{\text{gas}} > 25 M_{\odot} \text{ pc}^{-2}$ were attributed to the spiral arm regions and pixels with $8 M_{\odot} \text{ pc}^{-2} \leq \Sigma_{\text{gas}} \leq 25 M_{\odot} \text{ pc}^{-2}$ were attributed to the inter-arm regions. We defined two additional regions in the cores of M 51 and NGC 5195 with a radius of $25''$. The resulting map and the defined regions are shown in Fig. 2.5.

2.3.4 Non-thermal radio spectral index and curvature

In the next step, we explored the observed non-thermal radio continuum spectra in different regions of the galaxy on a point-by-point basis. We fitted a model spectrum consisting of a power law and a

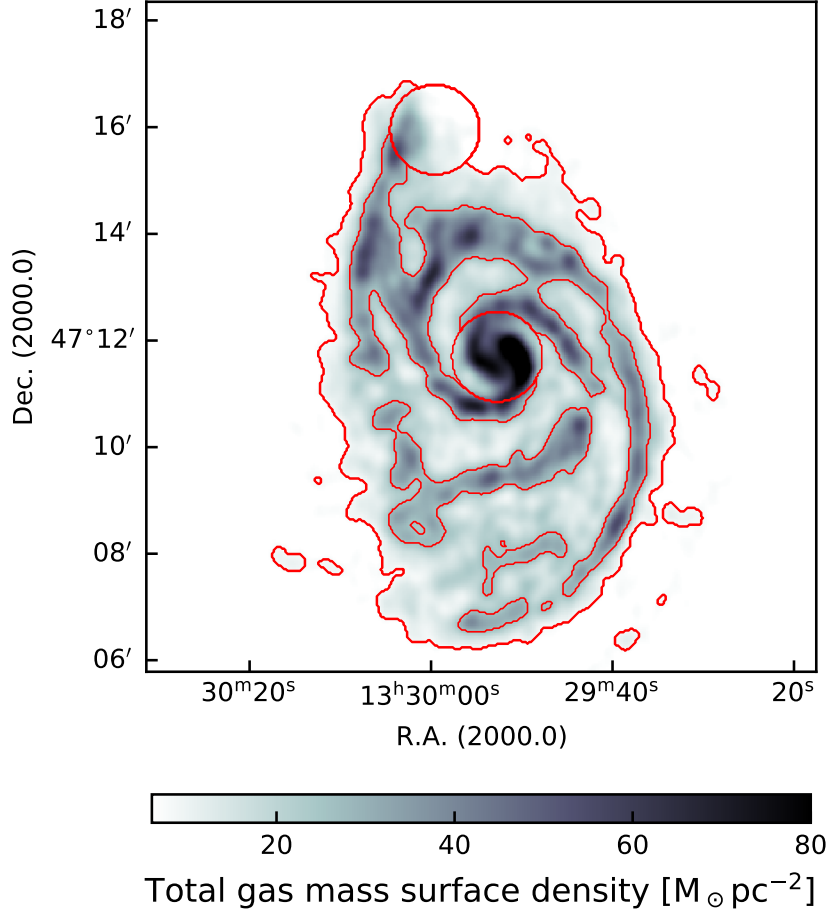


Figure 2.5: Total gas-mass surface density as derived from a combination of atomic (H I) and molecular (H₂) gas maps. The contours at 8 and 25 M_⊙ pc⁻² define the borders of the spiral arm and inter-arm regions, respectively. The circular apertures denote the core regions in M 51 and NGC 5195.

curvature component using a polynomial equation in logarithmic space (Perley & Butler 2013, 2017),

$$\log S_\nu = \log S_0 + \alpha_0 \log(\nu/\nu_0) + \beta [\log(\nu/\nu_0)]^2, \quad (2.6)$$

where S_ν is the flux density at a given frequency, ν is in GHz, S_0 is the flux density at the normalisation frequency $\nu_0 = 1$ GHz, α_0 is the non-thermal radio spectral index, and β the non-thermal radio spectral curvature. We note that $\beta < 0$ corresponds to a concave spectrum. The non-thermal radio spectral index α_0 needs to be defined at a single reference frequency because the spectral slope is frequency dependent in case of a curved spectrum. We started with this purely phenomenological model in order to explore the general shape of the spectrum without a bias towards a specific physical mechanism. We explore the underlying physics responsible for the shape of the spectrum in Sect. 2.4.

For each point in the maps, we fitted this model to eight data points at the frequencies listed in table 2.2 (excluding 619 MHz). For simplicity, we ignored higher-order terms, and a more sophisticated modelling of the spectra needs to be deferred to future work. The data were fitted with a Levenberg–Marquardt least-squares algorithm. The resulting maps of best-fit α_0 and β and their corresponding error maps are shown in Fig. 2.6. The reduced χ^2 of the fit is shown in Fig 2.7. The resulting parameter

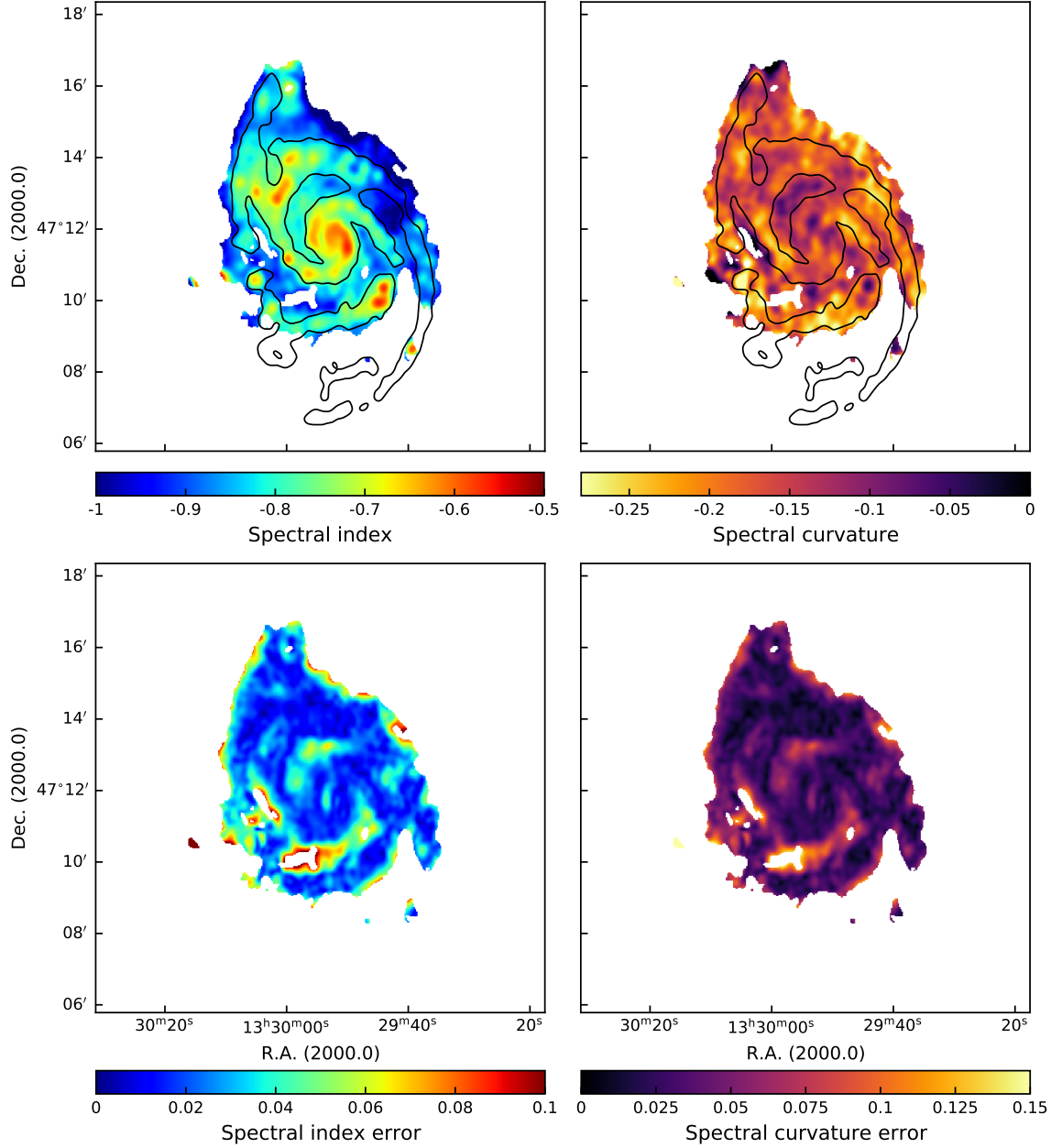


Figure 2.6: Non-thermal radio spectral index and curvature at 1 GHz. Top panels: Best-fit radio spectral index α_0 (left panel) and spectral curvature (right panel). The bottom panels show the corresponding uncertainty maps of the radio spectral index (left panel) and curvature (right panel). The black contours represent a total gas-mass surface density $25 M_{\odot} \text{pc}^{-2}$.

values were restricted to the frequency range between 54 and 8350 MHz and cannot be extrapolated towards arbitrary high or low frequencies.

The non-thermal radio spectral index at 1 GHz has values between -1.0 and -0.5 . The flatter radio spectra (α_0 from -0.7 to -0.5) are mostly found along the spiral arms, where the star-forming regions are located. The inter-arm regions have radio spectral indices between -1.0 and -0.8 . The tidal bridge region between M 51 and NGC 5195 (located north of M51) is characterised by a similarly

2 A spatially resolved radio spectral study of the galaxy M51

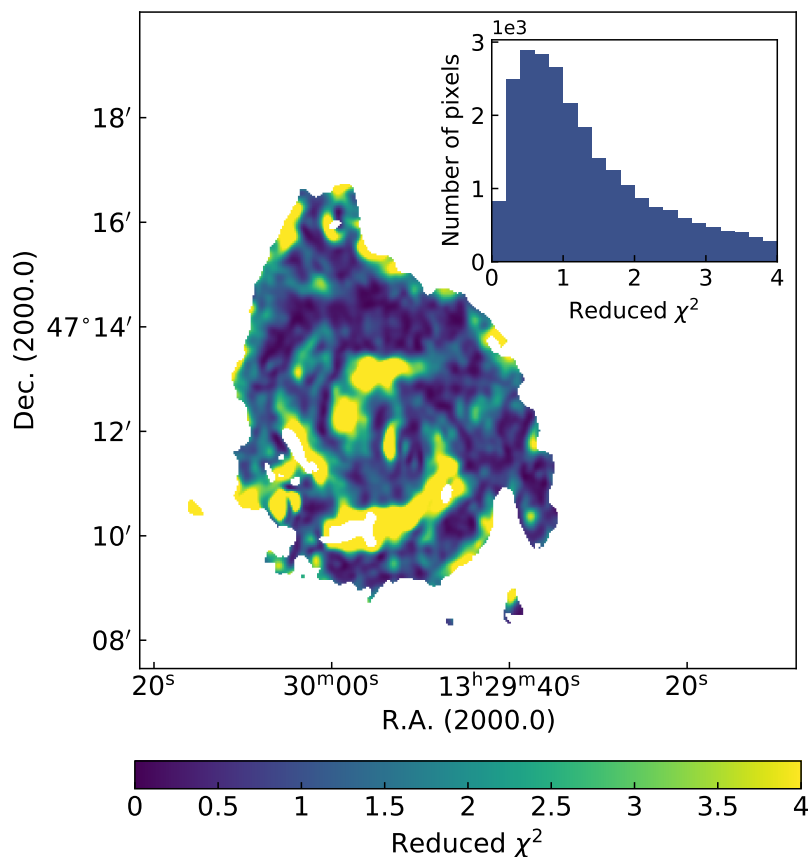


Figure 2.7: Map of the reduced χ^2 of the fit presented in Fig. 2.6. The inset in the top right corner shows the histogram of the reduced χ^2 values.

steep radio spectrum, whereas the spectrum flattens again towards the companion with spectral indices of $\alpha_0 \approx -0.7$. The errors usually lie below 0.04 and only rise to 0.10 in regions with lower signal-to-noise ratios. Our radio spectral index map is very similar to the 1400–4850 MHz map by Fletcher et al. (2011), who used a 1400 MHz map from the VLA instead of the WSRT map (and the same 4850 MHz map we used). Our radio spectral index is defined at a lower frequency of 1 GHz, and the deviations of 0.1–0.2 therefore become apparent in regions in which the absolute value of the spectral curvature is high.

The spectral curvature is negative, with values between -0.3 and 0.0 . This means that the radio spectrum is concave, implying a suppression of radio emission at either low or high frequencies, or a combination of both. The suppression of the radio emission at low frequencies can be caused by free–free absorption, ionisation losses, or synchrotron self-absorption, and at high frequency, it can be caused by CR radiation losses (Longair 2011). We further explored the process that causes the observed curvature in Sect. 2.4. Regions with flatter radio spectra tend to show stronger curvatures ($\beta \leq -0.2$). The errors for the curvature are usually smaller than 0.06; only in regions with lower signal-to-noise ratios do they rise to 0.14. The reduced χ^2 is smaller than one in most of the galaxy. The value is higher in the areas in which the error on the fit parameters is also high. The areas in which the model does not fit the data so well are also less strongly curved. We assume that a better model in these areas would be just a power law.

2.3.5 Low- and high-frequency non-thermal radio spectral indices

We now study the non-thermal spectral index at both low and high frequencies. We compared the two-point low-frequency radio spectral index α_{low} between 54 and 144 MHz with the two-point high-frequency spectral index α_{high} between 1370 and 4850 MHz. The two-point spectral indices were calculated in a standard way by taking the logarithmic ratio of the flux densities in two maps over the logarithmic frequency ratio. The errors in the spectral index maps were calculated by propagating the errors from the individual maps, which are a combination of the flux error (listed in Table 2.2) and the rms noise measured away from the source. The two-point spectral index maps are shown in Fig. 2.8. We did not select the two highest frequencies because the galaxy at 8350 MHz is smaller, which would prevent us from studying the radio spectral index of the diffuse emission further in the outskirts of M 51. Additionally, skipping the 8350 MHz map gives a higher ratio between frequencies, which results in a more reliable spectra index map.

The maps of α_{low} and α_{high} have a similar morphology at first glance, but α_{low} is systematically higher than α_{high} . The values for α_{low} reach from -0.7 to 0.2 , with errors in the range of 0.17 – 0.25 . In contrast, the values for α_{high} reach from -1.3 to -0.6 , with errors in the range of 0.05 – 0.15 . Higher errors for the low-frequency spectral index are expected because of the higher calibration error and noise in these maps. The errors are also higher at the edges of the maps because the signal-to-noise ratio is lower. The higher values of $\alpha_{\text{high}} \approx -0.7$ correlate well with the spiral arm structure of M 51, which was reported by Fletcher et al. (2011). The values of α_{low} are similarly distributed, although the spiral arms are more diffuse and have an inverted radio spectrum, as indicated by radio spectral indices with values of up to ≈ 0.2 . Because of the cosmic-ray radiation losses of the CR electrons, we expect a steepening at the edges of the galaxy. This is shown in the α_{low} map, even though it might not be completely reliable because the signal-to-noise ratio is low in these regions. We attribute the strong flattening of the radio spectrum at higher frequencies towards the extreme north and south as visible in the map of α_{high} as spurious. The strong spurious flattening is likely due to the limitations of combining the interferometric and single-dish data (Cotton 2017). These data do not affect our results because they lie beyond the region of interest that we considered for our analysis.

As the results of fitting for spectral index and curvature already suggested (Fig. 2.6), the spectral index flattens overall towards lower frequencies for the whole inner disc of M 51. In the following, we discuss the effects that might cause these flat and partially inverted spectra.

2.4 Spectral index flattening and low-frequency turnovers

Changes in the spectral indices over frequency may be due to a number of reasons. In the following, we investigate the plausible mechanisms that can alter the radio continuum spectrum from a power-law to a concave spectrum. This can either be done by changing the cosmic-ray electron spectrum or by directly absorbing low-frequency radio emission. Previous work has shown (Heesen et al. 2023, 2024a) that the diffusion coefficient of GeV CR electrons is independent of energy, at least over the relevant energy range. Hence, we do not expect diffusion to change the spectrum. Moreover, advection does not change the spectrum. Hence, we now consider cosmic-ray radiation losses, synchrotron self-absorption, thermal free–free absorption, and cosmic-ray ionisation losses.

2.4.1 Cosmic-ray radiation losses

In regions with low gas densities, cosmic-ray electrons lose their energy due to synchrotron and inverse-Compton radiation losses, causing their spectra to age, that is, to steepen.

2 A spatially resolved radio spectral study of the galaxy M51

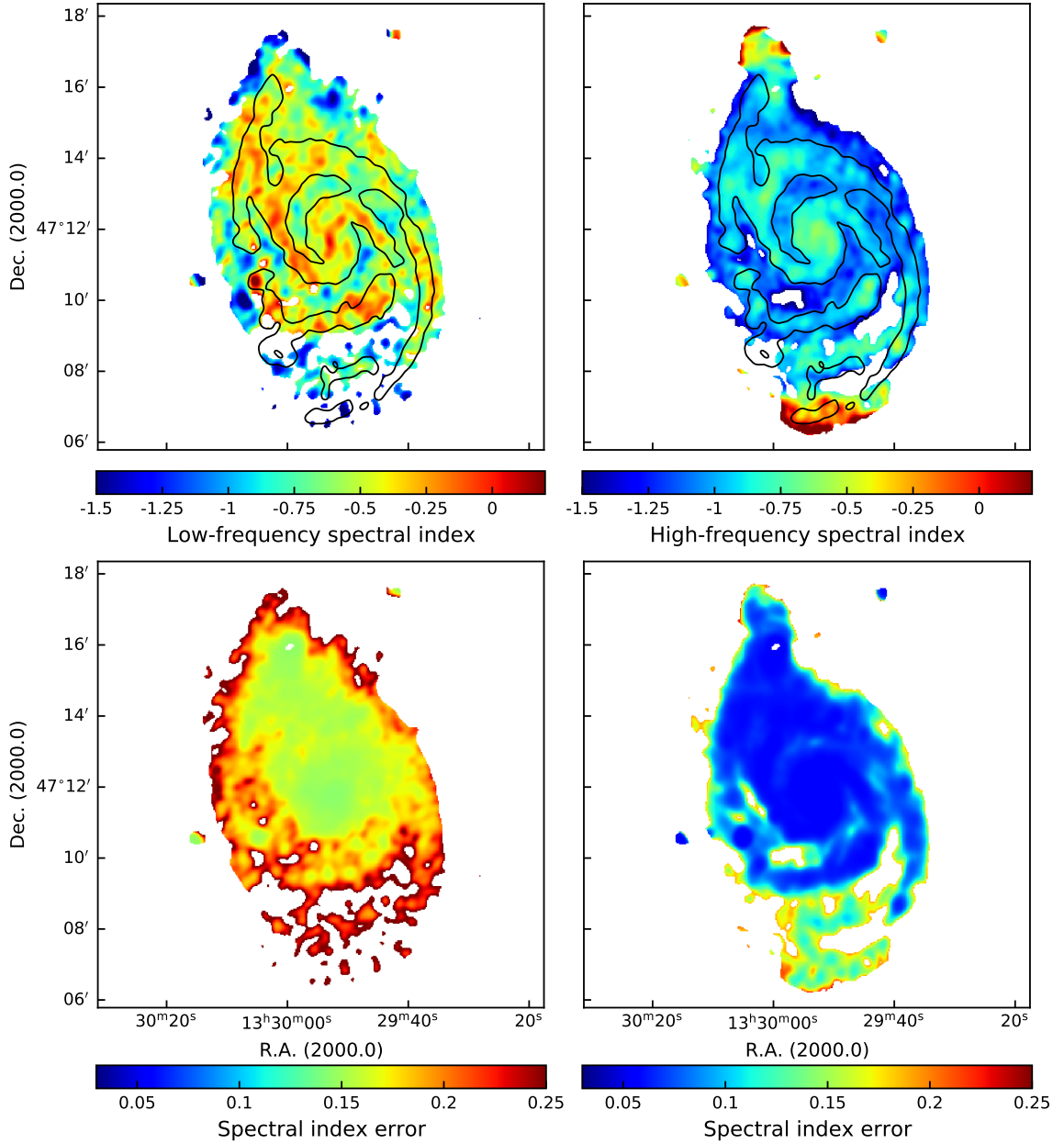


Figure 2.8: Two point non-thermal radio spectral indices at low (α_{low} ; 54–144 MHz) and high (α_{high} ; 1370–4850 MHz) frequencies. The top panels show the spectral indices α_{low} (left panel) and at α_{high} (right panel). The bottom panels show the corresponding uncertainty maps. The black contours represent a total gas-mass surface density $25 M_{\odot} \text{pc}^{-2}$.

In particular, spectral ageing predominantly affects the high-frequency radio spectral index (Sect. 2.3.5). Near star-forming regions, the values of $\Delta\alpha = \alpha_{\text{low}} - \alpha_{\text{high}}$ are lower (between 0.2 and 0.5) than in the inter-arm regions, where they are between 0.8 and 1.1. A proper modelling of CR ageing is not possible with the data, but we can make a few qualitative observations. Fig. 2.6 clearly shows that the curvature is high, and the spectral index is lower in regions with low star formation, that is, in the inter-arm regions. Inside the spiral arms, the synchrotron emission at low frequencies is likely to

be a mix of recently accelerated CR electrons and those from previous nearby sites of star formation, which fall within a resolution element. However, this is not true in the inter-arm regions, where the star formation is low. The data resolution is approximately $16''$, that is, 650 kpc. If we assume that the bulk of the CR electrons are produced in the arms, then CR electrons with energies lower than about 1.5 GeV will be able to diffuse to scales larger than 650 kpc (assuming $B = 10 \mu\text{G}$, and $D = 2 \cdot 10^{28} \text{ cm}^2/\text{s}$). This corresponds to CR electrons that are emitted at critical frequencies of 600-700 MHz. Hence, CR electrons emitting above 1 GHz lose energy before they can mix, especially in the inter-arm regions. Even in regions with a low star formation, the local CR electron injection timescale is much longer than the ageing timescale. This is quantitatively shown in Fig. 3 of Basu et al. (2015) in order to explain the steep spectra in low-density regions. This argument is also supported by the spatially resolved radio-FIR relation (see Fig. 5 and Section 4 of Basu et al. 2012).

2.4.2 Synchrotron self-absorption

Synchrotron self-absorption is known to play a key role in the flattening of spectra in the inner cores of active galactic nuclei (AGN). We used the equation from Lacki (2013) to determine the turnover frequency ν_{SSA} for integrated spectra of galaxies,

$$\nu_{\text{SSA}} = 2.4 \text{ MHz} \left(\frac{\Sigma_{\text{SFR}}}{50 \text{ M}_{\odot} \text{ yr}^{-1} \text{ kpc}^{-2}} \right)^{0.39}, \quad (2.7)$$

where Σ_{SFR} is the star formation rate surface density. With a value of $\Sigma_{\text{SFR}} = 0.9$ from González-Lópezlira et al. (2013), we calculate a value of $\nu_{\text{SSA}} = 0.5 \text{ MHz}$. This value is lower by more than two orders of magnitude than our lowest observing frequency. Therefore, synchrotron self-absorption cannot be the dominant effect causing the flattening.

Similarly, diffuse large-scale structures in nearby galaxies are not very likely to be affected by synchrotron self-absorption because the required magnetic field strength is high. We can calculate this magnetic field strength B_{SSA} for a given frequency ν in GHz and brightness temperature T_{b} in K using the standard equation

$$B_{\text{SSA}} \approx 1.4 \cdot 10^{21} \nu T_{\text{b}}^{-2}. \quad (2.8)$$

T_{b} is defined as

$$T_{\text{b}} = 1.222 \cdot 10^3 \frac{I}{\nu^2 \theta_{\text{maj}} \theta_{\text{min}}} \text{ K}, \quad (2.9)$$

with the brightness I in Jy/beam and θ_{maj} and θ_{min} the synthesised major and minor beam half-power beam widths in arcseconds, respectively. When we insert our beam size of $17.5'' \times 15''$ and a brightness of 150 mJy/beam as a maximum at 54 MHz, the resulting magnetic field is $1.3 \times 10^{15} \text{ G}$. From equipartition calculations, we know that the typical magnetic field strength in nearby galaxies is $9 \mu\text{G}$ (Beck & Krause 2005) with maximum values for extreme starburst cases such as M 82 of $100 \mu\text{G}$ (Adebahr et al. 2013). Lacki (2013) discussed the possible turnover frequency for extreme starburst cases, which would be about $\nu_{\text{SSA}} = 2.4 \text{ MHz}$. These results show that synchrotron self-absorption cannot play an important role in the flattening of the spectra at low frequencies in M 51.

2.4.3 Thermal free-free absorption

Free-free absorption is an effect caused by an ionised medium that absorbs radio waves while they propagate through it. The amount of absorption depends on the thermal electron number density n_e ,

2 A spatially resolved radio spectral study of the galaxy M 51

the path length, and the frequency, such that the optical depth increases with decreasing frequency. Free–free absorption has been observed at frequencies below 500–1000 MHz in the core regions (Adebahr et al. 2013; Varenius et al. 2016) and individual star-forming regions (Wills et al. 1997; Varenius et al. 2015; Basu et al. 2017) of starburst galaxies, and also in the Milky Way (Rishbeth 1958; Roy & Rao 2004). Observations at very low radio frequencies also showed a turnover for the global spectrum of the Milky Way at about 3 MHz (Brown 1973).

In the following, we investigate whether free–free absorption can explain the flattening of the radio spectrum towards lower frequencies. Following Wills et al. (1997), the spectrum in case of free–free absorption of sources inside an ionised medium is

$$S_\nu = S_0 \nu_0^\eta e^{-\tau_{\text{ff}}}, \quad (2.10)$$

with η the radio spectral index of the optically thin medium, and τ_{ff} the free–free emission optical depth. In the expression for the free–free Gaunt factor at radio wavelengths from Lequeux (2005), the optical depth is given as

$$\tau_{\text{ff}} = 8.2 \times 10^{-2} \nu_0^{-2.1} T_e^{-1.35} \text{EM}, \quad (2.11)$$

with the emission measure (EM) in units of $\text{cm}^{-6} \text{pc}$ and the electron temperature T_e in K. The EM is defined as

$$\left(\frac{\text{EM}}{\text{pc cm}^{-6}} \right) = \int_0^{s_0} \left(\frac{n_e}{\text{cm}^{-3}} \right)^2 \left(\frac{ds}{\text{pc}} \right), \quad (2.12)$$

where n_e is the thermal free electron density, and s is the distance along the line of sight between the source at s_0 and an observer at 0. The absorption model (Eq. 2.10) was used to fit the spectrum of M 51. We then derived the EM using Eq. (2.11), where we inserted the electron temperature as expressed by the galactocentric distance (Eq. 2.3).

Local radio continuum spectra

We first investigated the effect of free–free absorption on our radio continuum spectra by analysing the integrated flux densities within the four regions of the arm, inter-arm, and the two cores of M 51 and NGC 5195 (Sect. 2.3.3). The thermal emission that we previously subtracted is also affected by free–free absorption. However, the absorption of the thermal radio continuum can be ignored because free–free absorption is only significant at low frequencies, where the thermal fraction is very low. Similarly, at high frequencies, free–free absorption is negligible. We can therefore justify using the non-thermal maps as produced above for the fitting and neglect the effect of free–free absorption on the thermal emission. For comparison, we also fitted the polynomial model (Eq. 2.6) to the non-thermal radio continuum spectra (after thermal subtraction) in the four regions. The flux density error was estimated by assuming a statistical error caused by the map noise σ_{rms} , as well as a relative flux uncertainty ε_ν due to calibration uncertainty (see Table 2.2). The error of the flux density measurements at each frequency was calculated using the following expression (Heesen et al. 2022):

$$\sigma_{S_\nu} = \sqrt{\left(\sigma_{\text{rms}} \sqrt{N_{\text{beams}}} \right)^2 + (\varepsilon_\nu S_\nu)^2}, \quad (2.13)$$

where S_ν is the flux density, and N_{beams} is the number of beams in the integration region.

Figure 2.9 shows the measured spectra within the regions together with the best-fitting absorption models. We show additional point spectra in Appendix B. The flattening of the spectra at low frequencies is highlighted by comparing the spectrum to a power law. The resulting parameters are

2.4 Spectral index flattening and low-frequency turnovers

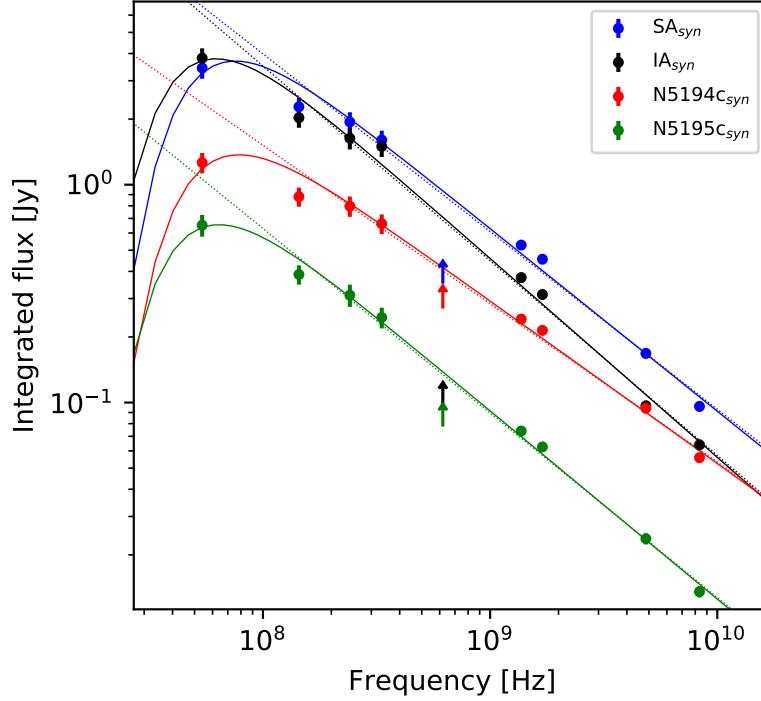


Figure 2.9: Non-thermal radio continuum spectra for the spiral arm (SA), inter-arm (IA), and core regions (N5194c and N5195c). The flux densities at 619 MHz are only given as lower limits and are not included in the analysis. The solid lines are the best-fitting free–free absorption models (Eq. 2.10). The dotted lines show the power-law fits for frequencies ≥ 144 MHz.

Table 2.3: Fitted parameters for the spectra of the spiral arm (SA), inter-arm (IA), and core (N5194c, N5195c) regions.

Region	S_0 [Jy]	η	EM [pc cm $^{-6}$]	S_0 [Jy]	α_0	β
SA _{syn}	0.630±0.036	−0.839±0.039	2800±990	0.697±0.013	−0.777±0.0089	−0.176±0.013
IA _{syn}	0.459±0.026	−0.914±0.041	2000±790	0.507±0.026	−0.881±0.024	−0.147±0.034
N5194c _{syn}	0.293±0.014	−0.746±0.032	2710±980	0.3119±0.0071	−0.674±0.012	−0.144±0.016
N5195c _{syn}	0.0917± 0.0036	−0.865±0.027	2040±570	0.09924± 0.0021	−0.821±0.0097	−0.132±0.014

Columns (2)–(4) list the free–free absorption, and Columns (5)–(7) list the curved spectral model. Both are fitted to the non-thermal radio continuum spectra.

listed in Table 2.3. The radio spectral indices η lie between -0.91 and -0.75 . For the polynomial fits, we find non-thermal radio spectral indices at 1 GHz between -0.88 and -0.67 .

We find that the EM has values between 2000 and 2800 cm $^{-6}$ pc. They mostly show the same tendency as the absolute values of the spectral curvature because the higher EM values are seen in the spiral arm regions and the lower values in the inter-arm regions. However, the EM values do not greatly differ statistically because the uncertainties are large.

2 A spatially resolved radio spectral study of the galaxy M 51

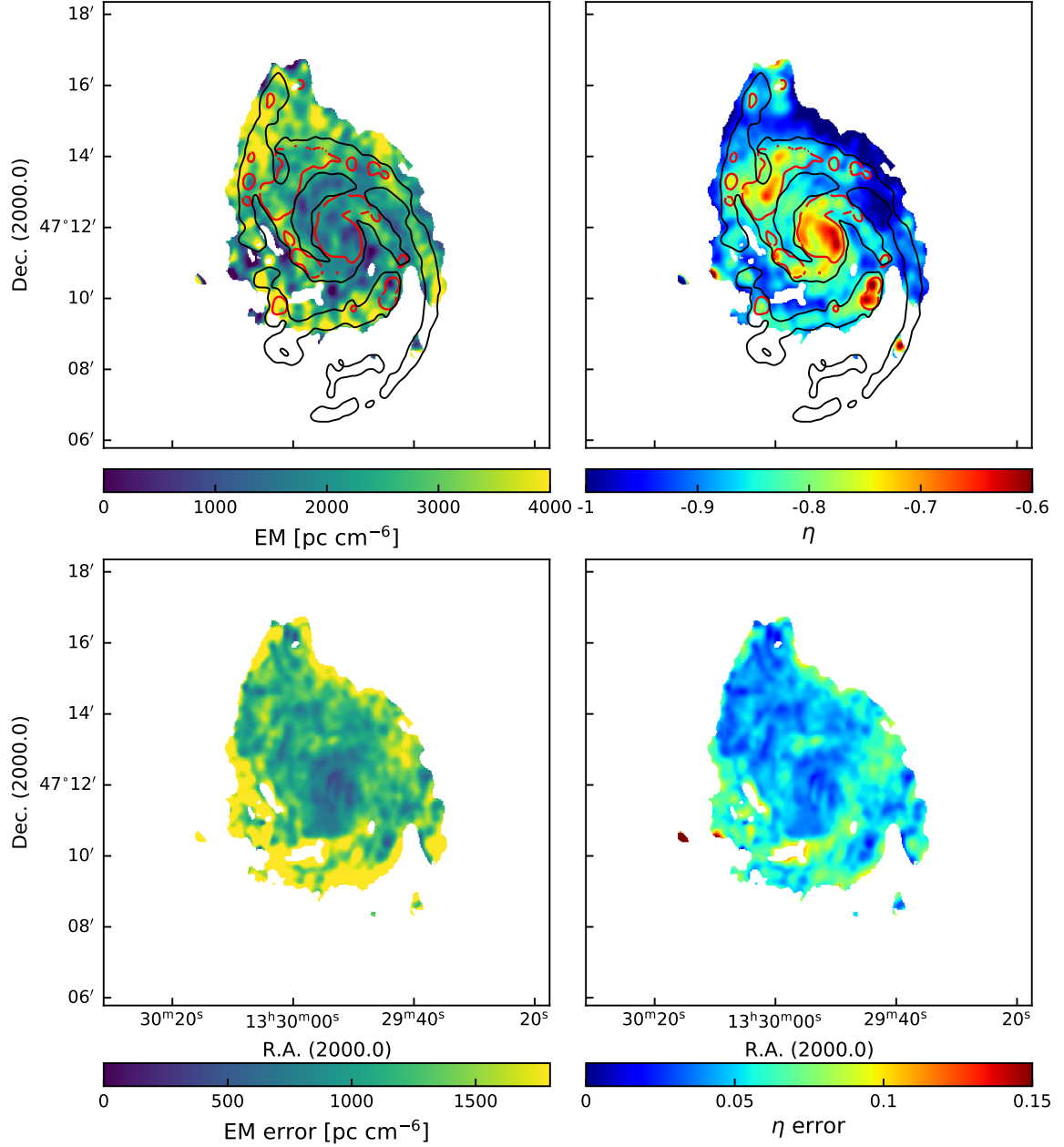


Figure 2.10: Thermal free–free absorption. Results from fitting the thermal absorption model to the non-thermal radio continuum emission at eight frequencies between 45 and 8350 MHz (Table 2.2). The left column shows the resulting EM map (top panel) and its uncertainty map (bottom panel). The right column shows the radio spectral index of the optically thin medium η (top panel) and its uncertainty map (bottom panel). The red contours represent the H α flux value of $2.6 \cdot 10^{-13} \text{ erg s}^{-1} \text{ cm}^{-2} \text{ \AA}^{-1} \text{ beam}^{-1}$ from the Metal-THINGS survey. The black contours represent a total gas-mass surface density $25 M_{\odot} \text{ pc}^{-2}$.

Emission measure and radio spectral index

We now investigate the free–free absorption on a point-by-point basis in order to determine the spatial distribution of the EM. For each point in the radio maps, we fitted the free–free absorption model (Eq.

2.4 Spectral index flattening and low-frequency turnovers

2.10) to eight data points at the frequencies listed in table 2.2 (excluding 619 MHz). We assumed the electron temperature from Eq. 2.3. The parameters of the model were the spectral index η and the EM. We present the resulting maps in Fig. 2.10. In general, regions with higher gas densities (the spiral arms) show flatter spectral indices and a slightly higher EM. While the steeper spectral index in the inter-arm regions can be explained by radiation losses of the cosmic-ray electrons during propagation away from their places of origin in the star-forming regions, the significant flattening in the spiral arms and in the cores of NGC 5194 and 5195 is difficult to explain without thermal absorption effects. The spectra presented in Fig. 2.9 show that the 54 MHz data points have much lower flux densities than what would be expected if the emission were to follow a power law. This is an indication of a flattening at low frequencies that is at least in part caused by free-free absorption.

We used the $H\alpha$ flux density map obtained using IFU spectroscopy to calculate an independent EM estimate. We first convolved the data to the same beam as the radio maps. To calculate the EM, we used the equation (Dettmar 1992)

$$EM = 5 \cdot 10^{17} F_{H\alpha} / \Omega \text{ cm}^{-6} \text{ pc}, \quad (2.14)$$

where $F_{H\alpha}$ is the measured flux in $\text{erg cm}^{-2} \text{ s}^{-1}$, and $\Omega = 1.133 \cdot 17''.5 \times 15''.0$ is the collecting area in \square'' calculated for our beam.

We compared the EM from the $H\alpha$ flux density to the EM obtained by fitting the free-free absorption model to the radio data by plotting them against each other in Fig. 2.11. In contrast to our expectation, we see no correlation, with a Spearman rank correlation coefficient of $\rho_s = -0.04$. Free-free absorption might therefore not be the main mechanism for the low-frequency flattening that we observe (see Sect. 2.4.4). An alternative reason could be that $H\alpha$ directly traces the clumpy ionised gas, while the EM estimated from the radio spectrum also receives a contribution from the diffuse gas. The latter is known as the diffuse ionised gas that fills the space between the $H \text{ II}$ regions (Haffner et al. 2009). The radio free-free emission also originates from a medium like this. The lack of correlation, or putative anti-correlation, may therefore be explained by the very different volume-filling factors.

2.4.4 Ionisation losses

The spectral curvature and the $H \text{ I}$ gas-mass surface density (Fig. 2.12) are related, however. We therefore explored ionisation losses as an alternative mechanism to explain the low-frequency flattening because it dominates in the neutral gas. Cosmic-ray electrons lose energy due to the ionisation of atomic and molecular hydrogen. The ionisation loss rate is directly proportional to the number density of neutral atoms and molecules n , as shown in the following expression in the case of neutral hydrogen (Longair 2011):

$$-\left(\frac{dE}{dt}\right)_{\text{ion}} = 7.64 \times 10^{-15} n (3 \ln \gamma + 19.8) \text{ eV s}^{-1}, \quad (2.15)$$

where E is the electron energy, and γ is the Lorentz factor. The dependence on energy is only logarithmic, and so it can be approximated as constant throughout the spectrum. At lower energies, a larger energy fraction is lost due to ionisation, and therefore the effect is stronger. The fraction of energy that is lost is higher at lower CR energies because the total energy is lower while the lost energy is approximately constant. This means that the cosmic-ray electron number density (per energy bin) does decrease as function of time, and this effect is more pronounced at lower energies. The spectral index flattening due to ionisation losses should be $\Delta\alpha \leq 0.5$ in comparison to the injection spectrum (Basu et al. 2015).

2 A spatially resolved radio spectral study of the galaxy M51

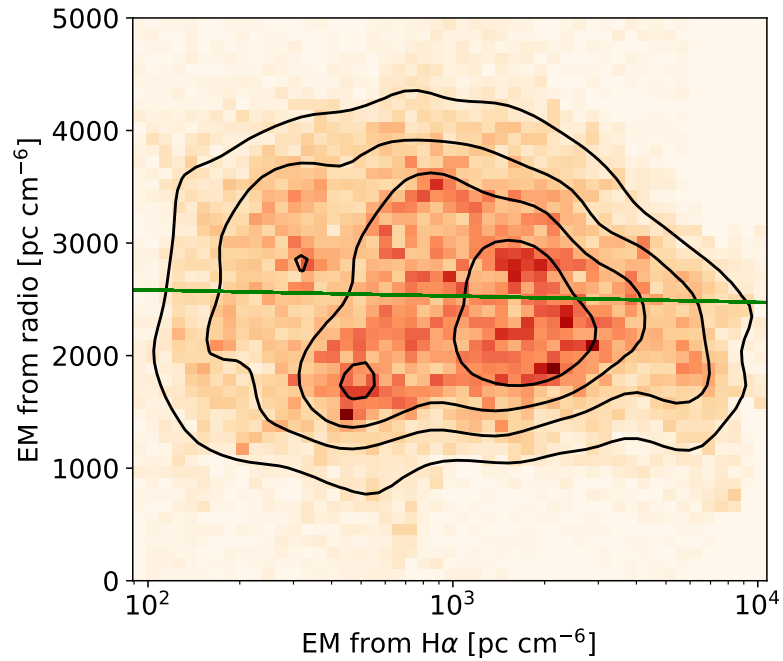


Figure 2.11: Comparison of the EM from H α flux density to the EM obtained by fitting the free-free absorption model to the radio data. The colours and contours represent the data point density. The green line shows the best-fitting, if insignificant, correlation.

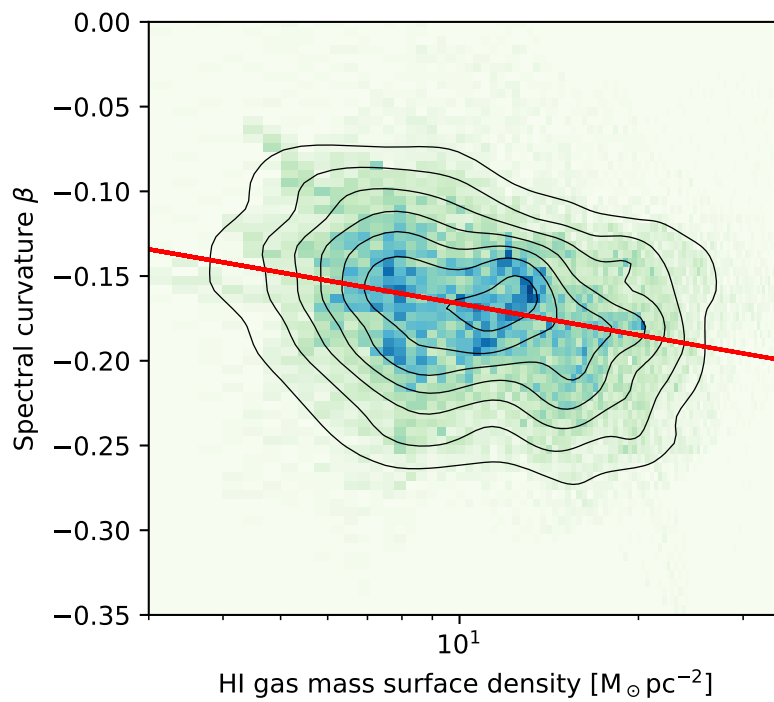


Figure 2.12: Non-thermal radio spectral curvature as a function of the H I gas-mass surface density. The colours and contours show the data point density. The red line shows the best-fitting correlation.

In Fig. 2.12 we show the non-thermal spectral curvature as a function of H I gas-mass surface density. We find a weak negative correlation ($\rho_s = -0.21$). This can be explained if cosmic-ray ionisation losses cause the low-frequency flattening. At higher H I gas-mass surface densities, the spectrum becomes more concave (lower value of β), as expected if ionisation losses play a role. The timescale for ionisation losses is (Murphy 2009)

$$t_{\text{ion}} = 4.1 \times 10^9 \left(\frac{n}{\text{cm}^{-3}} \right)^{-1} \left(\frac{E}{\text{GeV}} \right) \left[3 \ln \left(\frac{E}{\text{GeV}} \right) + 42.5 \right]^{-1} \text{ yr.} \quad (2.16)$$

For this timescale to be an important process to flatten the radio continuum spectrum at low frequencies, it therefore has to be shorter than the synchrotron loss timescale of approximately 100 Myr (Heesen et al. 2023). For cosmic-ray electrons with $E \approx 0.5$ GeV at the lowest frequency, we thus expect $t_{\text{ion}} \approx 100$ Myr for neutral gas densities of $n \approx 0.5 \text{ cm}^3$. This is the case for mass surface densities of $\Sigma_{\text{gas}} = 2.5\text{--}5 M_{\odot} \text{ pc}^{-2}$, assuming a gas scale height of 100 pc (Cox 2005; Basu et al. 2015). This means that the suggested correlation between non-thermal spectral curvature and H I gas-mass surface density can indeed be ascribed to cosmic-ray ionisation losses that affect the low-energy cosmic-ray electrons most. In the absence of a spectral model for ionisation losses, we leave a more rigorous fitting of the spectra to future work. We currently cannot rule out the effect free–free absorption in addition to ionisation losses. We therefore conclude that the low-frequency flattening observed in M 51 is probably caused by a combination of ionisation losses and free–free absorption.

Ionisation of the molecular component of the interstellar medium should also cause CR energy loss. We repeated the same analysis as shown in Fig. 2.12 to test the correlation between the spectral curvature and the total gas-mass density. In contrast to our expectation, they are not correlated ($\rho_s = -0.07$). The reason may be that cosmic rays (at least in the GeV range) do not enter molecular clouds because the magnetic field is strong and turbulent (Tabatabaei et al. 2013).

2.5 Summary and conclusions

Synchrotron spectra at low radio frequencies are shaped by several processes, such as cosmic-ray ionisation losses and free–free absorption, that suppress the emission. The cosmic-ray energy loss from ionisation is nearly independent of energy (the dependence is only logarithmic), and it therefore proportionally affects low-energy cosmic-ray electrons most, resulting in spectral flattening. Free–free absorption is also strongly dependent on frequency. Frequencies below 300 MHz (depending on EM) are more affected. This affects our ability to interpret low-frequency continuum emission as an extinction-free star formation tracer. On the other hand, strong free–free absorption would allow us to measure the EM, which itself is derived from radio spectra and thus is an extinction-free star-formation tracer. In order to study these effects, we compiled data of the nearby grand-design spiral galaxy M 51 at nine different frequency bands between 54 and 8350 MHz, eight of which we used for the analysis. We presented for the first time new observation with the GMRT at 240 MHz. We calculated the contribution of the thermal radio continuum emission based on the H α map corrected for extinction using 24 μm mid-infrared data. This contribution was subtracted from the radio maps, so that we only studied the non-thermal emission. We also used new IFU spectroscopy data from Metal-THINGS in order to measure extinction-corrected H α intensities, which we used as an independent EM estimate.

First, we fitted a polynomial function to the logarithmic intensities to determine the non-thermal radio spectral index and spectral curvature, as shown in Fig. 2.6. The non-thermal radio spectral index at 1 GHz is relatively flat in the spiral arms, with $\alpha_0 \approx -0.6$, in agreement with the injection

spectral index. The spectral curvature is negative throughout the galaxy, with more negative values in the spiral arms. This means that the spectrum is concave, where intensities both at low and high frequencies are suppressed. This is the expected behaviour for low-energy losses and absorption effects as well as strong synchrotron and inverse-Compton radiation losses at higher frequencies, resulting in spectral ageing. Next, we calculated the low- (54–144 MHz) and high-frequency (1370–4850 MHz) non-thermal two-point radio spectral indices separately, as shown in Fig. 2.8. The low-frequency radio spectral index is very flat and even positive in the spiral arms, with α_{low} between -0.5 and 0.2 , showing inverted radio continuum spectra. This clearly hints at either low frequency absorption or cosmic-ray ionisation losses. In contrast, the high-frequency radio spectra are fairly steep, with values of α_{high} between -1.5 and -0.7 . The differences throughout the galaxy can be explained by spectral ageing.

Next, we analysed the spatially resolved spectral index in more detail, starting with the effect of free–free absorption. In Fig. 2.9 we plot the integrated spectra of the spiral arms, inter-arm, and core regions. The spectra can be well fitted with a free–free absorption model (Wills et al. 1997). At 54 MHz the deviation from a power-law spectrum is most apparent.

Comparing the spiral arms with the inter-arm regions, we find that the turnover in the spiral arms occurs at higher frequencies, which implies stronger free–free absorption. This is confirmed by the values of the EM obtained by fitting the free–free absorption model. On the other hand, the difference in the EM between spiral arm and inter-arm regions is not statistically significant, suggesting that free–free absorption might not be the only effect.

We then fitted the free–free absorption model to our spatially resolved data. We obtained point-by-point maps of the EM and the radio spectral index η (Fig. 2.10). We compared the EM values obtained from the fit to the values estimated from the extinction-corrected H α measurements. The EMs calculated from different tracers are not correlated (Fig. 2.11). The lack of correlation may therefore be explained by the very different volume-filling factors, or the free–free absorption might not be the only process that causes the low-frequency flattening. Therefore, we also investigated the possible influence of cosmic-ray ionisation losses on the radio continuum spectrum. To this end, we studied the correlation between non-thermal spectral curvature and gas-mass surface density. We find a weak correlation between spectral curvature and H I gas-mass surface density (Fig. 2.12). The main process that causes the low-frequency flattening is therefore probably more dominant in the regions with neutral H I gas. In these regions, the cosmic rays lose energy due to ionisation. Because ionisation losses are nearly independent of frequency, they are more apparent at low frequencies, where low-energy cosmic-ray electrons emit. We therefore conclude that the low-frequency flattening in M51 is most likely caused by a combination of free–free absorption and ionisation losses.

A low-frequency spectral flattening in an average spiral galaxy outside of the Milky Way is observed here for the first time. Previously, this effect was only observed in starburst galaxies (Adebahr et al. 2013; Basu et al. 2015; Varenius et al. 2016; Adebahr et al. 2017). Now we were able to spatially locate the galaxy region in which the spectra flattens at low frequencies. These areas generally have a higher density of H I gas. Curiously, spectral curvature and total gas-mass density are not correlated, suggesting that the cosmic-ray ionisation losses occur in the atomic gas phase, but not in the molecular gas phase, possibly because the cosmic rays do not enter molecular clouds due to the magnetic field (Tabatabaei et al. 2013). We also considered what our results mean for using sub-GHz radio continuum observations as an SFR tracer. Even when low frequencies of around 150 MHz (LOFAR HBA) are used as an SFR tracer, an understanding of the losses we investigated here is required (see e.g. Adebahr et al. 2013; Chyży et al. 2018). The forthcoming surveys with LOFAR at very low frequencies and high angular resolution will enable further studies in other nearby galaxies and allow us to investigate the influence of these effects in more detail.

Acknowledgements

We thank the two anonymous referees for detailed comments which significantly improved the paper and especially made it more understandable for the reader. LG and MB acknowledge funding by the Deutsche Forschungsgemeinschaft (DFG, German Research Foundation) under Germany's Excellence Strategy – EXC 2121 “Quantum Universe” – 390833306. BA, DJB and MS acknowledge funding from the German Science Foundation DFG, via the Collaborative Research Center SFB1491 ‘Cosmic Interacting Matters – From Source to Signal’. FdG acknowledges support from the ERC Consolidator Grant ULU 101086378. LOFAR (van Haarlem et al. 2013) is the Low Frequency Array designed and constructed by ASTRON. It has observing, data processing, and data storage facilities in several countries, which are owned by various parties (each with their own funding sources), and that are collectively operated by the ILT foundation under a joint scientific policy. The ILT resources have benefited from the following recent major funding sources: CNRS-INSU, Observatoire de Paris and Université d’Orléans, France; BMBF, MIWF-NRW, MPG, Germany; Science Foundation Ireland (SFI), Department of Business, Enterprise and Innovation (DBEI), Ireland; NWO, The Netherlands; The Science and Technology Facilities Council, UK; Ministry of Science and Higher Education, Poland; The Istituto Nazionale di Astrofisica (INAF), Italy. This research made use of the Dutch national e-infrastructure with support of the SURF Cooperative (e-infra 180169) and the LOFAR e-infra group. The Jülich LOFAR Long Term Archive and the German LOFAR network are both coordinated and operated by the Jülich Supercomputing Centre (JSC), and computing resources on the supercomputer JUWELS at JSC were provided by the Gauss Centre for Supercomputing e.V. (grant CHTB00) through the John von Neumann Institute for Computing (NIC). This research made use of the University of Hertfordshire high-performance computing facility and the LOFAR-UK computing facility located at the University of Hertfordshire and supported by STFC [ST/P000096/1], and of the Italian LOFAR IT computing infrastructure supported and operated by INAF, and by the Physics Department of Turin university (under an agreement with Consorzio Interuniversitario per la Fisica Spaziale) at the C3S Supercomputing Centre, Italy. The research leading to these results has received funding from the European Research Council under the European Union’s Seventh Framework Programme (FP/2007-2013) / ERC Advanced Grant RADIOLIFE-320745. The Westerbork Synthesis Radio Telescope is operated by ASTRON (Netherlands Foundation for Research in Astronomy) with support from the Netherlands Foundation for Scientific Research (NWO). This research made use of the Python Kapteyn Package (Terlouw & Vogelaar 2015).

2 A spatially resolved radio spectral study of the galaxy M51

3 The low-frequency flattening of the radio spectrum of giant H II regions in M 101

L. Gajović, V. Heesen, M. Brüggen, H. W. Edler, B. Adebahr, T. Pasini, F. de Gasperin, A. Basu, M. Weżgowiec, C. Horellou, D. J. Bomans, H. Dénes, D. Vohl, *Accepted to Astronomy & Astrophysics*, arXiv:2502.08713. (2025)

Abstract

Context. In galaxies, the flattening of the spectrum at low radio frequencies below 300 MHz has been the subject of some debate. A turnover at low frequencies could be caused by multiple physical processes, which can yield new insights into the properties of the ionised gas in the interstellar medium.

Aims. We investigate the existence and nature of the low-frequency turnover in the H II regions of M 101.

Methods. We study the nearby galaxy M 101 using the LOw Frequency ARray (LOFAR) at frequencies of 54 and 144 MHz, Apertif at 1370 MHz, and published combined map from the Very Large Array (VLA) and Effelsberg telescope at 4850 MHz.

Results. The spectral index between 54 and 144 MHz is inverted at the centres of H II regions. We find a significant low-frequency flattening at the centres of five out of six H II regions that we selected for this study.

Conclusions. The low frequency flattening in H II regions of M 101 can be explained with two different free-free absorption models. The flattening is localised in a region smaller than 1.5 kpc and can only be detected with high resolution (better than 45"). The detection of low frequency flattening has important consequences for using radio continuum observations below 100 MHz to measure extinction-free star-formation rates.

3.1 Introduction

Non-thermal (synchrotron) and thermal (free-free) radiation processes play a key role in the radio continuum emission of nearby galaxies. Synchrotron radiation in galaxies is produced by cosmic-ray (CR) electrons that spiral around magnetic field lines and free-free radiation by free electrons scattering off ions (e.g. Niklas et al. 1997; Basu et al. 2012; Tabatabaei et al. 2017). The synchrotron radiation dominates the spectrum at radio frequencies below a few GHz. CRs that produce synchrotron radiation originate from regions with higher star formation in spiral galaxies because they are accelerated through shocks during supernova explosions (Green 2014; Caprioli et al. 2010). The

3 The low-frequency flattening of the radio spectrum of giant H II regions in M 101

spectrum of synchrotron radiation is a power law $S_\nu \propto \nu^\alpha$, with a radio spectral index α between -1.2 and -0.5 for nearby galaxies (e.g. Gioia et al. 1982; Li et al. 2016; Tabatabaei et al. 2017). At higher frequencies (around 10 GHz), the contribution of thermal free-free emission from ionised gas with the spectral index $\alpha = -0.1$ becomes significant and the spectrum should flatten out (e.g. Tabatabaei et al. 2017; Klein et al. 2018). Lower-frequency (below 100 MHz) observations at high spatial resolution only recently became possible with the advent of digital interferometers, such as the LOw Frequency ARray (LOFAR; van Haarlem et al. 2013), and sophisticated calibration strategies (van Weeren et al. 2016; Tasse et al. 2018; de Gasperin et al. 2019). Still, the spectral behaviour in this frequency regime remains largely unexplored, but there is evidence that the spectrum of nearby galaxies flattens or even turns over below 100 MHz.

The low frequency flattening was first noticed in statistical studies of galaxy samples. Israel & Mahoney (1990) observed that the radio intensities at 57.5 MHz are systematically lower than the values extrapolated from higher frequency measurements assuming a power law spectrum. They reported a dependence of the flattening on the inclination of the galaxies and attributed it to free-free absorption. However, Hummel (1991) was unable to find any correlation using the same data and stressed that a steepening of the spectrum at high frequencies due to propagation effects of the relativistic electrons is equally plausible. A more recent study by Chyży et al. (2018), using additional data at 150 MHz, confirms the results of Hummel (1991).

An alternative explanation for the low frequency flattening was provided by Pohl & Schlickeiser (1990) and Pohl et al. (1991a,b) who modelled the energy spectra of CR electrons that experience simultaneous injection, diffusion, convection, adiabatic deceleration, as well as radiative and ionisation losses. Observing a large sample of 250 bright galaxies at three pairs of frequencies with the lowest being 74 and 325 MHz, Marvil et al. (2015) reports a curvature in the mean spectrum with a magnitude of approximately $\Delta\alpha = -0.2$ per logarithmic frequency decade. They propose two reasons for this effect: free-free absorption at low frequencies or a curved synchrotron spectrum resulting from curvature in the underlying energy distribution of CR electrons.

To observe the low-frequency spectral flattening in individual galaxies it is usually necessary to look at exceptional targets where the flattening is significant at comparatively high frequencies. In the centre of the Milky Way, thermal absorption shapes the spectra below 500 MHz (Roy & Pramesh Rao 2006). Meanwhile, the integrated spectrum of the Milky Way has a detectable turnover at about 3 MHz (Brown 1973). In the starburst galaxy M 82, turnovers were detected in the global integrated radio spectrum (Klein et al. 1988), the core regions (Adebahr et al. 2013), and individual sources near the galactic centre (Adebahr et al. 2017). There is also a low frequency turnover in the integrated spectrum of the starburst galaxy NGC 253 (Marvil et al. 2015). The ultra-luminous infrared galaxy Arp 220 shows a turnover in the central region at around 1 GHz (Varenius et al. 2016) and in the integrated spectrum (Anantharamaiah et al. 2000).

More recently, Ramírez-Olivencia et al. (2022) investigate the luminous infrared galaxy Arp 299 using sub-arcsecond LOFAR observations at 150 MHz. In order to fit the SED in the nucleus of this galaxy, they use two models for the free-free absorbing and emitting thermal gas. In the first model the gas is smooth and continuous medium while in the second model it is distributed in a clumpy fashion (Lacki 2014; Conway et al. 2018). They find that both models fit their data reasonably well. While the smooth continuous model can explain the SED by an injection of relativistic electrons subjected to synchrotron, bremsstrahlung, and ionisation losses, the clumpy model yields negligible losses but a more realistic thermal fractions.

In the dwarf galaxy IC 10, spectra of several compact H II-regions were measured down to 320 MHz (Basu et al. 2017). These spectra show evidence of thermal free-free absorption at low frequencies. A region of the edge-on galaxy NGC 4631 observed by Stein et al. (2023) is found to

Table 3.1: Basic properties of M 101.

Name	M 101
Alternative names	NGC 5457
RA (J2000)	14 ^h 03 ^m 12 ^s .5
DEC (J2000)	+54°20′ 56″
Morphology	SAB(rs)cd ^a
Apparent size	40′ ^b
Distance	6.644 ± 0.087 Mpc ^c
Position angle	36° ^d
Inclination angle	26° ^d
Scaling	1″ ↔ 32.21 pc

References. ^(a)de Vaucouleurs et al. (1991), ^(b)Vorontsov-Vel’ Yaminov & Arkhipova (1962), ^(c)Hiramatsu et al. (2023), ^(d)Hu et al. (2018)

have a very flat radio spectrum with a flattening at low-frequencies. Local spectral turnovers are also observed in jellyfish galaxies, where they might be due to ionisation losses in compressed gas (Lal et al. 2022; Ignesti et al. 2022; Roberts et al. 2024). The only average spiral galaxy where the low frequency effects were studied in detail is M 51 (Gajović et al. 2024). Using high-resolution low-frequency radio maps, they show that the flattening spatially correlates with the neutral H I gas in the galaxy which points to CR ionisation losses as an important mechanism aside from free-free absorption.

In summary, there is still no consensus about what causes the low-frequency flattening at radio frequencies below 300 MHz and whether there is a turnover. The most commonly suggested explanation for the flattening is free-free absorption. However, ionisation losses, CR ageing, or synchrotron-self absorption could also be responsible. The physical mechanism most likely depends on the galaxy’s environment and is possibly a combination of multiple effects. We therefore choose to explore the low frequency spectrum of the nearby spiral galaxy M 101 that is known to have multiple giant H II regions in a diffuse disc. While the previous study of M 51 surprisingly shows no correlation with ionised gas (Gajović et al. 2024), this may be because the H II regions are embedded in strong background radiation and thus are hard to study individually. Therefore, we focus on the giant H II regions in M 101 that are very massive and luminous, so they can be studied in the radio continuum (Israel et al. 1975).

The galaxy M 101 (details in Table 3.1) and its H II regions have already been studied at radio frequencies down to 610 MHz (Israel et al. 1975; Graeve et al. 1990; Berkhuijsen et al. 2016). It is possible to observe M 101 at a high spatial resolution because of its large angular diameter of 40′ and a distance of only 6.6 Mpc. Israel et al. (1975) mapped M 101 at 610 MHz with 1′ resolution, and specifically noted the brightest H II regions and how the structure visible in radio compares to two different H α maps. Graeve et al. (1990) studied the H II region spectra and found them to be flat due to thermal emission. However, they did not observe a turnover because their measurements did not extend to frequencies below 610 MHz. In this work, we use LOFAR to observe M 101 at frequencies of 54 and 144 MHz with a resolution higher than 26″ and search for the low frequency flattening in the H II regions.

This paper is structured as follows: in Sect. 3.2 we present the data from LOFAR, Apertif and literature. Sect. 3.3 describes the data preparation, including the selection of the H II regions. In Sect. 3.4 we present our results that are discussed in Sect. 3.5. Finally, we conclude in Sect. 3.6.

3 The low-frequency flattening of the radio spectrum of giant H II regions in M 101

Table 3.2: Observation parameters for the radio maps used in the analysis.

Telescope (Survey)	Central frequency [MHz]	Beam size	Beam position angle PA [°]	Original σ rms noise [$\mu\text{Jy beam}^{-1}$]	Convolved regridded σ_c rms noise [$\mu\text{Jy beam}^{-1}$]	Flux density scale un- certainty ϵ_v [%]	Ref.
LOFAR (LoLSS)	54	26''5 \times 14''7	114.8	1700	1700	10	1
LOFAR (LoTSS)	144	20''0 \times 20''0	/	130	170	10	2
Apertif	1370	15''1 \times 11''0	1.4	20	30	5	3
VLA+Effelsberg	4850	30''0 \times 30''0	/	59	59	5	4

References: (1) Observed by de Gasperin et al. (2021), reprocessed in this paper; (2) Shimwell et al. (2022); (3) This work; (4) Weżgowiec et al. (2022).

3.2 Data

We used four radio maps at frequencies of 54, 144, 1370 and 4850 MHz at resolutions between 11'' and 30''. The details of each map are presented in Table 3.2 and in the following sections.

3.2.1 LOFAR LBA observations

M 101 was observed with the LOFAR Low-Band Antenna (LBA) system at a central frequency of 54 MHz and in a bandwidth of 24 MHz as part of the LOFAR LBA Sky Survey (LoLSS; de Gasperin et al. 2021, 2023). The galaxy is covered by three survey pointings (P209+55, P210+52, P214+55) with a primary beam response of at least 30% and each pointing was observed for 8 h. The observations were calibrated for direction-independent (de Gasperin et al. 2021) and direction-dependent effects (de Gasperin et al. 2023). To further process the pointings, for each observation we subtracted all sources except for a circular region with 0.25° radius around M 101 from the visibility data using the source models and calibration solutions found in the direction-dependent calibration carried out as part of LoLSS. We then phase-shifted the measurement sets of the individual observations and pointings to the location of M 101 and corrected them for the primary beam response in the new phase centre. We also applied the direction-dependent calibration solutions of the nearest direction-dependent calibrator source from LoLSS (for more details about the calibration procedure see e.g. Pasini et al. 2022). All nine observations were then imaged together to allow for a deep deconvolution of the extended emission associated with M 101. The LOFAR LBA radio map of M 101 at 54 MHz is presented in Fig. 3.1 and the main parameters of the map are in Table 3.2.

3.2.2 Apertif observations

The Apertif system is a Phased Array Feed (PAF) receiver operating at a central frequency of 1.4 GHz with a bandwidth of 300 MHz mounted on the dishes of the Westerbork Synthesis Radio Telescope (WSRT). The PAF allows simultaneous observations of 40 individual compound beams covering an area of 6.6 deg^2 .

We inspected the Apertif Wide and Medium Deep Extragalactic Survey (AWES/AMES; Adams

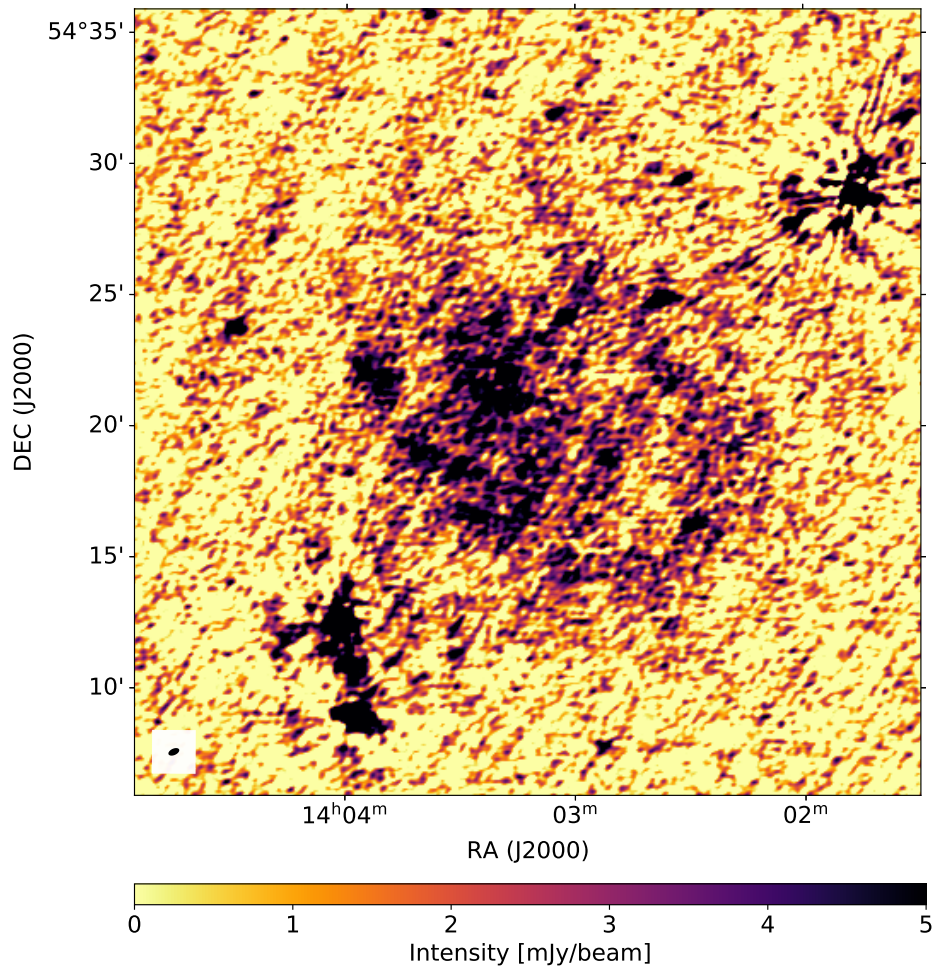


Figure 3.1: Radio map of M 101 at 54 MHz observed with LOFAR LBA. The beam size is shown with the black ellipse in the bottom left corner.

et al. 2020) observations and the Apertif archive for coverage of M 101. Fortunately, the galaxy is situated very close to the intrahour-variable source J1402+5347 (Oosterloo et al. 2020) that was observed twelve times during the Apertif operational phase. We considered a compound beam response level of 10 % as useful for imaging. This resulted in three compound beams (numbers 29, 35 and 36) of each observation being considered for further inspection.

For the data reduction, we used the cross-calibrated visibilities provided by the `apercal`-pipeline averaged down to 192 channels for every compound beam data set. These data were then directionally dependent self-calibrated and finally imaged in total power using the advanced Apertif reduction pipeline (Kutkin et al. 2023).

We found that eight out of the twelve observations had sufficient data quality in terms of dynamic range and resolution to be usable for our analysis. The corresponding observation ids are 190807041, 190913045, 191010041, 191102001, 191207034, 200106009, 200128124 and 200302074. The final image was generated by convolving all 24 images (one per beam and observation) to the largest common synthesised beam and correcting by their appropriate primary beam model (Dénes et al. 2022). The final Apertif radio map at 1370 MHz is presented in Fig. 3.2 and the main parameters of the map are in Table 3.2.

3 The low-frequency flattening of the radio spectrum of giant H II regions in M 101

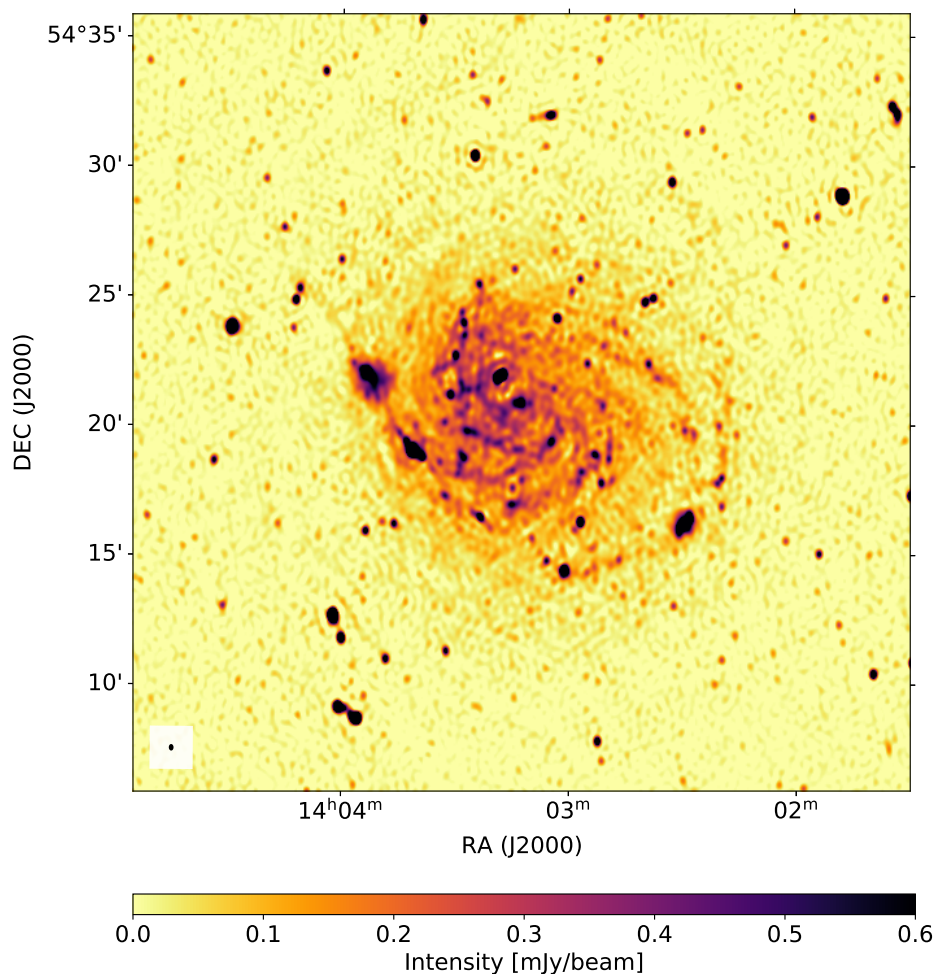


Figure 3.2: Radio map of M 101 at 1370 MHz observed with Apertif. The beam size is shown with the black ellipse in the bottom left corner.

3.2.3 Other radio continuum data

The observation of M 101 at 144 MHz was done with the LOFAR high-band antennas (HBA) as a part of the LOFAR Two-metre Sky Survey data release 2 (LoTSS-DR2; Shimwell et al. 2022). The map of M 101 used in this work was reprocessed by Heesen et al. (2022) along with 44 other nearby galaxies. They compared the low 20'' and the high 6'' resolution maps and made sure that the integrated flux density matches. We used the low resolution map because it is more sensitive to diffuse emission and the maps at other frequencies have similar beam sizes, so this map did not have to be convolved to a significantly larger beam. We also consulted the high resolution map to identify background sources. The flux density scale error of LoTSS-DR2 is below 10% (Shimwell et al. 2022), which is the value we adopted. The main parameters of the LOFAR HBA radio map are presented in Table 3.2.

The radio map of M 101 at 4850 MHz is a combination of VLA and Effelsberg maps presented by Weżgowiec et al. (2022). Because of the large angular size of M 101, the VLA observations include multiple pointings separated in two observation projects (19B-027 and 15B-292). The results of Effelsberg observations were previously published by Berkhuijsen et al. (2016). The combination of the two data sets restores the large-scale diffuse emission that cannot be recovered if the short

baselines are not sufficiently covered by the interferometer. More details on the VLA calibration and the combination of data sets are presented in Weżgowiec et al. (2022). In this work, we used only the total intensity map and assumed a flux density scale uncertainty of 5%, which is standard for the VLA (Konar et al. 2013). The main parameters of the combined VLA and Effelsberg radio map are presented in Table 3.2.

3.3 Data preparation

The radio maps were additionally processed in the following way. All data, except for the 4850 MHz, were convolved to the largest common beam of $26.52'' \times 20''$ with the position angle $PA=115^\circ$. For the convolution, we used the routine CONVOL of the software package MIRIAD (Sault et al. 1995). The 4850 MHz data were kept with the original $30''$ beam and for flux density measurements we made sure to take into account the different beam size for that map. We did not convolve to the largest common beam of all data (which would be $30''$) because that would make the large rms noise in the LBA map even worse. The rms error dominates over the flux scale error in small regions that we study, so it was important to keep it as small as possible.

All maps were then aligned to a common world coordinate system, re-gridded to a pixel size of $2''$, as well as transformed into the reference pixel and image size. We used the world coordinate system of the $H\alpha$ map by Hoopes et al. (2001) as the reference. This was achieved using the REGRID routine of MIRIAD.

The rms noise σ of each individual image was determined by calculating the standard deviation over an emission-free area. The total noise was calculated as a combination of the rms noise and the flux density scale uncertainty (both listed in Table 3.2).

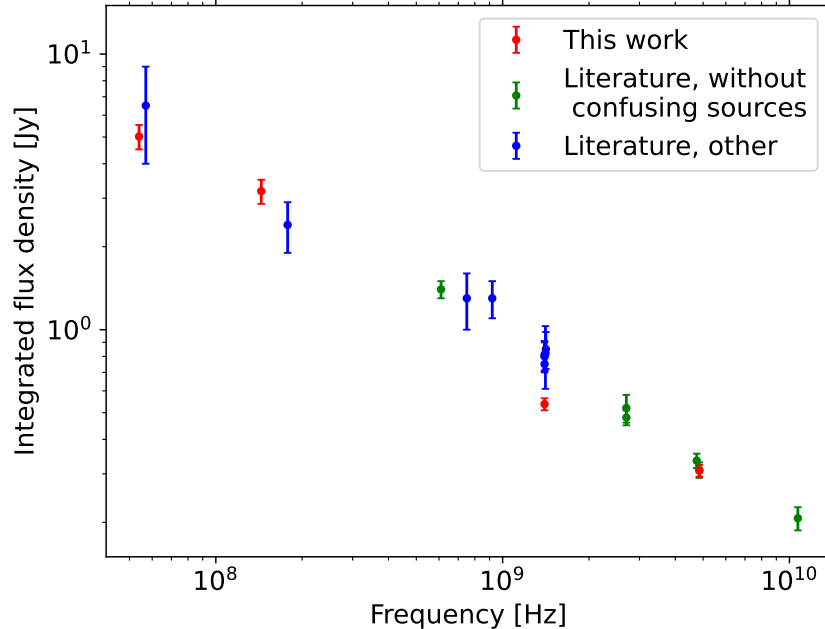


Figure 3.3: Integrated spectrum of M 101. The flux density measurements from the maps used in this work (red) compared to literature flux density measurement, separated into those where bright background sources surrounding the galaxy are excluded (green) and are not excluded (blue).

3.3.1 Data validation

We first checked if the integrated flux density of M 101 in our maps matches the literature measurements. We prepared a mask to calculate the integrated flux density in our maps, which includes all the emission from the galaxy, but excludes nearby bright radio sources (e.g. NVSS J140147+542852 and NVSS J140357+540852). We specifically made sure we include the H II region NGC 5471, which is located outside the galactic disc to the east. We did not remove the background sources in cases where their emission overlapped with the disc of the galaxy (e.g. NVSS J140318+542159). The mask is shown in Appendix C.

We compile the integrated flux density of M 101 from the literature and from the maps used in this paper in Appendix D. We also note the type of telescope used for the observation, the beam size and most importantly whether the bright background sources around the galaxy are included in the flux density measurements. We show these measurements in Fig. 3.3. The data points roughly follow a power-law. We do not see a significant flattening of the integrated spectrum at low frequencies. Comparing our data with the literature, we notice that there might be missing large-scale flux density in the 1370 MHz Apertif map. The inclusion of background sources cannot account for this difference. For this reason, the Apertif map was not used for studying the galaxy as a whole, only the compact

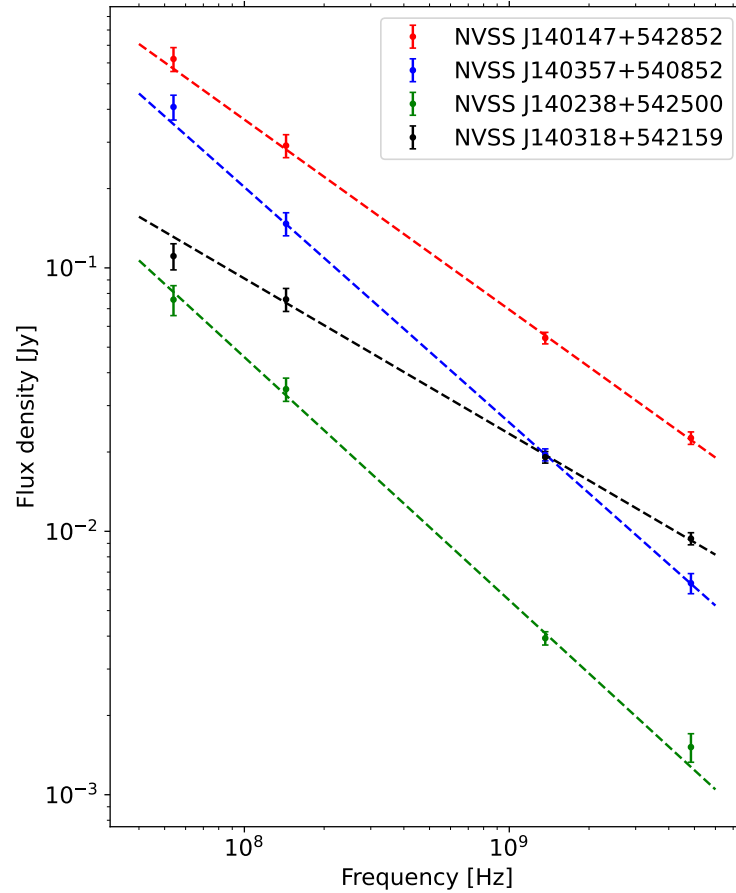


Figure 3.4: Spectra of four selected background sources. The spectra follows a power law as expected confirming that there are no flux density problems in our images at small scales.

H II regions that are less likely to be affected by missing flux density issue.

We additionally checked if our maps are reliable to study spectra in smaller regions. In Fig. 3.4, we plot the spectra of four background radio sources surrounding M 101. The spectra are well-fit by a power-law between 54 MHz and 5GHz, and the offset of the data points is minimal. Because the small scale flux is reliable, we can continue with analysing the spectra of H II regions in M 101. We used the Apertif map for studying the spectra of smaller regions that are not affected by the missing large-scale flux density.

3.3.2 H II region selection

More than a thousand H II regions were identified in M 101 (Hodge et al. 1990), but we want to focus on the prominent giant H II regions. There is no consensus in literature on what constitutes a giant H II region, but they generally have a large physical size and they are very bright at both optical and radio frequencies. Therefore, we combine the most comprehensive lists of giant H II regions in M 101 (Skillman & Israel 1988; Hippelein 1986; Dodorico et al. 1983) with coordinate positions (Gordon et al. 2008) in Table 3.3.

For this paper, we selected the H II regions that are prominent at low radio frequencies, specifically in the 144 MHz map. We chose the 144 MHz map because the frequency is high enough to not be affected by low frequency flattening. Additionally, the 144 MHz map has a good signal-to-noise ratio.

Table 3.3: Coordinates of H II regions considered for analysis. Regions 0-5 were selected.

No.	Name	RA(J2000)	DEC(J2000)	Ref.
0	Centre	14:03:12.48	+54:20:55.4	1
1	NGC 5447	14:02:28.18	+54:16:26.3	1,2,3,4
2	NGC 5455	14:03:01.13	+54:14:28.7	1,2,3,4
3	NGC 5461	14:03:41.36	+54:19:04.9	1,2,3,4
4	NGC 5462	14:03:53.19	+54:22:06.3	1,2,4
5	NGC 5471	14:04:29.35	+54:23:46.4	1,2,3,4
6	NGC 5449	14:02:26.0	+54:19:48.0	2,5
7	Hodge 1013 ^{a,b}	14:03:31.0	+54:21:14.5	1,2,4,6
8	Searle 5	14:02:55.05	+54:22:26.6	1,2
9	Searle 12	14:04:11.11	+54:25:17.8	1,2,4
10	Hodge 67 ^a	14:02:19.92	+54:19:56.4	1
11	Hodge 70/71 ^a	14:02:20.50	+54:17:46.0	1
12	Hodge 681 ^a	14:03:13.64	+54:35:43.0	1

References: ((1) Gordon et al. (2008); (2) Hippelein (1986); (3) Skillman & Israel (1988); (4) Dodorico et al. (1983); (5) Corwin (1995); (6) Hodge et al. (1990).

^(a) Identification numbers according to Hodge et al. (1990). ^(b) Also called Hodge 40, according to Hodge (1969).

3 The low-frequency flattening of the radio spectrum of giant H II regions in M 101

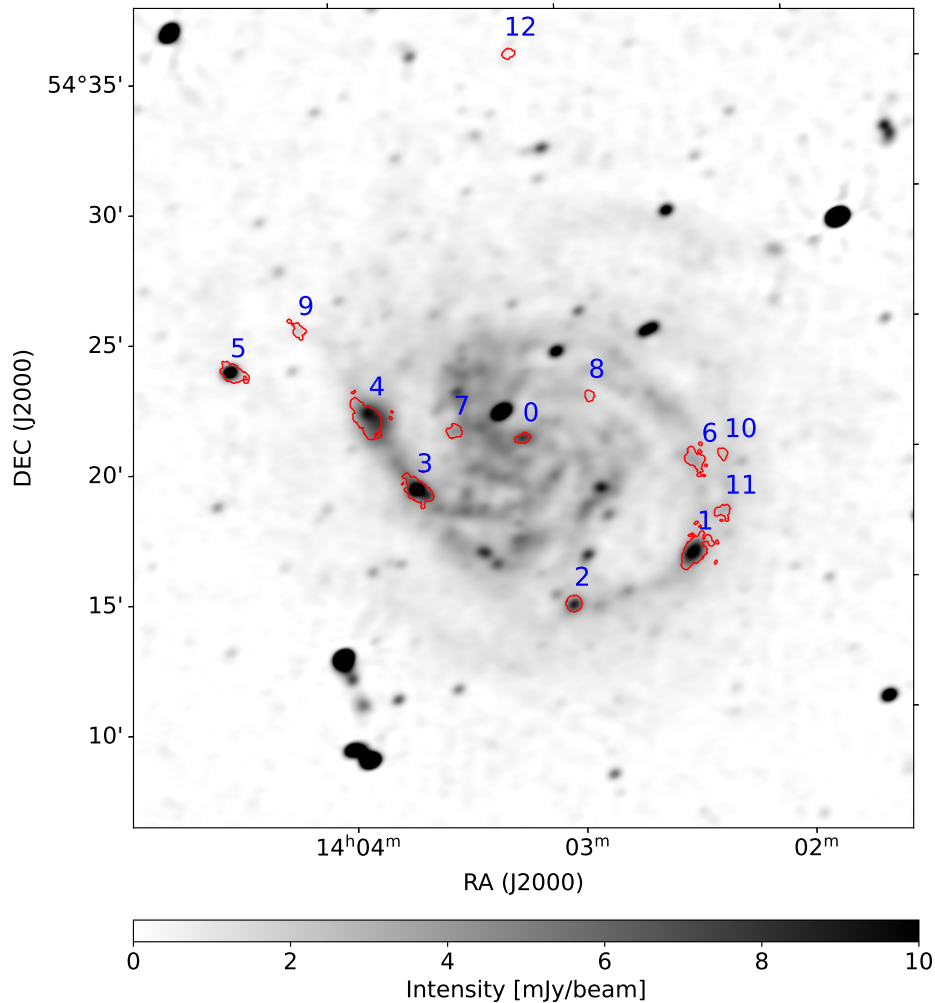


Figure 3.5: H II region boundaries determined from H α (Hoopes et al. 2001) plotted on top of 144 MHz radio map. The region boundaries are red and the blue numbers correspond to their identification numbers in Table 3.3. For the analysis we select only regions 0-5, which are bright at 144 MHz. Note that these boundaries were only used in the H II region selection.

In this selection, we used the H α map by Hoopes et al. (2001) to define the H II region boundaries. First, we manually plotted circles that include all the H α emission from the H II region and mostly exclude the surrounding emission. Second, we refined the H II region boundary by selecting everything above 10σ in the H α image. In Fig. 3.5, the H II region boundaries defined from H α are plotted on top of the 144 MHz map. Regions 0–5 show a clear excess of emission compared to the disc surrounding them. For regions 0–5, surface brightness is higher than 7 mJy/beam while for the other regions it is lower than 5 mJy/beam. We chose these six regions (the galactic centre, NGC 5447, NGC 5455, NGC 5461, NGC 5462, and NGC 5471) for the spectral analysis in this work. Coincidentally, those are the same regions selected for analysis by Israel et al. (1975), likely because of their brightness at radio frequencies.

3.4 Results

3.4.1 Spectral index maps between 54 and 144 MHz

We calculated the radio spectral index of M 101 between 54 and 144 MHz. Both radio maps were convolved to the same beam ($26.52'' \times 20''$ beam with $PA=115^\circ$) and re-gridded to the same coordinate grid. The spectral indices were calculated in a standard way by taking the logarithmic ratio of the flux densities in two maps over the logarithmic frequency ratio. The errors in the spectral index maps were calculated by propagating the errors from the individual maps, which are a combination of the flux density scale uncertainty and the rms noise measured away from the source (both listed in Table 3.2). The regions below 2σ (in either map) were excluded from the analysis. We chose a 2σ exclusion limit instead of the usually used 3σ because otherwise the high noise in the LBA map would significantly limit the area in which the spectral index is calculated. We also note that LOFAR has good coverage of short baselines which correspond to large angular scales on the sky. We can therefore trust that the LOFAR maps are not missing large scale emission from M 101 and the spectral indices presented here are reliable.

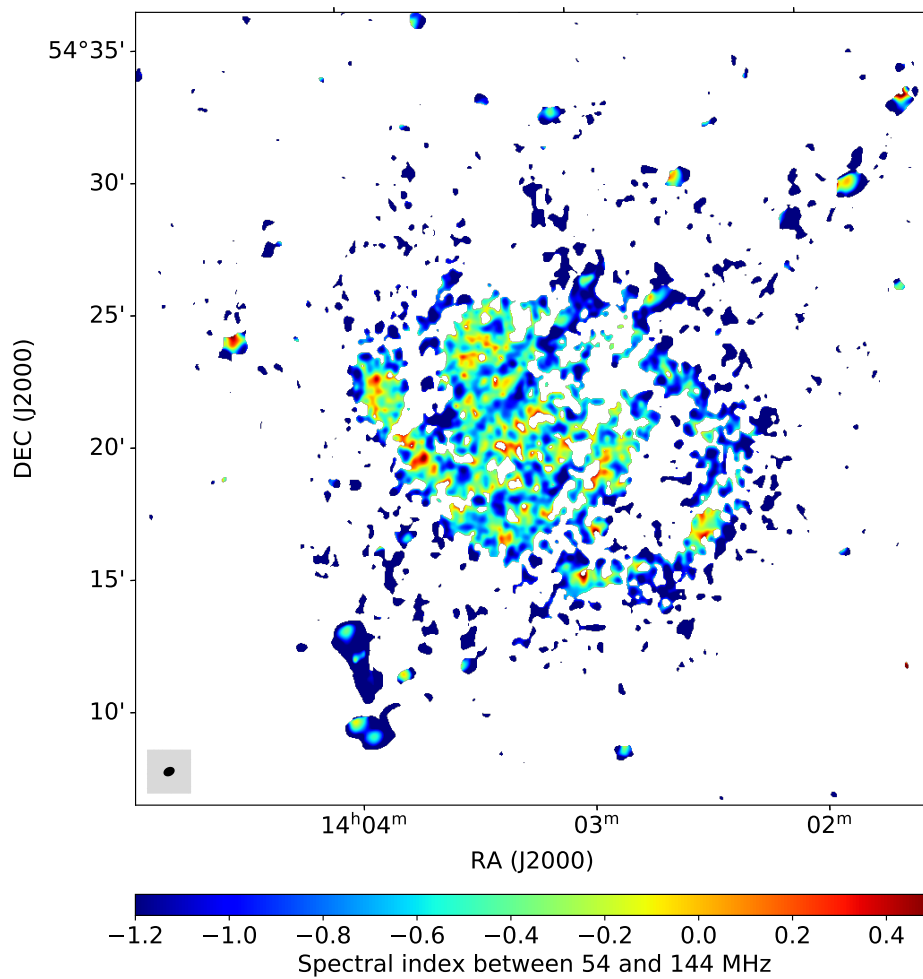


Figure 3.6: Spectral index map of M 101 between 54 and 144 MHz. White areas below 2σ are excluded. The beam size is shown with the black ellipse in the bottom left corner.

3 The low-frequency flattening of the radio spectrum of giant H II regions in M 101

The index of M 101 between 54 and 144 MHz is shown in Fig. 3.6 and the corresponding error map can be found in Appendix E. Significant areas of flat or inverted spectra index are present, especially at the positions of the H II regions.

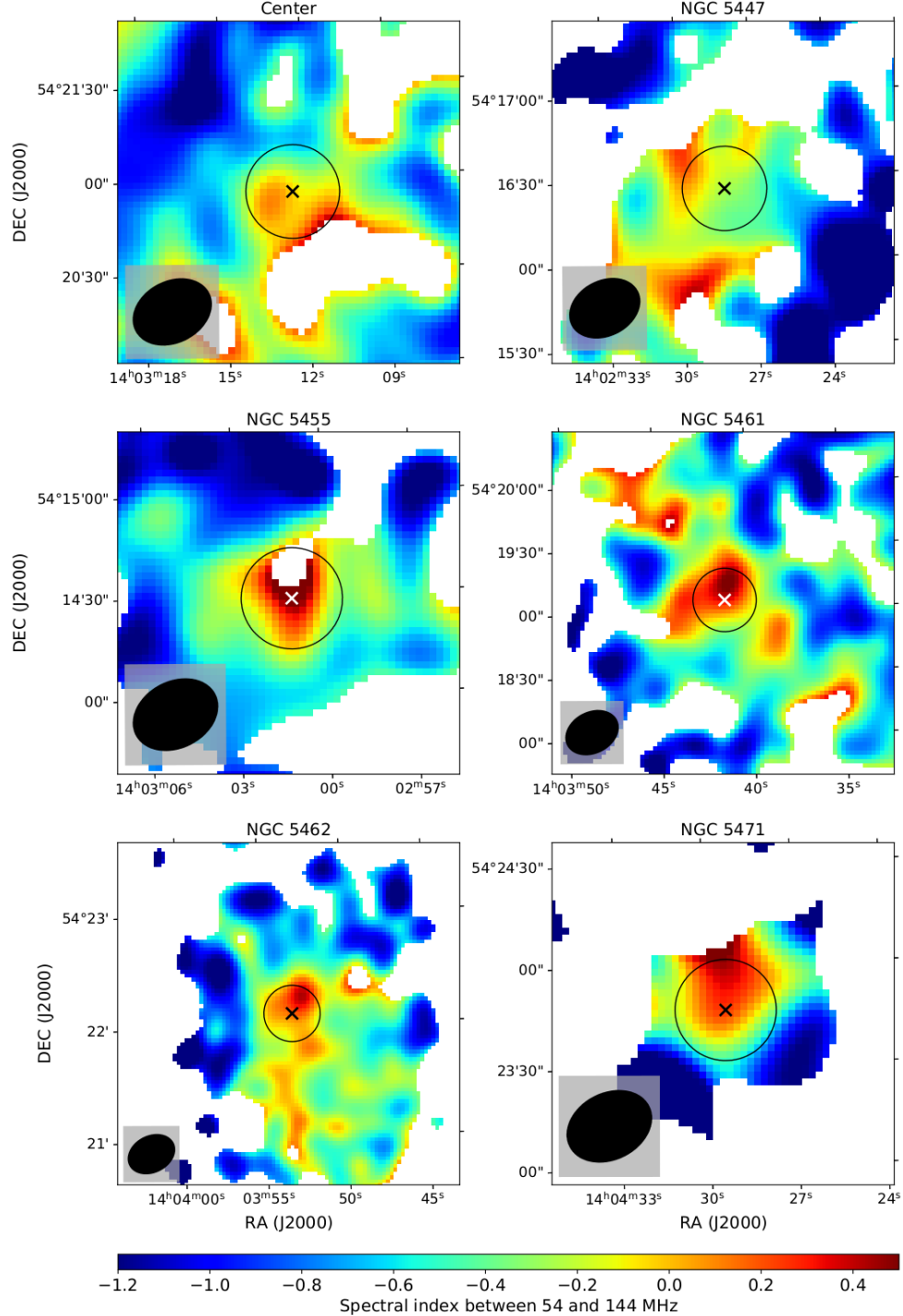


Figure 3.7: Zoomed-in spectral index maps of H II regions in M 101 between 54 and 144 MHz. The regions where the spectrum is measured (in Sect. 3.4.2) are indicated with black circles and the centres of the regions (Table 3.3) are marked with an x. White areas below 2σ are excluded. The beam size is shown with the black ellipse in the bottom left corner of each panel.

In Fig. 3.7 we present cutouts of the spectral index maps focused on the six H II regions that we selected for this study. For the majority of the regions we see a small area of positive spectral index right at the centre of several H II regions. There, we expect the highest free–free absorption because of high density of ionised gas. If we want to observe the turnover in the spectrum, we should focus on these very central areas.

3.4.2 SEDs of H II regions and fits

In the spectral index cutouts (Fig. 3.7) we see that there are areas of positive spectral index at the very centre of H II regions (except NGC 5447). For this reason we measure the spectra in circular areas with increasing size starting from the largest beam size (30'') up to twice the beam size (60'') with a 10'' step. These areas are centred on the position of the H II region according to Gordon et al. (2008), which are listed in Table 3.3. Alternative centres could be defined directly from H α data, but the position would not change more than the size of our beam and an alternative definition would not affect our results significantly. Here, we include measurements at all four frequencies (54, 144, 1370, and 4850 MHz) because the flux densities in small regions are accurate in all the maps, which we confirm by checking the spectra of background sources in Sect 3.3.1.

The spectra are shown in Fig. 3.8 with different lines indicating different areas within which the fluxes are measured. We can clearly see a deviation from a power law with decreasing area, or increasing resolution. We initially model the spectra using a synchrotron power law with an internal free–free absorbing medium. We make an assumption that in the H II region the absorbing thermal plasma coexists with the synchrotron-emitting CR electrons. Thus, the model assumes a thoroughly mixed medium of thermal gas and cosmic rays. This "internal" model includes emission and free-free absorption internal to a continuous synchrotron-emitting region. As in Kapińska et al. (2017), the model only considers the non-thermal synchrotron emission and the free–free absorption of that emission. At such low frequencies, the free–free emission is insignificant compared to the synchrotron emission so the free–free self-absorption is neglected and free–free absorption only affects synchrotron emission. Modelling the radio spectrum with a synchrotron power law with an internal free–free absorbing screen, the flux density S_ν depends on frequency as (Tingay & de Kool 2003):

$$S_\nu = S_0 \left(\frac{\nu}{\nu_0} \right)^\eta \left(\frac{1 - e^{-\tau_{\text{ff}}}}{\tau_{\text{ff}}} \right), \quad (3.1)$$

where S_0 is the flux density normalisation, ν is the frequency in GHz, $\nu_0=1$ GHz is the reference frequency, η is the absorption–free spectral index and τ_{ff} is the free–free emission optical depth. Here, the last term in the bracket on the right-hand side of the equation denotes the escape probability of the photons; this expression can be obtained by solving the radiation transport equation using the large-scale velocity approximation under the assumption of spherical symmetry (de Jong et al. 1975). In the expression for the free–free Gaunt factor at radio wavelengths from Brusaard & van de Hulst (1962), the optical depth is given as

$$\tau_{\text{ff}} = 8.2 \times 10^{-2} \nu^{-2.1} T_e^{-1.35} \text{EM}, \quad (3.2)$$

with the emission measure (EM) in units of $\text{cm}^{-6} \text{pc}$ and the electron temperature T_e in K. The EM is defined as

$$\left(\frac{\text{EM}}{\text{pc cm}^{-6}} \right) = \int_0^{s_0} \left(\frac{n_e}{\text{cm}^{-3}} \right)^2 \left(\frac{ds}{\text{pc}} \right), \quad (3.3)$$

where n_e is the thermal free electron density, and ds is the infinitesimal depth element along the line of sight between the source at s_0 and an observer at 0. We combine equations (3.2) and (3.1) to

3 The low-frequency flattening of the radio spectrum of giant H II regions in M 101

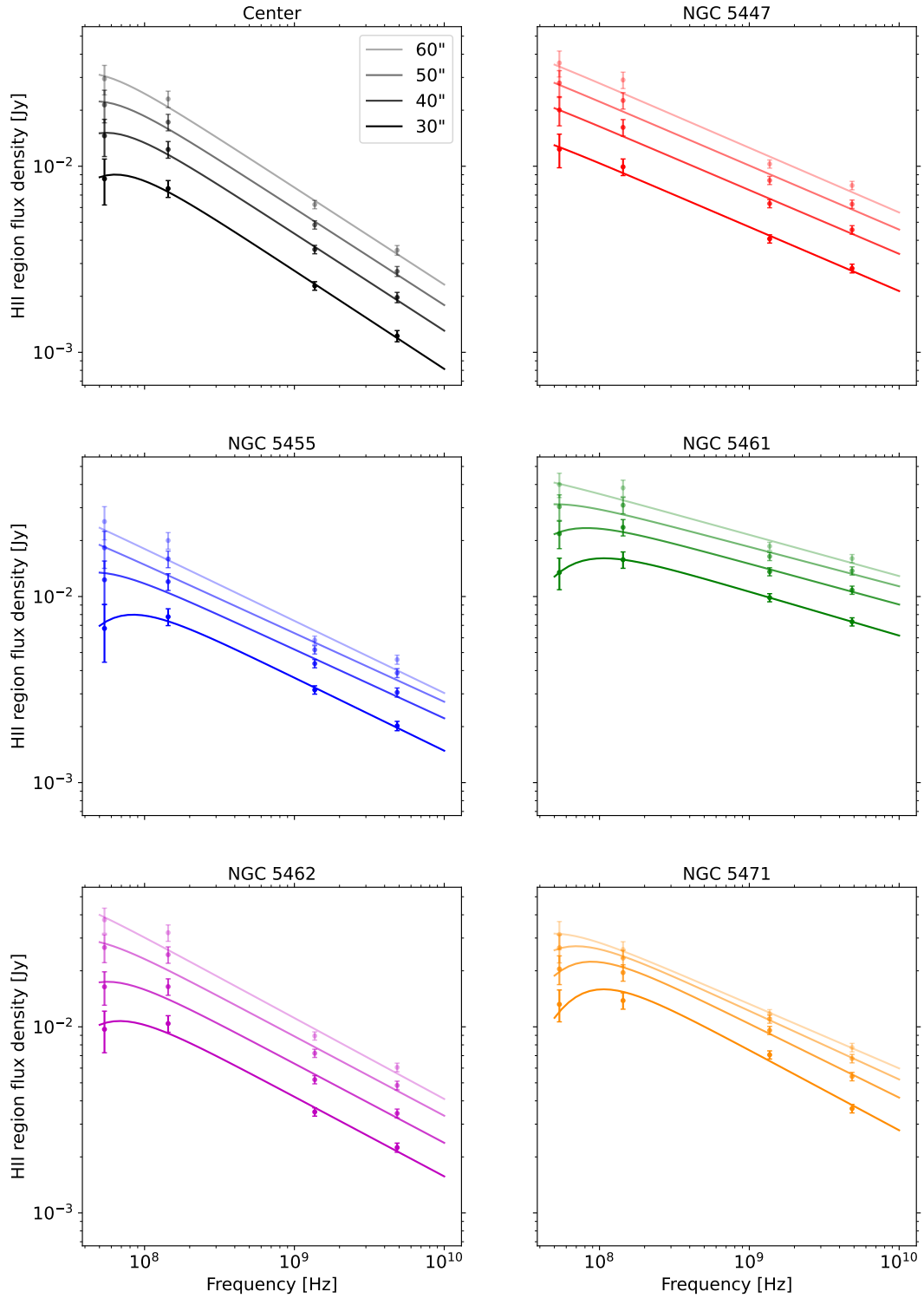


Figure 3.8: Spectra of the selected H II regions in M 101. The solid lines of different opacity correspond to fits for the free-free absorption model (combined Eq. 3.1 and 3.2) in different areas within which the flux is measured, with diameters from 30 to 60'' with a 10'' step. The fit parameters for the 30'' area are in Table 3.4.

Table 3.4: Fitted parameters for the spectra of the giant H II regions in M 101. The spectra are measured in areas with a 30'' diameter.

Region	Internal model		External model	
	η	EM [pc cm ⁻⁶]	η	EM [pc cm ⁻⁶]
Centre	-0.528 ± 0.044	5200 ± 5200	-0.528 ± 0.043	2500 ± 2200
NGC 5447	-0.344 ± 0.035	200 ± 3300	-0.343 ± 0.039	0 ± 1800
NGC 5455	-0.393 ± 0.041	6700 ± 6100	-0.392 ± 0.040	3200 ± 2600
NGC 5461	-0.236 ± 0.036	6600 ± 4100	-0.235 ± 0.035	3000 ± 1700
NGC 5462	-0.428 ± 0.041	4800 ± 4600	-0.429 ± 0.040	2300 ± 2000
NGC 5471	-0.431 ± 0.036	12300 ± 5300	-0.424 ± 0.034	4900 ± 1800

make a single free–free absorption fit model with three free parameters: S_0 , η and EM. The electron temperature is assumed to be $T_e = 10^4$ K. The value of electron temperature does not affect the shape of the spectrum, only the resulting value of EM.

Alternatively, the free–free absorption could occur in the intervening region (essentially a screen), which is also likely to contain thermal gas, in particular since the H II regions are small compared to the thickness of the disk. Our data cannot distinguish between this external model and the internal model presented in Eq. 3.1, both of them fit the data and they look remarkably similar. We use the internal model as our fiducial model. In an external model, the spectrum no longer has the optical depth in the denominator, yielding (Wills et al. 1997)

$$S_\nu = S_0 \left(\frac{\nu}{\nu_0} \right)^\eta e^{-\tau_{\text{ff}}}. \quad (3.4)$$

The external model leads to lower valued of EM because all the absorption occurs in front of the source thus requiring less ionised gas. The fit results for both models are in Table 3.4.

In most of the analysed H II regions the flux density at 54 MHz is significantly lower than it would be if the power law behaviour extended to lower frequencies. The exception is the region NGC 5447 where the spectrum is entirely a power law with no absorption at low frequencies. We exclude this region from further collective analysis and analyse it separately in Sect. 3.5.3.

We observe a flattening in the spectrum of H II regions at frequencies below 100 MHz. Assuming $T_e = 10^4$ K and the "internal" free-free absorption model we get values of the EM between 4800 and 12000 cm⁻⁶ pc. Fitting a different temperature does not change the fits because the parameter $T_e^{-1.35} \cdot \text{EM}$ enters the fit (Eq. 3.2). Hence changing T_e leads to a change in the inferred value of EM. Kennicutt et al. (2003b) measured T_e for each of the H II regions and the values for T_e vary between 9000 K and 12000 K for the low-ionisation zones. This would lead to a change in EM of 25% at most (which is less than other uncertainties). The initial values of EM are of the same order of magnitude but higher than the values determined for the spiral arms of M51 assuming that the flattening in the spectrum is caused by free–free absorption (Gajović et al. 2024). In Sect. 3.5.1 we compare the values of EM obtained by fitting the low frequency radio absorption to a different tracer of EM.

The spectral indices of the H II regions are very close for both models. Their values are between -0.52 and -0.22 which is fairly flat. Thermal emission has a spectral index -0.1 and non-thermal radio emission has a spectral index higher than -0.7. We observe a combination of thermal and non-thermal

emission coming from the centres of H II regions.

We note that synchrotron self-absorption is not a viable explanation for the spectral behaviour as it requires brightness temperatures well in excess of the ones we measure (see Gajović et al. 2024 for an exact calculation). Moreover, ionisation losses of the cosmic-ray electrons do not lead to spectral down-turns but only to a flattening of spectra. Also, since HII regions are already ionised, ionisation losses should not play a major role.

3.5 Discussion

3.5.1 Comparison to other EM tracers

One can independently estimate the EM from the H α flux density using the relation (Dettmar 1992; Voigtländer et al. 2013):

$$EM = 5 \cdot 10^{17} F_{H\alpha} / \Omega \quad (3.5)$$

where $F_{H\alpha}$ is the H α flux density in $\text{erg cm}^{-2} \text{s}^{-1}$, and Ω is the collecting area in arcsec^2 and EM is in $\text{cm}^{-6} \text{pc}$.

The H α fluxes for our H II regions (except for the galactic centre) are presented in Hippelein (1986) who adapted them from Israel & Kennicutt (1980). The exact collecting areas for each region are not available, but their diameters range between 20'' and 40''. We assumed a diameter of 30'' for all our regions, because this diameter matches the regions in which we measured the radio flux and

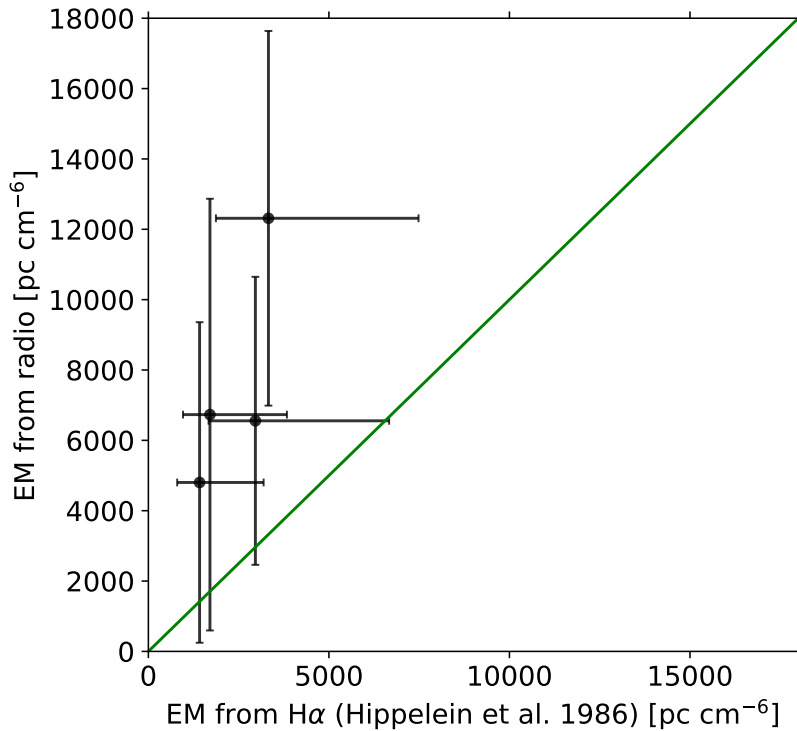


Figure 3.9: Comparison of EM values from the internal free-free absorption model fit to the radio data and EM values from H α . The 1:1 line is plotted in green.

the range of possible diameters for the $H\alpha$ measurements. The EM estimate using the $H\alpha$ flux density as proxy is compared to the EM obtained by fitting the internal free-free absorption model to the radio data in Fig. 3.9. We exclude the galactic centre because of missing $H\alpha$ data and NGC 5447 since we do not observe a turnover in that region.

The EM from radio and from $H\alpha$ is the same order of magnitude, but the radio fits are consistently about two times higher than the $H\alpha$ estimates. Here we plot the EM from the internal free-free absorption model (Eq. 3.1), however in Table 3.4 we show that the external model (Eq. 3.4) results in consistently lower values of EM. The values from the external model are about a factor of two lower, which is more in line with the $H\alpha$. This is an indication that the external model could be more appropriate for the spectra of H II regions. However, due to the high uncertainty on the radio fit results and the unknown area for $H\alpha$ measurements we cannot firmly claim which model is better.

3.5.2 Turnover localisation

The spectral index maps (Fig. 3.7) show inverted spectra right in the centres of the H II regions. In Fig. 3.8, it is clear that the turnover can only be observed if we focus on a small area around the centre of the H II region. We now investigate how the size of the area affects our ability to observe a flattening in the spectrum. We added up the fluxes of the five selected H II regions (excluding NGC 5447) to create the total H II region spectrum. To get a more precise view, we varied the size of the area in which the flux density is measured between $30''$ and $67.5''$ in steps of $7.5''$. In Fig. 3.10, we show how this affects the total H II region spectrum. We also fitted the free-free absorption model to those spectra. The fluxes of the H II regions are comparable so the total spectrum is not dominated by the brightest region.

From Fig. 3.10, we see that the low frequency flattening in the radio spectrum can not be detected

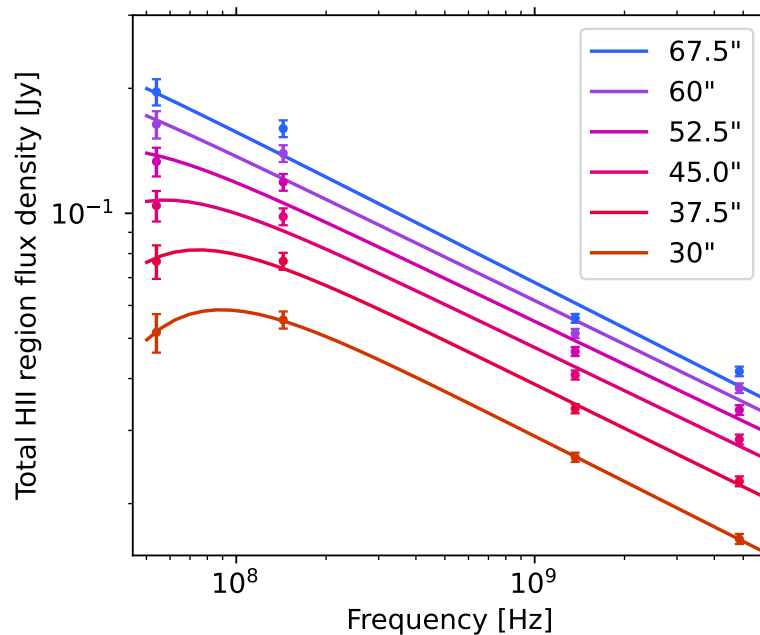


Figure 3.10: Total flux density of H II regions measured in increasing areas around the centre of the region. NGC 5447 is excluded.

3 The low-frequency flattening of the radio spectrum of giant H II regions in M 101

if the area in which the flux density of the H II region is measured has a diameter larger than $45''$. This corresponds to 1.5 kpc at the distance of M 101 (see Table 3.1). This means that the flattening is only observable in the very centre of the H II region. With the increase of the area we include more of the surrounding part of the H II region and the flattening gets "diluted".

It was already shown by Israel et al. (1975) that more than 50% (in some regions even up to 90%) of the radio flux density of the H II regions in M 101 is concentrated in the core. It is therefore not surprising that the free-free absorption is also most prominent in the cores, but it is interesting that the area where we detect the flattening has a diameter smaller than $1'$.

This has important implications for future studies of H II regions at very low frequencies. To detect the low frequency flattening, the resolution of the radio maps has to be high enough that the centres of the H II regions with the flattening can be resolved from the surroundings. Our results on M 101 show that the beam size should be small enough to correspond to 1.5 kpc or less in the observed galaxy. M 101 has exceptionally bright and dense H II regions, so we expect that an even better resolution might be needed in other galaxies. The international baselines of the LOFAR telescope allow to reach a resolution around $1''$ at 54 MHz (Groeneveld et al. 2022). If that is combined with SKA observations of similar resolution at higher frequency, in the future it could be possible to observe flattening in extra-galactic H II regions at distances up to 300 Mpc.

3.5.3 NGC 5447 at low radio frequencies

NGC 5447 is the H II region in which we do not see a flattening at frequencies down to 54 MHz (top right panel of Fig. 3.8). There are no known background radio sources that could affect the flux density in the location of NGC 5447. If we examine the spectral index of NGC 5447 (top right panel of Fig. 3.7), we see that around the centre of the region the spectral index is not inverted. There are only two patches with an inverted spectrum near the edges of the H II region. It is probably the case that the area in which we measure the spectrum, does not include the parts of the region where there is a flattening. If we look at the $H\alpha$ +continuum map of NGC 5447 (Fig. 3.11), it is revealed that this region consists of multiple distinct condensations, which can also be classified as separate H II regions. The area where we measure the spectrum in previous section is centred on the north-west condensation. We also try centring the area on the south-east condensation, but this does not change the result and we still do not detect a low frequency flattening. Our result can be explained if the free-free absorption only occurs in small condensations and our resolution is not sufficient to separate the emission with the turnover from the surroundings. This idea could be tested by higher resolution imaging using the international LOFAR stations. This region is also an exception in the work by Israel et al. (1975) because it is the only region in which they did not see a core component in 6 cm observations. With the perspective we get from our results, that could also be a consequence of the radio emission being produced by multiple distinct condensations and not one core.

Alternatively, different properties of NGC 5447 could be because of its position within M 101. It is located next to the big hole in the disk of M101 that hosts only hot X-ray gas and potentially strong vertical magnetic fields, which could be a result of heating by magnetic reconnection (Weżgowiec et al. 2022). It is possible that the hole influenced the structure of NGC 5447. In addition to that, the H II regions on the East of the galaxy could be different from NGC 5447 because of the tidal interaction of M101 with the galaxy to the east that also distorts the magnetic arm of M 101 (Weżgowiec et al. 2022).

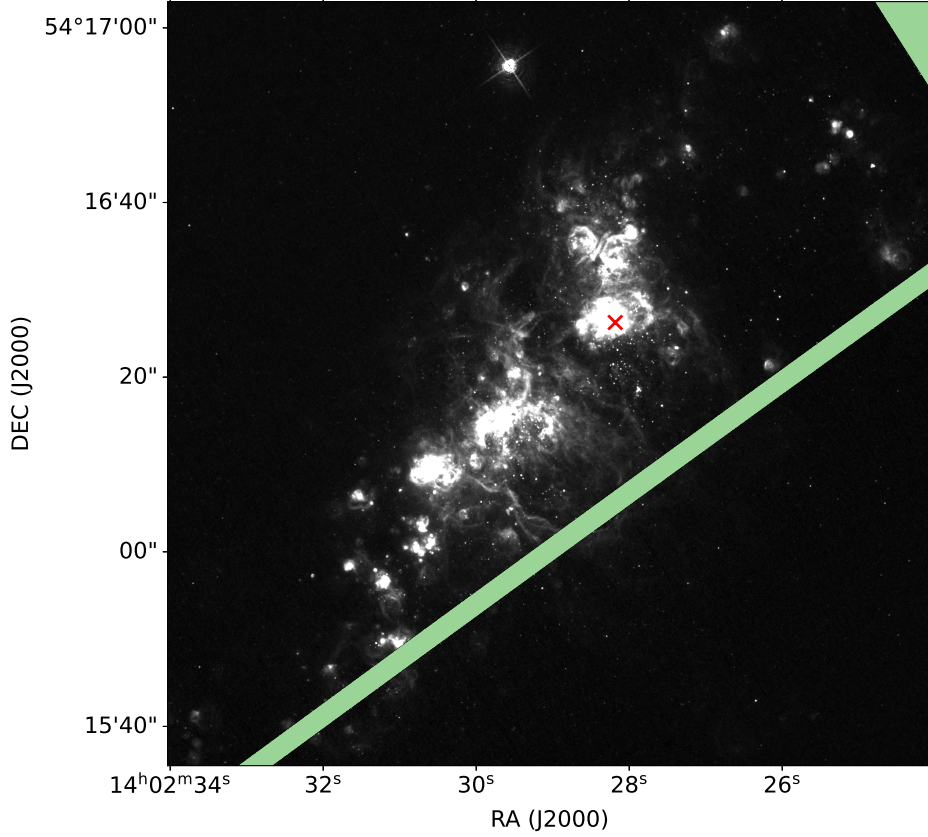


Figure 3.11: NGC 5447 in $H\alpha$ +continuum from the Hubble Legacy Archive¹. The pale green area was not observed. The red x marks the centre of the area in which we measured the spectrum.

3.5.4 Implication for spectral flattening and radio–FIR correlation

The nearly linear, tight correlation of far-infrared (FIR), and radio luminosity of star-forming galaxies is an important property to measure extinction-free star formation rates (Yun et al. 2001). This correlation can be explained if the cosmic ray electrons do not escape the galaxy in the so-called calorimetric model (Voelk 1989). However, in such a case the radio continuum spectra should be steep with integrated radio spectral indices around $\alpha \approx -1.1$ (see e.g. Lacki et al. 2010). The integrated radio spectral index of galaxies is an important proxy for energy losses and transport effects of cosmic-ray electrons. Synchrotron and inverse Compton radiation losses tend to steepen the radio continuum spectrum, whereas Bremsstrahlung and ionisation losses tend to flatten the spectrum. With our new results we can now quantify the importance of other effects, namely of free–free absorption. The mean emission measure of our $H\text{II}$ regions is $(7000 \pm 2600) \text{ pc cm}^{-6}$ for the internal model. According to Equation (3.2) the optical depth is $(2.3 \pm 0.8) \cdot 10^{-3}$ at 1 GHz and 0.28 ± 0.11 at 100 MHz. This means that the decrement due to free–free absorption can be neglected at 1 GHz and is of order 30% at 100 MHz. We expect that integrated over the entire galaxy, these values are even smaller as the free–free absorption occurs only in regions with dense ionised gas. This means that in regular star

¹Based on observations made with the NASA/ESA Hubble Space Telescope, and obtained from the Hubble Legacy Archive, which is a collaboration between the Space Telescope Science Institute (STScI/NASA), the Space Telescope European Coordinating Facility (ST-ECF/ESA) and the Canadian Astronomy Data Centre (CADC/NRC/CSA).

3 The low-frequency flattening of the radio spectrum of giant H II regions in M 101

forming galaxies, free–free absorption as a cause for spectral flattening may be neglected at frequencies $\gtrsim 100$ MHz. Only in the nuclei of starburst galaxies may such an explanation be worthwhile as both observations (Adebahr et al. 2013) and simulations (Werhahn et al. 2021) suggest.

The observed flat radio spectral indices (Fig. 3.8, Table 3.4), flatter than the canonical injection spectral indices, hint at other energy losses at work. Because they are not strongly frequency-dependent, we do not see a strong downturn at low frequencies. Also, the contribution of free–free emission will flatten the spectrum further at higher frequencies. A positive correlation between spectral curvature and neutral gas density was already found by Gajović et al. (2024) in M 51 corroborating the importance of low energy ionisation losses of the cosmic-ray electrons.

3.6 Conclusions

We present new radio continuum maps of M 101 at 54 and 1370 MHz. We study the giant H II regions at low radio frequencies. The centre of the galaxy and five giant H II regions (NGC 5447, NGC 5455, NGC 5461, NGC 5462, and NGC 5471) are selected for the analysis because they are bright at 144 MHz.

The spectral index between 54 and 144 MHz is negative in the very centres of the H II regions. The radio spectra of five out of six giant H II regions in M 101 show a flattening below 100 MHz. We do not see a turnover in the spectrum of NGC 5447, likely because it consists of several smaller condensations. The flattening observed in the majority of the selected regions can be well fitted with both the internal and external free-free absorption model and our data do not show preference for either model. The resulting EMs are about a factor of two lower for the external model and that is more in line with the EMs estimated from H α fluxes. This is an indication that the external free-free absorption model is better for H II regions, but because of high uncertainties it is only an indication.

Low-frequency flattening is only present in the very centre of the giant H II regions. The area where radio spectrum is measured has to be smaller than 1.5 kpc (corresponds to 45" in M 101) to detect a flattening. In the future, to detect the low frequency flattening in more distant H II regions, high resolution observations will have to be performed with the SKA and LOFAR international stations.

Our findings indicate that free–free absorption at frequencies around 100 MHz has an optical depth of ≈ 0.3 (Sect. 3.5.4). This means free–free absorption has to be taken into account when observing H II regions. Globally, however, the effect of free–free absorption is much smaller. This has important consequences when using radio continuum observations to measure extinction-free star-formation rates on kiloparsec scales at frequencies of $\lesssim 100$ MHz (e.g. Heesen et al. 2019).

Acknowledgements

We thank the anonymous referee for their comments, which helped to strengthen the conclusions of the paper. We thank M. Weżgowiec for providing the FITS files for the 4850 MHz maps. LG and MB acknowledge funding by the Deutsche Forschungsgemeinschaft (DFG, German Research Foundation) under Germany’s Excellence Strategy – EXC 2121 “Quantum Universe” – 390833306. BA and DJB acknowledge funding from the German Science Foundation DFG, via the Collaborative Research Center SFB1491 ‘Cosmic Interacting Matters – From Source to Signal’. FdG acknowledges support from the ERC Consolidator Grant ULU 101086378. LOFAR (van Haarlem et al. 2013) is the Low Frequency Array designed and constructed by ASTRON. It has observing, data processing, and data storage facilities in several countries, which are owned by various parties (each with their own funding sources), and that are collectively operated by the ILT foundation under a joint scientific policy. The ILT resources have benefited from the following recent major funding sources: CNRS-INSU, Observatoire de Paris and Université d’Orléans, France; BMBF, MIWF-NRW, MPG, Germany; Science Foundation

3.6 Conclusions

Ireland (SFI), Department of Business, Enterprise and Innovation (DBEI), Ireland; NWO, The Netherlands; The Science and Technology Facilities Council, UK; Ministry of Science and Higher Education, Poland; The Istituto Nazionale di Astrofisica (INAF), Italy. This research made use of the Dutch national e-infrastructure with support of the SURF Cooperative (e-infra 180169) and the LOFAR e-infra group. The Jülich LOFAR Long Term Archive and the German LOFAR network are both coordinated and operated by the Jülich Supercomputing Centre (JSC), and computing resources on the supercomputer JUWELS at JSC were provided by the Gauss Centre for Supercomputing e.V. (grant CHTB00) through the John von Neumann Institute for Computing (NIC). This research made use of the University of Hertfordshire high-performance computing facility and the LOFAR-UK computing facility located at the University of Hertfordshire and supported by STFC [ST/P000096/1], and of the Italian LOFAR IT computing infrastructure supported and operated by INAF, and by the Physics Department of Turin university (under an agreement with Consorzio Interuniversitario per la Fisica Spaziale) at the C3S Supercomputing Centre, Italy. The research leading to these results has received funding from the European Research Council under the European Union's Seventh Framework Programme (FP/2007-2013) / ERC Advanced Grant RADIOLIFE-320745. This research made use of the Python Kapteyn Package (Terlouw & Vogelaar 2015). Partly based on observations made with the NASA/ESA Hubble Space Telescope, and obtained from the Hubble Legacy Archive, which is a collaboration between the Space Telescope Science Institute (STScI/NASA), the Space Telescope European Coordinating Facility (ST-ECF/ESA) and the Canadian Astronomy Data Centre (CADC/NRC/CSA).

3 The low-frequency flattening of the radio spectrum of giant H II regions in M 101

4 Weakly interacting massive particle cross section limits from LOFAR observations of dwarf spheroidal galaxies

L. Gajović, F. Welzmüller, V. Heesen, F. de Gasperin, M. Vollmann, M. Brüggen, A. Basu, R. Beck, D. J. Schwarz, D. J. Bomans, A. Drabent *Astronomy & Astrophysics*, 673, p.A108 (2023)

Abstract

Context. Weakly interacting massive particles (WIMPs) can self-annihilate, thus providing us with a way to indirectly detect dark matter (DM). Dwarf spheroidal (dSph) galaxies are excellent places to search for annihilation signals because they are rich in DM and background emission is low. If $O(0.1\text{--}10\ \mu\text{G})$ magnetic fields in dSph galaxies exist, the particles produced in DM annihilation emit synchrotron radiation in the radio band.

Aims. We used the non-detection of 150 MHz radio continuum emission from dSph galaxies with the LOw Frequency ARray (LOFAR) to derive constraints on the annihilation cross section of WIMPs in electron–positron pairs. Our main underlying assumption is that the transport of the cosmic rays can be described by the diffusion approximation, which necessitates the existence of magnetic fields.

Methods. We used observations of six dSph galaxies in the LOFAR Two-metre Sky Survey (LoTSS). The data were reimaged, and a radial profile was generated for each galaxy. We also used stacking to increase the sensitivity. In order to derive upper limits on the WIMP cross section, we injected fake Gaussian sources into the data, which were then detected with 2σ significance in the radial profile. These sources represent the lowest emission we would have been able to detect.

Results. We present limits from the observations of individual galaxies as well as from stacking. We explored the uncertainty due to the choice of diffusion and magnetic field parameters by constructing three different model scenarios: optimistic (OPT), intermediate (INT), and pessimistic (PES). Assuming monochromatic annihilation into electron–positron pairs, the limits from the INT scenario exclude thermal WIMPs ($\langle\sigma v\rangle \approx 2.2 \times 10^{-26}\ \text{cm}^3\ \text{s}^{-1}$) below 20 GeV, and the limits from the OPT scenario even exclude thermal WIMPs below 70 GeV. The INT limits can compete with limits set by *Fermi*–LAT using γ -ray observations of multiple dwarf galaxies, and they are especially strong for low WIMP masses.

4.1 Introduction

Dark matter (DM) is known to interact gravitationally, and only weakly via other fundamental forces of nature, which makes it difficult to observe. Among the most promising candidates for DM are weakly interacting massive particles (WIMPs; Jungman et al. 1996), (quantum chromodynamics) axions (Peccei & Quinn 1977a,b; Weinberg 1978; Wilczek 1978) or axion-like particles (Kim 1987; Jaeckel & Ringwald 2010), massive compact halo objects (Alcock et al. 2000), sterile neutrinos (Ibarra 2015), primordial black holes (Hawking 1971), and modification of the Newtonian dynamics as an alternative to explain the effect of DM without additional mass (Milgrom 1983). WIMPs are particularly appealing candidates for DM and by far the most scrutinized.

In the WIMP hypothesis, the number density of DM particles freezes out when the expansion rate of the Universe becomes higher than their annihilation rate, so the number density of DM particles becomes constant. From this, the theoretical thermal relic annihilation cross section is calculated to be $\langle\sigma v\rangle \approx 2.2 \times 10^{-26} \text{ cm}^3 \text{ s}^{-1}$ for WIMP masses above 10 GeV and predicted to increase at lower masses (Steigman et al. 2012). There are also alternative production scenarios such as freeze-in, where DM never attains thermal equilibrium with the primordial plasma of standard model particles in the early Universe (Hall et al. 2010), as well as several scenarios where DM is in thermal equilibrium: hidden sector freeze-out (Finkbeiner & Weiner 2007; Cheung et al. 2011), zombie DM (Kramer et al. 2021), pandemic DM (Bringmann et al. 2021; Hryczuk & Laletin 2021), and others.

There is ongoing research attempting to directly detect WIMPs, for example EDELWEISS (Sanglard et al. 2005), the XENON-1T experiment (Aprile et al. 2017), and CRESST (Abdelhameed et al. 2019). Another way to achieve a detection is an indirect astrophysical search targeting particles that were created by or interacted with DM. Searches using γ -ray observations of nearby dwarf spheroidal (dSph) galaxies using the *Fermi* Large Area Telescope (*Fermi*-LAT; Ackermann et al. 2015; Hoof et al. 2020) and the High Energy Stereoscopic System (HESS; Aharonian et al. 2008) are able to provide new stringent upper limits for the WIMP annihilation cross section that depend on the particle mass. Recent work by Delos & White (2023) shows that if DM is thermally produced WIMPs, thousands of Earth-mass prompt cusps should be present in every solar mass of DM. This is manifested in a drastic increase in the expected DM annihilation signal compared to a smooth DM distribution, substantially tightening observational cross-section limits. The most recent γ -ray results (Hoof et al. 2020), assuming a smooth DM distribution, exclude the thermal relic annihilation cross section for WIMPs with masses of $\lesssim 100$ GeV annihilating through the quark and τ -lepton channels; and for WIMPs with masses of $\lesssim 20$ GeV annihilating through the electron-positron channel.

Radio continuum observations provide a complementary approach to constraining the WIMP annihilation cross section. Such searches exploit the fact that highly energetic electron-positron pairs (e^\pm pairs) produced by the annihilation of WIMPs give rise to synchrotron emission in the presence of magnetic fields (Colafrancesco et al. 2007). Although other WIMP annihilation channels can be explored, in this work we focus on WIMP self-annihilation into e^\pm pairs. For WIMP masses on the order of 10 GeV and microgauss (μG) magnetic fields, the critical frequency of synchrotron radiation, $\nu = 3eBE^2/(2\pi m_e^3 c^5)$, is on the order of a few gigahertz (Rybicki & Lightman 1986), which means the WIMP signal can only be detected at frequencies lower than that. Lowering the frequency below 1 GHz opens up the possibility for constraining WIMPs with masses down to 1 GeV.

Cosmic ray (CR) electrons and positrons produced via DM annihilation interact with the magnetic field and create an extended source that traces a diffusion halo due to the emitted synchrotron radiation. A common search strategy is to consider radial intensity profiles of the extended emission from these halos and compare them with modeled DM annihilation signals (Cook et al. 2020; Vollmann et al. 2020). Vollmann (2021) presents semi-analytical formulae for these models, which were

shown to be in reasonable agreement with the more sophisticated numerical methods (Regis et al. 2015, 2021).

Dwarf spheroidal galaxies are very promising systems to look for DM-related emission since in these systems the radio continuum emission is almost uncontaminated by baryonic emission of primary CR electrons due to a low level of star formation (Colafrancesco et al. 2007; Heesen & Brüggén 2021). Also, stellar-dynamical observations indicate that dSph galaxies are DM dominated (Geringer-Sameth et al. 2015), meaning that the signal from WIMP annihilation is expected to be bright compared to other types of galaxies. Most known dSph galaxies are satellites of either the Milky Way or the Andromeda galaxy and are therefore close to Earth. This allows us to resolve the spectra of their stellar light well, and the estimates of their DM content are relatively precise (Hütten & Kerszberg 2022).

The LOw Frequency ARray (LOFAR; van Haarlem et al. 2013) is the ideal instrument for radio continuum searches of WIMP annihilation. LOFAR is a radio interferometer operating at low frequencies, from 10 to 240 MHz. LOFAR combines the high angular resolution needed to identify compact background sources with the high sensitivity to extended emission needed to detect the signal from WIMPs. A LOFAR high band antenna (HBA) search for DM in the dSph galaxy Canes Venatici I using such a strategy was already performed by Vollmann et al. (2020). That proof-of-concept study shows that, for an individual galaxy, the limits are comparable to or even better than that from *Fermi*-LAT, assuming reasonable values for the magnetic field strength and diffusion coefficient. This work expands upon that study by considering six galaxies observed with LOFAR HBA. In order to improve the WIMP annihilation cross-section limits, we stacked the signal from these six galaxies in various ways. We thus present improved upper limits on the annihilation of low-mass WIMPs into e^\pm pairs in the GeV–TeV mass range using new radio continuum data.

This work is organized as follows. In Sect. 4.2 we present our theoretical calculations, where we convert the presence of DM into a radio continuum signal. Section 4.3 presents our employed methodology, including how we dealt with the LOFAR radio continuum data and how we improved our signal-to-noise ratio via both profile and image stacking. Section 4.4 contains our results. We finish off in Sect. 4.5, which contains the discussion and conclusions.

4.2 Dark matter calculations

4.2.1 Cosmic ray injection

The injection of standard model particles by WIMP annihilation is described by for example Lisanti (2017). The injection rate of CR electrons or positrons is expressed as

$$s(r, E) = \frac{\rho^2(r)}{2m_\chi^2} \frac{d\langle\sigma v\rangle}{dE} \Big|_{\chi\chi \rightarrow e^+e^-}, \quad (4.1)$$

where m_χ is the WIMP mass, E is the CR energy and r is the galactocentric radius. The injection rate also depends on the DM density profile $\rho(r)$ and the annihilation cross section $\langle\sigma v\rangle$. We assume a Navarro–Frenk–White (NFW; Navarro et al. 1997) model for the density profile given by

$$\rho_{\text{NFW}}(r) = \frac{\rho_s}{\frac{r}{r_s} \left(1 + \frac{r}{r_s}\right)^2}, \quad (4.2)$$

where ρ_s is the characteristic density and r_s is a scale length. The velocity- and spin-averaged cross section for WIMP annihilation into e^\pm pairs per unit energy are obtained as

4 WIMP limits from LOFAR observations of dwarf spheroidal galaxies

$$\frac{d\langle\sigma v\rangle}{dE} = \sum_{f^+f^-} \text{BR}_{f^+f^-}\langle\sigma v\rangle \frac{dN_{f^+f^- \rightarrow e^+e^-+X}}{dE}, \quad (4.3)$$

where $\text{BR}_{f^+f^-}$ is the branching ratio that describes the weighting of the elements for any standard model particle pair f^+f^- , into which the WIMPs will annihilate. This is calculated with for example the Fortran package `DARKSUSY` (Bringmann et al. 2018), but we assume annihilation into monochromatic electron–positron pairs. Then the derivative in Eq. (4.3) simplifies to $\frac{dN_{f^+f^- \rightarrow e^+e^-+X}}{dE} = \delta(E - m_\chi)$. Once an electron or positron is injected into the DM halo, it diffuses through the turbulent magnetic field in the halo of the dSph galaxy while emitting synchrotron radiation.

4.2.2 Cosmic ray diffusion

The electron mass is always much lower than the WIMP mass, $m_e \ll m_\chi$, so the e^\pm pairs are ultra-relativistic. Since magnetic fields in galaxies are mostly turbulent (Beck 2015), we assume the propagation of e^\pm pairs to be dominated by diffusion (Colafrancesco et al. 2007; Regis et al. 2014). Hence, the CR propagation is described with the stationary diffusion–loss equation, which we adopt as our transport model. Due to the spherical geometry of dSph galaxies, we further assume an isotropic momentum distribution, such that the diffusion–loss equation depends only on galactocentric radius, r , and CR energy:

$$D(E) \frac{1}{r} \frac{\partial^2}{\partial r^2} [n_e(r, E)r] + \frac{\partial}{\partial E} [b(E, B)n_e(r, E)] + s(r, E) = 0. \quad (4.4)$$

The parameter $b(E, B)$ describes the total energy loss-rate and $D(E)$ describes the diffusion coefficient. As a boundary condition, we assume that the CR number density (per unit volume and energy) n_e vanishes at diffusion-halo radius r_h , as the diffusion coefficient rises to infinity due to vanishing magnetic fields, so that $n_e(r_h, E) = 0$. We assume that r_h is on the order of the half-light radius r_\star . These assumptions, including stationarity, are well justified and became the de facto standard over the years (Colafrancesco et al. 2006; McDaniel et al. 2017).

Contributions to the total energy loss include synchrotron radiation, $b(E, B)_{\text{sync}}$, and inverse Compton scattering, $b(E, B)_{\text{ICS}}$, losses. Other energy losses, such as bremsstrahlung and ionization losses, are suppressed due to the low density of both ionized and neutral gas (Regis et al. 2015). The total energy loss of ultra-relativistic CR e^\pm in nearby galaxies (at redshift $z = 0$) is then

$$b(E, B) = b_{\text{sync}}(E, B) + b_{\text{ICS}}(E, B) \approx 2.546 \times 10^{-17} \left[1 + \left(\frac{B}{3.24 \mu\text{G}} \right)^2 \right] \left(\frac{E}{1\text{GeV}} \right)^2 \text{GeV s}^{-1}, \quad (4.5)$$

where B is the magnetic field and $3.24 \mu\text{G}$ is the field with the energy density of the cosmic microwave background (CMB) photons at $z = 0$. Inverse Compton scattering on radiation fields other than the CMB can be neglected. This is because the radiation energy density due to stellar light, u_\star , is quite low in comparison to that of the CMB, u_{CMB} , with $u_\star/u_{\text{CMB}} \approx 0.3\% \left(L_V/10^6 L_\odot \right) (r_\star/\text{kpc})^{-2}$, where L_V is the V-band luminosity (Vollmann 2021).

The average magnetic field strength in dSph galaxies is generally poorly known. In order to observe any radio continuum emission, the CR electrons have to be confined to the plasma, which implies that the magnetic field energy density cannot be too low in comparison with the CR energy density, even if the exact relation is not clear. For our typical sensitivities of $0.25\text{--}0.5 \text{ mJy beam}^{-1}$, frequency $\nu = 144 \text{ MHz}$, beam size $20''$, spectral index $\alpha = -0.8$, path length $l = 400 \text{ pc}$, and proton/electron ratio $K_0 = 0$, an equipartition magnetic field strength of $\approx 2 \mu\text{G}$ is calculated for an

e^\pm -plasma (Beck & Krause 2005). We adopted a more conservative value of $1 \mu\text{G}$ here, but varied it by an order of magnitude to account for the large uncertainties.

For the diffusion coefficient, we assume an energy-dependent power law,

$$D(E) = D_0 \left(\frac{E}{1 \text{ GeV}} \right)^\delta, \quad (4.6)$$

where $D_0 = D(1 \text{ GeV})$ and the power-law index, δ , describes the energy dependence, which is determined by the adopted turbulence model. The diffusion coefficient and its energy dependence in dSph galaxies are prone to uncertainties. We adopted a value of $10^{27} \text{ cm}^2 \text{ s}^{-1}$ for D_0 , which is in agreement with observations of nearby dwarf irregular systems (Murphy et al. 2012; Heesen et al. 2018). As no measurements exist for diffusion in dSph galaxies, we varied D_0 within two orders of magnitude. For the energy dependence, we assumed Kolmogorov-like turbulence resulting in $\delta = \frac{1}{3}$ (Kolmogorov et al. 1991). This model is supported by observations of the Milky Way (Korsmeier & Cuoco 2016). A key question is to what extent there is turbulence in the magnetic field structure, if it is present at all. Observations of the Milky Way and other galaxies usually fall into the two categories. Either the turbulence is extrinsically generated, where turbulence cascades down from large scales to the small scales relevant for CR scattering; or the turbulence is intrinsically generated by the CRs themselves via plasma instabilities. The latter scenario is usually referred to a self-confinement (Zweibel 2013). Because in dSph galaxies there is presumably no external source of turbulence such as supernova remnants, the self-confinement scenario is probably more appropriate. In star-forming galaxies this is likely the case as well for CRs with energy of a few GeV, where observations indicate a weaker energy dependence for CRs with less than 10 GeV energy (Heesen 2021). This is hence another source of uncertainty, at least for low WIMP masses.

4.2.3 Model scenarios

In order to deal with the uncertainties in the diffusion coefficient, D_0 , and the magnetic field strength, B , we employed three different model scenarios. Our standard values ($D_0 = 10^{27} \text{ cm}^2 \text{ s}^{-1}$, $B = 1 \mu\text{G}$) define the "intermediate" (INT) scenario. In the "optimistic" (OPT) scenario, we chose values that boost the DM signal. With a diffusion coefficient of $10^{26} \text{ cm}^2 \text{ s}^{-1}$ and an average magnetic field strength of $10 \mu\text{G}$, the CRs diffuse slowly and emit more synchrotron radiation due to the strong magnetic field. We note that these values are highly optimistic and probably unrealistic, but they serve us as a reference point for the maximum signal we might possibly expect. Such a high magnetic field strength is only observed in regions of concentrated star formation in nearby dwarf irregular galaxies (Hindson et al. 2018). In the "pessimistic" (PES) scenario, we used a high diffusion coefficient of $10^{29} \text{ cm}^2 \text{ s}^{-1}$ in a comparably weak magnetic field of $0.1 \mu\text{G}$. In this situation, the CRs emit less synchrotron radiation and the DM signal is lower. For such weak fields, most of the CR electron energy, whether primary or secondary, would be lost via inverse-Compton radiation.

This study does not cover the case in which the magnetic-field strengths are even weaker than $O(0.1 \mu\text{G})$. In this case, a ballistic description for the CR electron propagation would be more appropriate. Since we cannot exclude this possibility theoretically nor observationally, its study is left for future work.

4.2.4 Diffusion regimes

Because the full solution of the diffusion-loss equation (Eq. 4.4) is rather complicated, Vollmann (2021) defines three regimes, which allow one to simplify the solution. These regimes depend on the

4 WIMP limits from LOFAR observations of dwarf spheroidal galaxies

ratio of the CR diffusion timescale to the energy loss timescale. The diffusion timescale is

$$\tau_{\text{diff}} = \frac{r_h^2}{D(E)}, \quad (4.7)$$

where r_h is again the radius of the diffusion halo. As already mentioned, we assume that r_h is on the order of the half-light radius, r_\star .

The loss timescale from synchrotron radiation and inverse Compton scattering of CRs is

$$\tau_{\text{loss}} = \frac{E}{b(E, B)} = 1.245 \left(1 + \left(\frac{B}{3.24 \mu\text{G}} \right)^2 \right)^{-1} \left(\frac{E}{1 \text{ GeV}} \right)^{-1} \text{ Gyr}. \quad (4.8)$$

When $\tau_{\text{diff}} \gg \tau_{\text{loss}}$, one can assume that the CRs lose all their energy so rapidly that diffusion can be neglected and the first term in Eq. (4.4) vanishes. We refer to this assumption as "regime A" or the no-diffusion approximation. "Regime B" is defined such that $\tau_{\text{diff}} \approx \tau_{\text{loss}}$. In this regime the we have to consider the full solution of Eq. (4.4). Vollmann (2021) shows that the solution can be expressed as the sum of Fourier-like modes as a function of radius, where we consider only the leading term in this expansion. For $\tau_{\text{diff}} \ll \tau_{\text{loss}}$, one can neglect the second term of Eq. (4.4), as the CRs diffuse so rapidly that they leave the dSph galaxy without losing energy. We refer to this assumption as "regime C" or the rapid-diffusion approximation.

4.2.5 Synchrotron signal occurrence

The radio continuum intensity, I_ν , is the integral of the radio emissivity, $j_\nu(r)$, along the line of sight (LoS):

$$I_\nu = \int_{\text{LoS}} dl j_\nu(r(l)). \quad (4.9)$$

Following Vollmann (2021), the emissivity can be separated into a halo part, $H(r)$, a spectral part, $X(\nu)$, and a normalizing pre-factor,

$$j_\nu(r) = \frac{\langle \sigma \nu \rangle}{8\pi m_\chi^2} H(r) X(\nu). \quad (4.10)$$

Both the halo and the spectral part depend on the diffusion regime. The regime-specific equations for the halo factors are presented in Vollmann (2021). For the halo part, we employ the leading-mode approximation (regime B). For the NFW profile (Eq. 4.2) the halo function is

$$H_B(r) = h_B \frac{1}{r} \sin\left(\frac{\pi r}{r_h}\right), \quad (4.11)$$

where h_B is the halo factor in units of $\text{GeV}^2 \text{ cm}^{-5}$, which contains the part of H_B that is independent of radius:

$$h_B = 2 \left[\text{si}(\pi) - \frac{8r_h}{\pi r_s} + \dots \right] \frac{\rho_s^2 r_s^2}{r_h} \quad \text{where} \quad \text{si}(x) = \int_0^x dt \frac{\sin(t)}{t}. \quad (4.12)$$

It should be noted that Eq. (4.11) is a simplified version only valid for emissivities. In order to compare with our measured intensities, we implemented the actual halo factor as calculated for intensities (see Vollmann 2021, Appendix B).

For the spectral part, it is not viable to only consider one regime, as $X(\nu)$ strongly depends on the environment, for example which energy loss mechanism is dominant in the specific situation. Hence, we used all three spectral parts for the regimes A, B, and C, respectively, from Vollmann (2021):

$$X_A(\nu) = \frac{2\sqrt{3}e^3 B}{m_e} \int dz \frac{F(z)}{z} \frac{E(\nu/z)}{b(E(\nu/z))} \int_{E(\nu/z)}^{\infty} dE S(E), \quad (4.13)$$

$$X_B(\nu) = \frac{2\sqrt{3}e^3 B}{m_e} \int dz \frac{F(z)}{z} \frac{E(\nu/z)}{b(E(\nu/z))} e^{-\eta(E(\nu/z))} \int_{E(\nu/z)}^{\infty} dE S(E) e^{\eta(E)},$$

$$X_C(\nu) = \frac{2\sqrt{3}e^3 B}{m_e} \frac{r_h^2}{\pi^2} \int dz \frac{F(z)}{z} \frac{E(\nu/z) S(E(\nu/z))}{D(E(\nu/z))}; \quad (4.14)$$

with $\eta(E) = \frac{\pi^2}{r_h^2} \int_E^{\infty} dE' \frac{D(E')}{b(E')}$. The function $F(x)$ is described by Ghisellini et al. (1988) as

$$F(x) = x^2 \left[K_{\frac{4}{3}}(x) K_{\frac{1}{3}}(x) - x \frac{3}{5} \left(K_{\frac{4}{3}}^2(x) - K_{\frac{1}{3}}^2(x) \right) \right], \quad (4.15)$$

where $K_i(x)$ is the modified Bessel functions of the second kind. For monochromatic e^\pm injection, the CR energy is given by $E(\nu) = \sqrt{2\pi m_e^3 \nu / (3eB)}$ and the spectral injection function is $S(E) = \delta(E - m_\chi)$. All three spectral part formulae are related, where X_A and X_C are the limits for X_B when assuming $\eta \rightarrow 0$ and $\eta \rightarrow \infty$, respectively.

Assuming that the total radio emissivity is due to DM annihilation, it is straightforward to see that the shape of the radial profile is determined only by the halo function $H(r)$ of Eq. (4.10). We can therefore express the emissivity as

$$j_\nu(r) = N_B \cdot H_B(r), \quad (4.16)$$

where N_B is referred to as the signal-strength parameter that contains all the terms that do not depend on the radius (Vollmann 2021). Now we get an expression for the cross section in terms of N_B :

$$\langle \sigma \nu \rangle = \frac{8\pi m_\chi^2 N_B}{X_j(\nu)}, \quad (4.17)$$

where $j \in \{A, B, C\}$ specifies the diffusion regime. A similar approach is used in Regis et al. (2014) and Vollmann et al. (2020). The factor N_B connects predictions to observations, as it is proportional to the intensity of the DM signal in the radio band.

4.3 Methodology

4.3.1 LoTSS observations

The data used for our analysis are observed as part of the LOFAR Two-metre Sky Survey (LoTSS; Shimwell et al. 2017, 2019) and published in the second data release (LoTSS-DR2; Shimwell et al. 2022). LoTSS is a deep low-frequency survey with LOFAR HBA at 144 MHz with 24 MHz bandwidth. LoTSS-DR2 includes observations of 841 pointings and covers 5634 square degrees of the northern hemisphere. LoTSS data have a maximum angular resolution of 6'', referred to as high-resolution data, and additional low-resolution data at 20'' angular resolution. The high-resolution data were important for the subtraction of point-like sources, whereas the low-resolution data allowed us

4 WIMP limits from LOFAR observations of dwarf spheroidal galaxies

Table 4.1: Properties of the galaxies in our sample from LoTSS-DR2.

dSph	R.A. (J2000) [h m s]	Dec. (J2000) [° ' '']	r_* [pc]	d [kpc]	r_s [kpc]	ρ_s [GeV cm ⁻³]	rms-noise [μ Jy beam ⁻¹]	Ref.
CVnI	13:28:03.5	+33:33:21	564	218	2.27	0.5186	115	1
UMaI	10:34:52.8	+51:55:12	319	97	3.20	0.5473	74	1
UMaII	08:51:30.0	+63:07:48	149	32	4.28	2.794	60	1
UMi	15:09:08.5	+67:13:21	181	76	0.394	12.10	103	1
Will	10:49:23.0	+51:01:20	21	38	0.173	15.18	83	2, 3, 4
CVnII	12:57:10.0	+34:19:15	74	160	8.04	1.331	68	1

References: (1) Geringer-Sameth et al. (2015); (2) Martin et al. (2008); (3) Willman et al. (2011); (4) Sánchez-Conde et al. (2011).

to detect extended emission at high signal-to-noise ratios. The rms noise at 20'' resolution is 50–100 μ Jy beam⁻¹ (Shimwell et al. 2022).

We analyzed six dSph galaxies that are observed in the LoTSS-DR2. These galaxies have half-light radii between 20 and 600 pc with distances between 30 and 218 kpc (see Table 4.1). These galaxies are Canes Venatici I (CVnI), Ursa Major I (UMaI), Ursa Major II (UMaII), Ursa Minor (UMi), Willman I (Will), and Canes Venatici II (CVnII). These are the only non-disturbed dSph galaxies observed with the LOFAR HBA at this point in time. Additional four galaxies with declinations above +20° (Geringer-Sameth et al. 2015) could be observed in the future. LOFAR sensitivity is greatly reduced at lower declinations (Shimwell et al. 2017), but with longer observational times it is possible to observe additional six galaxies with declinations between +10° and +20° (Geringer-Sameth et al. 2015; Ackermann et al. 2015).

4.3.2 Reimaging the LoTSS data

We use recalibrated LoTSS data, where the calibration was specially tailored to our dSph galaxies (van Weeren et al. 2021). We reimaged the (u, v) data with WSCLEAN v2.9 (Offringa et al. 2014; Offringa & Smirnov 2017). The points in the (u, v) -plane were weighted using Briggs robust weighting as a compromise between uniform and natural weighting. A robustness parameter of `robust=-0.2` was found to produce the highest signal-to-noise ratio for the extended emission on the scales that we are interested in. Further imaging parameters are listed in Appendix G.

We excluded emission on large angular scales ($\gtrsim 1^\circ$) that can be attributed to the Milky Way (Erceg et al. 2022) by excluding (u, v) data at short baselines. We used lower limits to the (u, v) range between 60 and 400 λ , corresponding to angular scales from 7' to 46', making sure that these scales are not smaller than the size of the galaxy. Compact sources were subtracted from the (u, v) data prior to imaging. This was done by first producing a source catalog with the Python Blob Detector and Source Finder (PyBDSF; Rafferty, D. and Mohan, N. 2019). Since not all background sources have a point-like nature, we additionally used the "à trous wavelet decomposition module" integrated in PyBDSF. This module decomposes the residual maps resulting from the internal subtraction of the fitted Gaussians into wavelets of different scales (see Holschneider et al. 1989). We used between two and five wavelet scales depending on the galaxy. Sources were then subtracted as Gaussians from the

(u, v) data using the Default Pre-Processing Pipeline software (DPPP; van Diepen et al. 2018).

The maps were deconvolved with the multi-scale and auto-masking options to remove any residuals comparable to the size of the galaxies. Maps were then restored with a Gaussian beam at $20''$ angular resolution. The reimaging steps (as well as further steps in the cross-section limits calculation) were automated using PYTHON.¹

4.3.3 Calculation of the cross-section upper limits

To constrain the annihilation cross section of WIMPs, we used central amplitudes of the radial intensity profiles. To generate the radial profiles, we averaged intensities within annuli of increasing radius and constant width. For every galaxy, the width of an annulus was set to $20''$, which is equal to the full width at half maximum (FWHM) of the restoring Gaussian beam.

The expected shape of the radial profile is described by the halo function (Eq. 4.11). To analyze the observed radial profiles we approximate the shape as a fixed-width Gaussian with a FWHM equal to r_* . We note that the halo function depends on the density squared so the FWHM should indeed be approximated with r_* instead of $2r_*$, which we would expect from the density distribution. We varied the Gaussian central amplitude to best fit the observed radial profile. Since the size of the dSph galaxy diffusion radius is mostly unknown, it is important to verify the non-detection of a DM-related signals on various scales, not only the one we assumed earlier. Hence, we varied the FWHM of the Gaussians using values that are higher and lower than r_* .

To mimic a DM halo, we injected fake sources directly into the point-source subtracted (u, v) data. The fake source was constructed as a two-dimensional Gaussian with the FWHM equal to the stellar radius of the galaxy. This is a simplification as the real signal may be of a different shape. The simplification, however, has only a negligible effect on our inferred limits. The amplitude of the Gaussian was varied until we got a 2σ detection by fitting a Gaussian to the radial profile, as for the purely observational profile. Since the Gaussian FWHM was fixed for each dSph galaxy, the only free parameter was the central amplitude, a , which is related to the factor N_B in Eq. (4.17). The transformation between the central amplitude of the Gaussian radial intensity distribution, a , and the factor N_B was done using the halo factor (Eq. 4.12):

$$N_B = \frac{\pi(0.4)^2}{2h_B} a, \quad (4.18)$$

where the numerical factors account for the different shapes of the Gaussian source fitted to the data and assumed form of the halo function described by Eq. (4.11). Specifically, the width w (equivalent to the standard deviation) of the Gaussian is equal to $w = r_*/(0.4d)$. Additionally, the spectral function approximation was calculated for the appropriate scenario. The upper limits on the cross section were determined as a function of WIMP mass by inserting N_B into Eq. (4.17).

4.3.4 Stacking

In addition to looking at each galaxy separately, we combined the data from all galaxies through stacking. We used two different approaches for stacking the data. The first was to generate the radial profile for each galaxy separately, then to rescale to the stellar radius, and then stack the profiles. The second approach was to rescale and stack the images, and only then generate the radial profile from the stacked image.

¹<https://github.com/FinnWelzmueller/wimpsSoftware>

Stacking radial profiles

Our first approach to stacking the data was to stack the radial intensity profiles that are rescaled to the stellar radius. We used the stellar radius instead of the NFW scaling radius as it is the much more reliable observable. We set the width of the annuli in which the radio intensity is averaged to $0.05r_*$ for each galaxy. This was larger than the beam FWHM for most, but not all, galaxies, which might cause a slight correlation between adjacent data points. Each data point in the radial profile was expressed in terms of r_* and the intervals between them were equal even if the actual size on the sky is different. We note that the intensities did not have to be corrected for distance. The rescaled radial profiles were combined by calculating the noise-weighted mean. By fitting a Gaussian to the stacked profiles we confirmed they are consistent with zero.

After that we needed to handle the fake sources to be able to calculate the limits on the cross section. We first stacked the profiles with same fake sources as for the individual galaxies. The significance of the detection was higher than 2σ so in the stacked profile we could detect a fainter DM signal. To determine exactly how much fainter, we lowered the intensity of all the injected sources by a common factor, so the flux density ratio between the galaxies remained the same as in the individual analysis. This factor was chosen to achieve a detection with a significance of 2σ in the stacked radial profile.

Once we had the stacked radial intensity profile for all galaxies, we repeated the fitting to determine the combined value for the Gaussian amplitude, a . To calculate limits on the cross section from the combined data of our galaxies, we used this value for a and averaged all the other terms in Eq. (4.17) for each WIMP mass and each scenario. This is justified because by averaging the other terms we calculated the average emission from galaxies and this is exactly what we got when stacking.

Stacking images

Our second approach to stacking was to combine the galaxies in image space. This was done in the following steps:

1. A rescaled cutout image of every galaxy was created with a size of $4r_*$ and 1367×1367 pixel². The dimension in pixels was the median of all galaxies while ensuring there were at least seven pixels per beam FWHM. After the rescaling process, a single pixel sampled a larger section of the sky for galaxies with a larger angular diameter, compared to those with a small angular diameter, but this was a necessary compromise that we need to make for the image stacking. After this procedure, diffuse sources with equal flux density would appear identical, regardless of the distance and the stellar radius of the galaxy.
2. The flux density variance σ was calculated inside an annulus with an inner radius of r_* and an outer radius of $2r_*$.
3. All images were stacked using the weighted mean. The weight was adopted as the inverse square variance ($1/\sigma^2$) of each image, so that galaxy images with lower noise contributed more to the stacked image. Cosmological surface brightness dimming is negligible because the galaxies are in the Local Group so we have not applied any weighting with redshift.

From the final stacked image we generated the radial intensity profile (using the same algorithm as for the individual profiles) and confirmed a non-detection. To calculate the limits on the cross-section, we followed the same procedure as for the profile stacking. We adjusted the multiplication factors of injected sources and obtained the Gaussian amplitude, a . This combined value for a was

used in the calculation for the cross-section limits. Other necessary parameters that depend on galaxy properties were averaged.

4.4 Results

Our presentation of the results is split into three parts. We start with individual limits on the WIMP annihilation cross section (Sect. 4.4.1). In Sect. 4.4.2 we present the combined limits from the stacking algorithm. Finally, in Sect. 4.4.3 we discuss the limitations of our results.

4.4.1 Individual limits

Of the individual galaxies, we present first results of CVnI, which is already analyzed by Vollmann et al. (2020) using the same technique but with a slightly different implementation of other software. This galaxy serves as a benchmark to test our data processing algorithm. The radial intensity profiles with and without fake source are shown in Fig. 4.1. The amplitude of the Gaussian fitted to the observational data should be compatible with zero within the uncertainties to verify the non-detection of DM-related signals. Contrary, the amplitude of the Gaussian fitted to the data with the added fake source should be detected at 2σ significance. This is indeed the case, as the best-fitting amplitude for the profile including the injected source is $(36 \pm 13) \mu\text{Jy beam}^{-1}$ whereas without fake source it is $(9 \pm 15) \mu\text{Jy beam}^{-1}$ at a FWHM of 8.2 arcmin. In Table 4.2, we summarize the fitting results for each galaxy with the corresponding profiles presented in Appendix F.

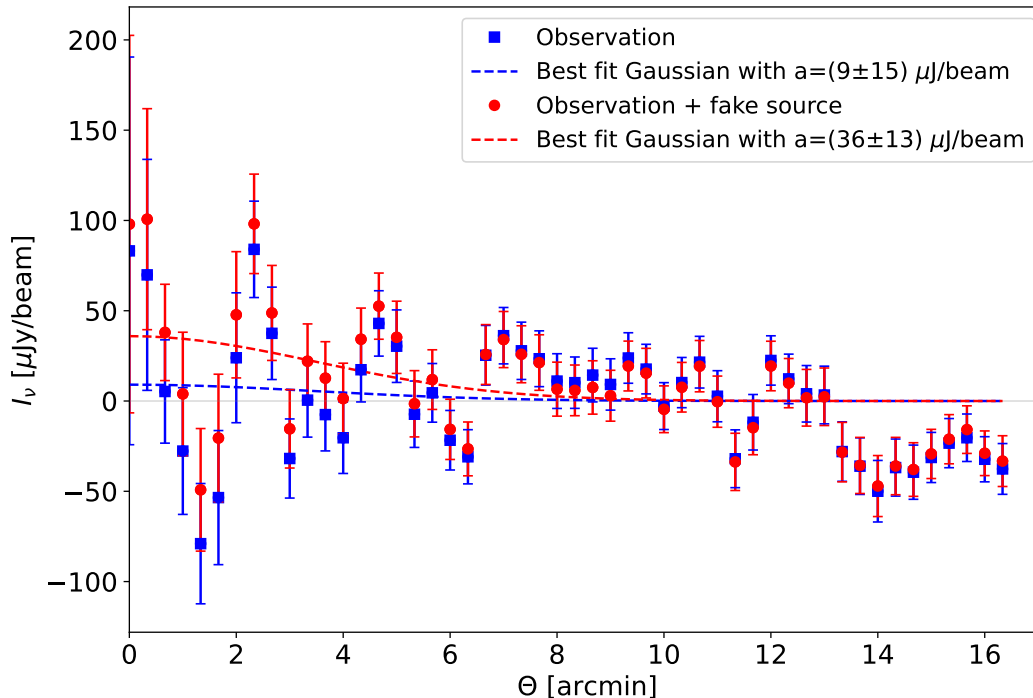


Figure 4.1: Radial intensity profiles for Canes Venatici I. Data points show the mean intensity in $20''$ wide annuli, with the error bars showing the standard deviation of the mean. Blue data points are for purely observational data, and red data points are for the same data with an additional 20 mJy fake source. Dashed lines show the best-fitting Gaussians with a fixed FWHM of r_\star equivalent to 8.2 .

4 WIMP limits from LOFAR observations of dwarf spheroidal galaxies

Table 4.2: Gaussian amplitude $a_{\text{Gauss, obs}}$ for purely observed data and amplitude $a_{\text{Gauss, inj}}$ for data with an additional injected fake source. S_{FS} is the fake source flux density, and FWHM is the width of the Gaussian, here assumed to be equivalent to r_* .

dSph	$S_{\text{FS}, 2\sigma}$ [mJy]	$a_{\text{Gauss, obs}}$ [$\mu\text{Jy beam}^{-1}$]	$a_{\text{Gauss, inj}}$ [$\mu\text{Jy beam}^{-1}$]	FWHM [arcmin]
CVnI	20	9 ± 15	36 ± 13	8.2
UMaI	35	-6 ± 10	24 ± 11	11.3
UMaII	35	-1.1 ± 4.8	12.9 ± 4.8	16.0
UMi	33	9.1 ± 9.6	28.9 ± 9.0	8.3
Will	5	-55 ± 42	17 ± 39	1.8
CVnII	1	16 ± 28	50 ± 29	1.6

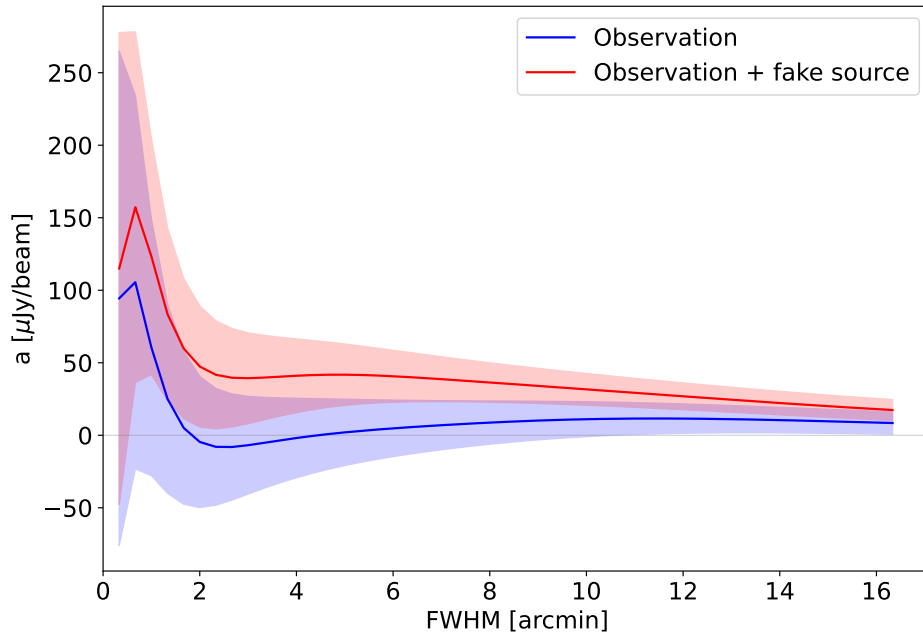


Figure 4.2: Best-fitting Gaussian amplitudes for the radial intensity profiles of Canes Venatici I with Gaussians of varying FWHMs. The solid blue line is for purely observational data, and the solid red line the same data with an additional 20 mJy fake source. Shaded areas indicate 1σ confidence intervals.

Fluctuations that cannot be described by Gaussian statistics can affect the fit of galaxies with small half-light radii as the number of data points is small and any fluctuation may not average out. This is in particular the case for Will ($r_* = 110''$) and CVnII ($r_* = 95''$). For Will, a negative Gaussian amplitude for the fit to the purely observational data is found. This is the only galaxy with a "signal," but because it is negative, it can be ruled out as DM-related. For CVnII, the Gaussian amplitude is compatible with zero, albeit with a large uncertainty. We tried to mitigate the limitation due to the small number of data points by increasing the region in which radial profiles were measured

to $3r_\star$ and $4r_\star$ for Will and CVnII, respectively.

Since the size of the DM halo is uncertain, we varied the FWHM of the Gaussian fit to the radial intensity profiles. Here, we wanted to investigate the possible systematic uncertainty of the assumption that the FWHM of the signal produced by the DM halo is equal to the stellar radius, r_\star , which itself has an uncertainty of around 10 to 15% (Geringer-Sameth et al. 2015). For CVnI, the corresponding results are shown in Fig. 4.2. The data are in agreement with zero within the 1σ confidence intervals for almost the entire range of FWHM. On the other hand, the 2σ detection of the injected source over a wide range of FWHM is also evident. Only at small FWHM, statistical fluctuations start to suppress the significance of the detection. Signals on that scale are most likely due to fluctuations in the map and not related to DM.

The next step was to calculate the diffusion and energy-loss timescales. This identified the diffusion regime that then lead to the set of equations needed to estimate limits on the annihilation cross section. For the INT scenario, the diffusion timescale for CVnI is ≈ 30 Myr, whereas the energy-loss timescale is ≈ 110 Myr. Since both timescales are on the same order of magnitude, we used diffusion regime *B* with Eq. (4.14) to calculate the limits on the WIMP annihilation cross section. We sum-

Table 4.3: Timescales of CR diffusion and loss for every model scenario with a benchmark CR energy of 10 GeV. The resulting diffusion regime is also noted.

dSph	Model scenario	τ_{diff} [Myr]	τ_{loss} [Myr]	Regime
CVnI	OPT	288	11.4	<i>A</i>
	INT	28.8	113	<i>B</i>
	PES	0.288	124	<i>C</i>
UMaI	OPT	92.1	11.4	<i>A</i>
	INT	9.21	113	<i>C</i>
	PES	0.0921	124	<i>C</i>
UMaII	OPT	20.1	11.4	<i>B</i>
	INT	2.01	113	<i>C</i>
	PES	0.0201	124	<i>C</i>
UMi	OPT	29.7	11.4	<i>B</i>
	INT	2.97	113	<i>C</i>
	PES	0.0297	124	<i>C</i>
Will	OPT	0.399	11.4	<i>C</i>
	INT	0.0399	113	<i>C</i>
	PES	0.000399	124	<i>C</i>
CVnII	OPT	4.96	11.4	<i>B</i>
	INT	0.496	113	<i>C</i>
	PES	0.00496	124	<i>C</i>

4 WIMP limits from LOFAR observations of dwarf spheroidal galaxies

marize the diffusion and energy-loss timescales together with the resulting diffusion regimes for the three model scenarios for our six dSph galaxies in Table 4.3. We note that both timescales depend on the CR energy. We used a benchmark-energy of $E = 10$ GeV; a different CR energy may change the choice of diffusion regimes and hence slightly affect the limits.

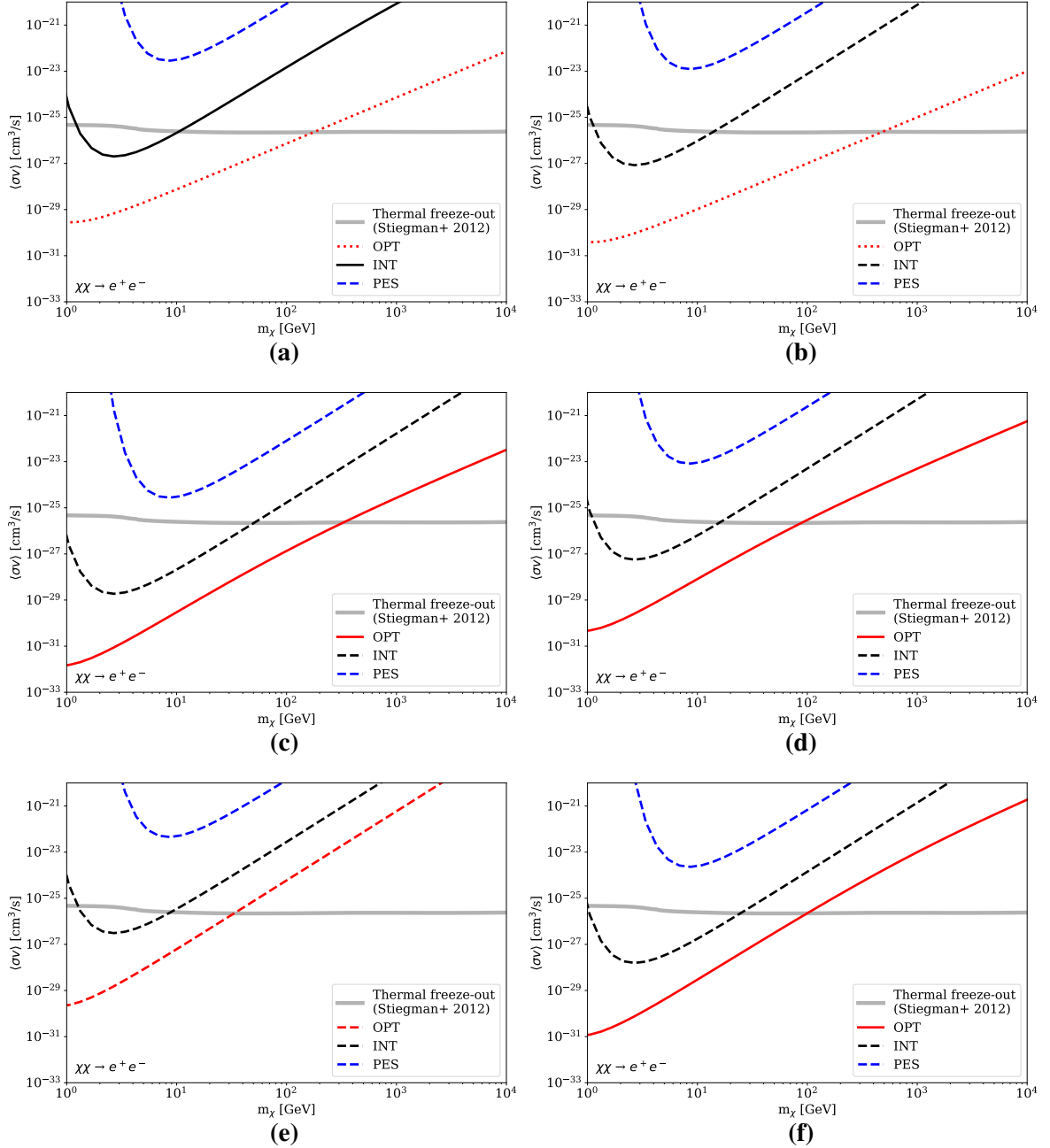


Figure 4.3: Individual upper limits on the WIMP annihilation cross section for the OPT, INT, and PES model scenarios. Line colors represent the assumed model scenario: red for OPT, black for INT, and blue for PES. Line styles represent the assumed diffusion regime: dashed lines for regime A, solid lines for regime B, and dotted lines for regime C. Panel (a) shows CVnI, (b) UMaI, (c) UMaII, (d) UMi, (e) Will, and (f) CVnII. The gray line represents the lower limit from the thermal freeze-out (Stiegman et al. 2012).

In Fig. 4.3 we present the upper limits to the WIMP annihilation cross section from each individual galaxy. For comparison, we additionally plot the lower limit on the annihilation cross section calculated from the thermal WIMP freeze-out mechanism by Steigman et al. (2012).

4.4.2 Stacked limits

The stacked radial intensity profiles both for profile and image stacking are shown in Fig. 4.4. The best-fitting Gaussian amplitudes are $a_{\text{obs, profiles}} = (0.3 \pm 4.3) \mu\text{Jy beam}^{-1}$ and $a_{\text{obs, images}} = (-1.8 \pm 2.9) \mu\text{Jy beam}^{-1}$ for the purely observed data using profile and image stacking, respectively. In both stacking strategies, the amplitudes are consistent with zero so the stacking does not reveal any additional signal. We varied the FWHM of fitted Gaussians as before for the individual galaxies. Again, the observed amplitudes are consistent with zero as shown in Fig. 4.5.

The flux density of the injected fake sources from the individual galaxies was divided by a factor to determine how much fainter is the signal that can be detected by stacking. The factor was chosen to achieve a 2σ detection, it equals 1.8 for profile stacking and 2.8 for image stacking. We again fitted Gaussians to the resulting stacked radial profile and the Gaussian amplitudes are $a_{\text{inj, profiles}} = (9.4 \pm 4.5) \mu\text{Jy beam}^{-1}$ for profile stacking and $a_{\text{inj, images}} = (6.6 \pm 2.8) \mu\text{Jy beam}^{-1}$ for image stacking, showing that we have detected the fake source at 2σ confidence.

Upper limits for the WIMP annihilation cross section were calculated from the best-fitting amplitudes of the radial profiles obtained with either method. A unique value of amplitude a was used and the other terms in Eq. (4.17) were given as an average value for all galaxies. This average was calculated using the same approximation regime as for the individual galaxies (Table 4.3). The resulting upper limits for the cross section from both approaches are shown in Fig. 4.6, together with the average of the limits obtained for the individual galaxies.

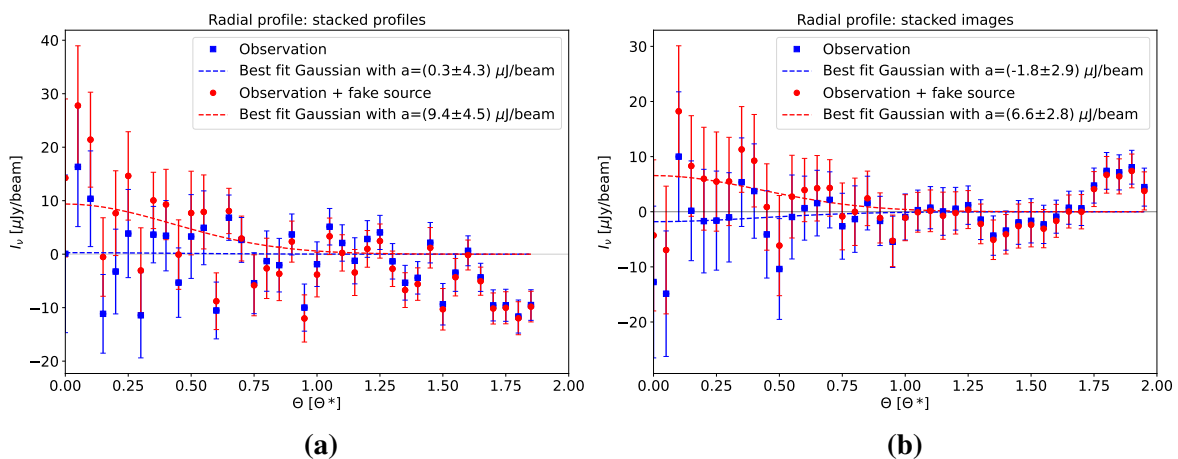


Figure 4.4: Stacked radial intensity profiles. Panel (a) shows profile stacking and panel (b) image stacking. Data points show the mean intensity in adjacent annuli, with the error bars showing the standard deviation of the mean. Blue data points are for purely observational data, and red data points are for the same data with an additional fake source. Dashed lines show the best-fitting Gaussians with a fixed FWHM of r_\star . The radius is expressed as an apparent angle, θ , scaled to the apparent size of the stellar radius, $\theta_\star = r_\star/d$.

4 WIMP limits from LOFAR observations of dwarf spheroidal galaxies

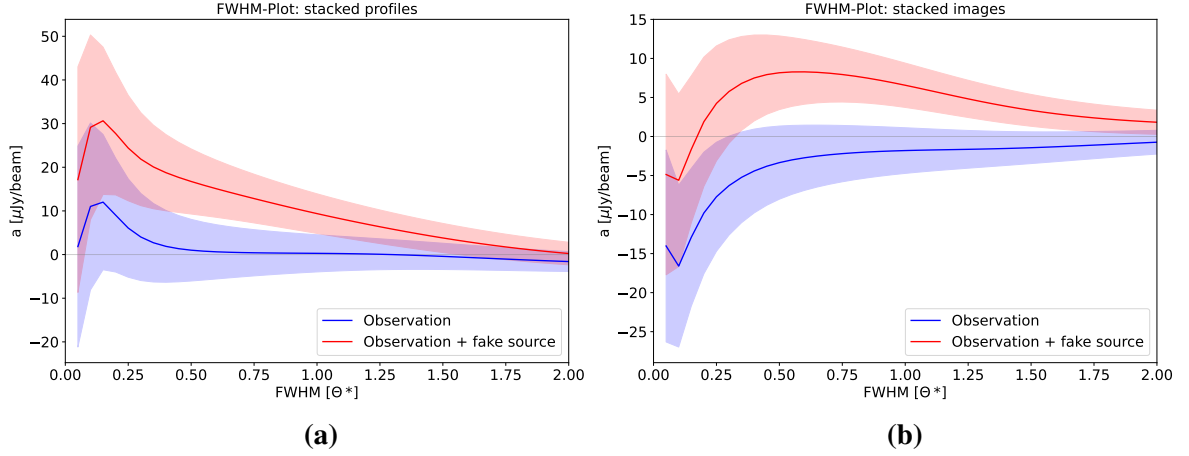


Figure 4.5: Best-fitting Gaussian amplitudes for the stacked radial intensity profiles. Panel (a) shows profile stacking and panel (b) image stacking. Solid blue lines show the purely observational data, whereas solid red lines show the same data with an additional fake source. Shaded areas indicate 1σ uncertainties. The FWHM of the Gaussian is expressed as the apparent size of the stellar radius, $\theta_\star = r_\star/d$.

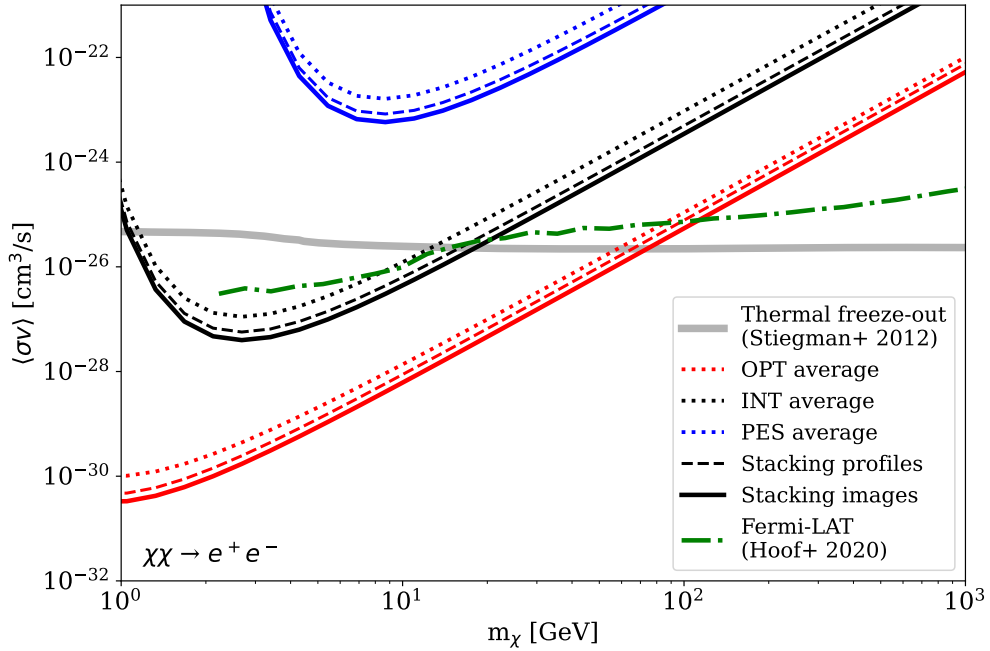


Figure 4.6: Upper limits on the WIMP annihilation cross section from stacking. Dotted lines are the averaged individual limits, dashed lines are limits obtained by stacking radial profiles, and solid lines are limits obtained by stacking galaxy images. Red, black, and blue correspond to the OPT, INT, and PES model scenarios, respectively. The thermal freeze-out cross section (Stiegman et al. 2012, gray) and upper limits from *Fermi*-LAT γ -ray observations (Hoof et al. 2020, green) are shown for comparison.

4.4.3 Systematic uncertainties

There are several sources of inaccuracies in the obtained limits. The most significant are the assumptions on the values of the average magnetic field strength and diffusion coefficient. For this reason

we used our three different model scenarios in order to illustrate the influence of these parameters. The differences between the cross-section limits in each scenario are indeed two to three orders of magnitude showing the large uncertainty resulting from the inaccuracy of these input parameters.

For our INT scenario we assumed that the diffusion coefficient is $10^{27} \text{ cm}^2\text{s}^{-1}$ as measured both in dwarf irregular galaxies (Murphy et al. 2012) and in the Milky Way (Korsmeier & Cuoco 2016). However, it is also possible that the true value may be closer to $10^{28} \text{ cm}^2\text{s}^{-1}$ as found in late-type spiral galaxies (Heesen et al. 2019) or even $10^{29} \text{ cm}^2\text{s}^{-1}$ such as for the halos in edge-on spiral galaxies. On the other hand, the true value can also go down to the value of $10^{26} \text{ cm}^2\text{s}^{-1}$ measured in dwarf irregular galaxies (Heesen et al. 2018). The magnetic field is much more uncertain but values range between $0.1 \mu\text{G}$ and $10 \mu\text{G}$ assuming that the magnetic energy density is in equipartition with the CR energy density within two orders of magnitude. We note that this is only a heuristic argument though as there are no stringent physical reasons why there should be equipartition. Generally, the diffusion coefficient depends on the magnetic field (Sigl 2017), but to simplify our model we treated them independently and this is an additional source of uncertainty.

A further uncertainty is introduced by the adopted NFW profile parameters r_s and ρ_s . While including full posterior probability-distribution functions (PDFs) of existing Bayesian fits in the literature (e.g., Ando et al. 2020) would be more appropriate, it would also be impractical. This is because of the overwhelming magnetic-field uncertainties, which would not be reduced by considering such PDFs. Therefore, we contend ourselves by using the best-fit values for r_s and ρ_s as derived in (Geringer-Sameth et al. 2015), and direct our attention to the CR propagation parameters (e.g., magnetic field) when discussing uncertainties.

Another source of uncertainty comes from the approximations made in the spectral function where we chose one of the diffusion regimes (A , B , or C) and used the appropriate equation (Eq. 4.13, 4.14, or 4.14). The regime was chosen by comparing the diffusion and energy-loss timescales (Table 4.3). The diffusion timescale depends on the diffusion coefficient, D_0 , and the energy-loss timescale depends on the average magnetic field, B . For this reason, regimes were chosen independently for each model scenario. An inappropriate choice of the approximation regime for certain ratio of timescales affects the cross-section limits much less than the previously mentioned uncertainty from the model parameters (D_0 , B). There is ongoing work to solve the transport equations regardless of the ratio of timescales (Vollmann et al. 2024), which would completely eliminate such uncertainties.

There is some evidence for tidal disruption or nonequilibrium kinematics in Will (Ibata et al. 1997; Willman et al. 2011; Geringer-Sameth et al. 2015), which could cause the NFW profile parameters to be biased to higher masses. Since that bias might artificially improve our stacked limits, we repeated the stacked analysis without Will but with the same injected source intensity for other galaxies (see Appendix H). We find that the resulting limits without Will are stronger compared to the limits including all the galaxies. In the end, we decided to keep the weaker limits derived from all galaxies as the more conservative estimate.

We also mention other sources of uncertainty that are small compared to the model scenario uncertainty. First, we assumed that the density distribution in dSph galaxies is described by a NFW density profile. This is just one of the possibilities and alternative profiles (e.g., Einasto & Haud 1989; Burkert 1995) could also be used (Vollmann 2021). Second, we assumed a power-law dependence of the diffusion coefficient on the CR energy (Eq. 4.6) and Kolmogorov turbulence. If we are able to better constrain the magnetic field and diffusion coefficient in dSph galaxies, the mentioned uncertainties would become more important.

4 WIMP limits from LOFAR observations of dwarf spheroidal galaxies

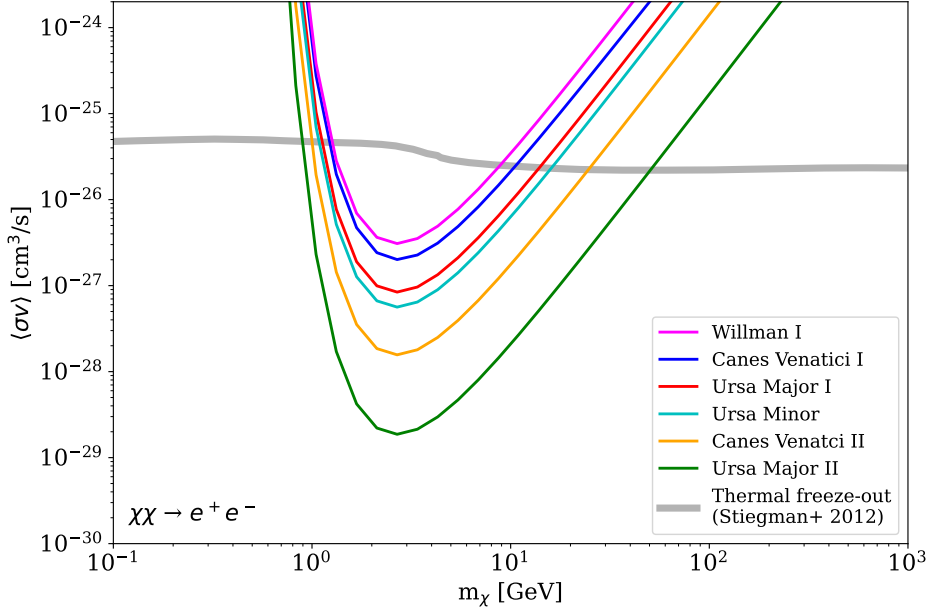


Figure 4.7: Individual upper limits on the WIMP annihilation cross section for the dSph galaxies in our sample for the INT model scenario.

4.5 Discussion and conclusions

We first compared the limits for the INT model scenario from individual galaxies in Fig. 4.7. The individual limits within our sample vary due to the different noise levels of the LoTSS maps and the different intrinsic properties, such as the DM density profile and distance. The best constraints on the annihilation cross section are derived from UMaII. This is also true for γ -ray WIMP searches since this galaxy has the highest J factor (Hoof et al. 2020). The next best constraints are derived from CVnII. This is counterintuitive since UMaII has the largest apparent size ($r_\star \approx 16'$), whereas CVnII is the smallest ($r_\star \approx 1.6'$). But reviewing the halo factor defined in Eq. (4.11), it becomes evident that the apparent size is not the most important parameter; the most important are instead the characteristic density, ρ_s , the scale length, r_s , and the half-light radius, r_\star . According to Eq. (4.11), the combination of these parameters is high for UMaII and CVnII, which explains the strong limits for these two galaxies. The same explanation justifies why the limits set by Will and CVnI are less stringent than average: Will has the lowest scale length within our set of galaxies², and CVnI has the smallest characteristic density. Since the halo factor depends on the square of both values, this factor is smaller than average, and hence the limits are less stringent.

We improved the limits by stacking the data for different galaxies. To test the improvement, we compared the stacked limits to the average value of all individual limits (Fig. 4.6). The stacking of profiles lowered the limits by a factor of approximately two and the stacking of images by three. This is expected because with stacking we are effectively extending the observing time. The image stacking yields better results than the stacking of profiles, but controlling the uncertainties is more difficult. We only compared the two specific stacking strategies, but in general there are many alternative ways of combining the results of different galaxies. For example, in a future study a more statistically rigorous

²The spectral factor $X(\nu)$ for Will is two orders of magnitude smaller than average, which justifies the moderate limit for this galaxy as well.

approach could be to treat galaxies independently with their own nuisance parameters while the DM model parameters are fitted simultaneously (see, e.g., Hoof et al. 2020).

The comparison of our stacking limits with other attempts to constrain the WIMP annihilation cross section, such as the thermal freeze-out cross section by Steigman et al. (2012) or dSph galaxy observations by *Fermi*–LAT (Hoof et al. 2020), shows the competitiveness of our results. Our cross-section limits from the INT scenario already exclude thermal WIMPs with masses below 20 GeV. In the OPT scenario we can even exclude thermal WIMPs with masses below 70 GeV. While the PES limits do not exclude thermal WIMPs in any mass range, they still prove the validity of our concept (Vollmann et al. 2020; Regis et al. 2014).

As is customary, we assumed a smooth DM distribution. However, there has been recent work stating that DM halos contain prompt cusps (Delos & White 2023) that would boost the annihilation signal, which, in turn, would lower our limits by up to two orders of magnitude. The same effect would apply to limits inferred from γ -ray excess in the Milky Way and other galaxies.

To date, the results from γ -ray observations of dSph galaxies presented by Hoof et al. (2020) are among the strongest limits on the WIMP annihilation cross section. In the mass range below 20 GeV, our INT limits are stronger than those from *Fermi*–LAT. Our limits are valid under the assumption of the average magnetic field and diffusion coefficient in dSph galaxies and therefore have a large uncertainty. However, our results show that radio observations of dSph galaxies can potentially constrain the WIMP annihilation cross section if one accepts this premise. This method is especially powerful for WIMP masses below 10 GeV.

Considering the observational resources needed for both attempts, our method is much more efficient. We only used LoTSS-DR2 survey data (Shimwell et al. 2022, about 50 h in total for the six dSph galaxies) and have not performed targeted observations. For comparison, Ackermann et al. (2015) used six years of *Fermi*–LAT data. Compared to these observations, we achieve better limits at lower masses in the OPT scenario and comparable limits in the INT scenario. Hence, the advantages of our study are the sensitivity in the low-mass regime and the efficiency in terms of observation time. The biggest drawbacks of using radio continuum observations are of course the uncertainties related to the strength of the magnetic field and the value of the diffusion coefficient. The field strength of dSph galaxies could be measured from a grid of Faraday rotation measures of polarized background sources with a sensitive radio telescope, such as the Square Kilometre Array (SKA; Johnston-Hollitt et al. 2015).

In addition to the HBA used for LoTSS, LOFAR low band antenna observations (de Gasperin et al. 2021) would improve the limits on the lower mass end because the critical frequency of synchrotron radiation depends on the square of the WIMP mass (Rybicki & Lightman 1986). The SKA has also been suggested as a promising future instrument for DM searches (Colafrancesco et al. 2015).

Acknowledgements

We thank the anonymous referee for a constructive report which helped to improve the paper. This work is funded by the Deutsche Forschungsgemeinschaft (DFG, German Research Foundation) under Germany’s Excellence Strategy – EXC-2121 “Quantum Universe” – 390833306. LOFAR (van Haarlem et al. 2013) is the Low Frequency Array designed and constructed by ASTRON. It has observing, data processing, and data storage facilities in several countries, which are owned by various parties (each with their own funding sources), and that are collectively operated by the ILT foundation under a joint scientific policy. The ILT resources have benefited from the following recent major funding sources: CNRS-INSU, Observatoire de Paris and Université d’Orléans, France; BMBF, MIWF-NRW, MPG, Germany; Science Foundation Ireland (SFI), Department of Business, Enterprise and Innovation (DBEI), Ireland; NWO, The Netherlands; The Science and

4 WIMP limits from LOFAR observations of dwarf spheroidal galaxies

Technology Facilities Council, UK; Ministry of Science and Higher Education, Poland; The Istituto Nazionale di Astrofisica (INAF), Italy. This research made use of the Dutch national e-infrastructure with support of the SURF Cooperative (e-infra 180169) and the LOFAR e-infra group. The Jülich LOFAR Long Term Archive and the German LOFAR network are both coordinated and operated by the Jülich Supercomputing Centre (JSC), and computing resources on the supercomputer JUWELS at JSC were provided by the Gauss Centre for Supercomputing e.V. (grant CHTB00) through the John von Neumann Institute for Computing (NIC). This research made use of the University of Hertfordshire high-performance computing facility and the LOFAR-UK computing facility located at the University of Hertfordshire and supported by STFC [ST/P000096/1], and of the Italian LOFAR IT computing infrastructure supported and operated by INAF, and by the Physics Department of Turin university (under an agreement with Consorzio Interuniversitario per la Fisica Spaziale) at the C3S Supercomputing Centre, Italy. DJB acknowledges funding from the German Science Foundation DFG, via the Collaborative Research Center SFB1491 "Cosmic Interacting Matters - From Source to Signal".

5 Conclusion and Outlook

In this thesis, I showed how low-frequency radio observations can be utilized to investigate some of the largest unknowns in galaxy formation and evolution, namely the workings of star formation and the nature of dark matter. To this end, we first investigated the limitations of radio continuum emission as an extinction-free star formation tracer; indeed, we expect a suppression at low frequencies due to the combined effects of free–free absorption and ionisation losses of the cosmic ray electrons. The low-frequency flattening of radio emission was observed in the galaxy M 51 where it is caused by a combination of ionisation losses and free–free absorption as well as in the H II regions of the galaxy M 101 where it is caused by free–free absorption. In the second part, LOFAR radio observations of dwarf spheroidal galaxies were used to put new stringent limits on WIMPs as a dark matter candidate.

After introducing the basic astrophysical and observational concepts for both parts in Ch. 1, I present the radio spectral study of M 51 in Ch. 2. The analysis is based on high resolution observations in eight different frequency bands between 54 and 8350 MHz and it reveals a spectral flattening below 100 MHz which is observed for the first time in an average external spiral galaxy. The turnover is at slightly higher frequencies in the spiral arms compared to the inter-arm regions. This is what we expect as the ionised gas is more concentrated in the spiral arms leading to higher values of EM that translate into higher turn-over frequencies. However, the EM difference is not statistically significant. The processes expected to cause the flattening is free–free absorption which would correlate with the ionised medium in the galaxy. However, we did not find a spatial correlation between the EM calculated from the radio turnover and the EM estimated from the H α observations. Instead we found a weak correlation between the spectral curvature and the neutral hydrogen (H I) mass surface density. This implies that free–free absorption, while its influence can not be ruled out conclusively, is not the sole process responsible for the low-frequency spectral flattening. We can therefore conclude that ionisation losses, which are dominant in the neutral medium, must also play an important role. This answers the first of the scientific questions: the very low-frequency emission in spiral galaxies is suppressed because of CR ionisation losses and affected by free–free absorption. Their effects need to be taken into account if we are to use sub-gigahertz radio continuum observations to study star formation in galaxies.

In Ch. 3, I extend this work to search specifically for the effects of free–free absorption in the giant H II regions of the nearby spiral galaxy M 101. New high-resolution radio continuum maps at 54 and 1370 MHz are presented and analysed together with ancillary maps at 144 and 4850 MHz. Out of the six selected H II regions, we observe a low-frequency flattening in five of them; we find even hints of spectral turnover, not just a flattening, something that requires absorption effects. This flattening can be well fitted with the free–free absorption model producing reasonable EM values that are in approximate agreement with those as measured from optical H α observations. The low-frequency flattening can only be detected in the very centre of the giant H II regions so its detection requires observations at high angular resolution. The second science question is now answered: the radio emission in giant H II regions shows low-frequency flattening in the very centre of the region, caused by free–free absorption.

The third scientific question is answered in both Ch. 2 and 3. Radio observations below 100 MHz cannot be used as a star formation tracer unless we thoroughly understand the effects causing the low-

5 Conclusion and Outlook

frequency spectral flattening, especially in the H II regions. Special care is needed even when using frequencies around 150 MHz (LOFAR HBA) as an SFR tracer because they could be affected by free–free absorption and ionisation losses in some parts of the galaxies.

A different topic is studied in Ch. 4; the WIMPs as a dark matter candidate. I used 144 MHz LOFAR observations of six nearby dwarf spheroidal galaxies to put limits on the WIMP self-annihilation cross-section. No dark matter signal was detected but I obtained limits that are presented in Fig. 4.6. The limits strongly depend on the assumption of the magnetic field and diffusion coefficient so we present three scenarios: optimistic, intermediate and pessimistic. Comparing our limits to the thermal relic cross-section we can exclude thermal WIMPs with masses below 20 GeV in the intermediate scenario and thermal WIMPs with masses below 70 GeV in the optimistic scenario. In the mass range below 20 GeV, our intermediate limits are stronger than those from *Fermi*–LAT (Hoof et al. 2020). Our limits suffer from higher uncertainties but they can be obtained after a significantly shorter observation time. The fourth and final scientific question is now partially answered: it is still not known if WIMPs are dark matter but I successfully used radio observations to put limits on this scenario.

All of the science in the thesis is based on the same underlying process, cosmic ray electrons producing synchrotron emission in the magnetic fields of galaxies. The behaviour of CRes is explained by the diffusion-loss equation which connects diffusion, energy loss and injection. The standard scenario is that CRes are injected in supernova explosions, they diffuse in the galaxy and lose energy due to IC losses and synchrotron emission, which is observed in the radio band. In this thesis, deviations from this standard scenario are studied. In the study of M 51, I showed that an additional ionisation energy loss term becomes relevant for lower energy CRes in neutral ISM. Very low-frequency radio emission is absorbed due to free–free interactions in the ionised medium causing the radio emission we observe to be diminished. This is especially relevant in H II regions. In the DM study, the injection in supernova explosions is not happening because dwarf spheroidal galaxies have very low star formation, the CRes are instead injected in DM annihilation. The rest of the process is the same and that allows us to calculate the limits on DM annihilation from the non-detection of radio emission.

Ultra low-frequency radio observations were necessary to reach the scientific conclusions in this thesis. The low-frequency turnover in spiral galaxies happens below 100 MHz so we needed the LOFAR LBA observations at 54 MHz to detect it. The high resolution of the observations made it possible to test spatial correlations and focus on small H II regions. Searching for WIMPs at low frequencies makes it possible to constrain low mass WIMPs in an observationally efficient way. The LOFAR telescope was crucial for this work because it is the only instrument that can observe at such low frequencies with high resolution and sensitivity.

5.1 Future prospects

The opportunities for future discoveries run on two parallel but interconnected tracks: theory and observations.

From the theory point of view, the most notable open question about the low-frequency flattening is a spectral model for ionisation losses. We now know that ionisation losses play an important role in the flattening but a specific model for the shape of the spectrum does not exist as such. This model would allow us to determine the relative importance of ionisation losses compared to the free–free absorption. Isolating the effects of free–free absorption would make it possible to calculate the EM with certainty and provide information about the ionisation and distribution of the ISM.

Significant theoretical advancements on radio DM searches have already been achieved since the work in Ch. 4 was published. The diffusion loss equation was solved exactly for dwarf spheroidal

galaxies and we developed a new computational tool to calculate DM limits from observations and expected signal from dwarf galaxies. This Python tool is published under the title `diffSph` (Vollmann et al. 2024). A large number of WIMP annihilation and decay channels as well as different DM profiles are available, not just the e^+e^- channel and NFW profile that we were limited to in this thesis. This will significantly broaden the future WIMP limits from radio observations and make them easier to calculate. Further work is also required to reduce the uncertainties from the assumptions on the magnetic field in dSph. The magnetic field in dSph could be calculated by considering the star formation history and the decay of magnetic field after the star-formation activity. An alternative approach was proposed by Regis et al. (2023), in which the CR electrons and positrons themselves generate irregularities in the magnetic field which results in WIMP limits independent on the magnetic field.

In general, further observations will always improve and substantiate results in astrophysics. Following are the specific observational results that would be the most valuable as a follow up to this thesis. First, we would need at least one M 101 radio map at frequencies between 150 and 5000 MHz with reliable large scale emission. This would make it possible to test the conclusions from the M 51 work on another galaxy and at the same time substantiate the results from the H II observations. M 101 has actually been observed with the GMRT, but the data has not been properly processed due to the difficulty imposed by the large angular size of the galaxy. Second, to get better limits on the WIMP cross-section, it would be the best to perform deeper observations on a single dSph. This would avoid the stacking uncertainty. The best single galaxy would be Ursa Minor because it has a high dark matter density, it is not tidally disturbed and has a large enough angular size.

To make these observations reality, we should consider the current and future radio telescopes capable of performing them. The LOFAR telescope was the most important for the work on this thesis and it will be even more valuable in the future because of its currently ongoing LOFAR2.0¹ update. The update will triple the processing power at each station and enable simultaneous HBA and LBA observations. LOFAR2.0 long term programs are under evaluation, including a dedicated dark matter search program; the LOFAR2.0 Dark Matter eXperiment (LoDMaX). LoDMaX is proposing 6000 h of observations which include hundreds of hours on dSph in order to reach the confusion limit. The point source removal will also be significantly improved by using the international stations that produce sub-arcsecond resolution. The results from Ch. 4 and my experience on this topic was invaluable in planning the LoDMaX continuum searches.

The Square Kilometre Array (SKA) is a new low-frequency facility currently being built on the Southern hemisphere. It will consist of 131,072 smaller SKA-low three-like antennas to cover the frequency range from 50 to 350 MHz and 197 SKA-mid dish antennas to cover the frequency range 350 MHz to 14 GHz. However, LOFAR will remain uniquely important for studying the very low frequencies because it is the only instrument capable of achieving sub-arcsecond resolution at frequencies below 100 MHz with international stations.

¹https://www.lofar.eu/wp-content/uploads/2023/04/LOFAR2_0_White_Paper_v2023.1.pdf

5 Conclusion and Outlook

6 Acknowledgments

The last three and a half years were so much different than I could have expected. It was not easy moving to a new country by myself and committing to doing a PhD, but it was worth it. Not only for everything I learned, but also for all the experiences I had and people I met. Here, I would like to thank all of those people.

First, I would like to thank my wonderful supervisors Marcus and Francesco. Marcus was always there to answer questions, give guidance in difficult moments and his easy-going attitude made me feel like I can do anything. I am seriously impressed by how much motivation I had after each of our meetings. Francesco helped me so much with his expertise, practical advice and productive discussions in meetings.

Next, I am enormously grateful for all the help from Volker in writing papers, analysing data and discussion results. I often think he should get a monument for how much he helped me over the years.

Thank you to Robi Banerjee, Dieter Horns, and Joe Liske for being part of the examination committee of my doctoral defence.

A big thank you goes to my family. Even when we were far away from each other, I always knew you supported me in everything I do. I am thankful to my mom, for believing in me, the relaxing moments we had and her advice. I am thankful to my dad, for his support, kindness and for offering me a new perspective for many things in life. Thank you to my brother Juraj, for being someone I can rely on and relax with. Veliko hvala mom bratu Dominiku, za zabavne igre i puno ljubavi. Jako sam ponosna na to koliko je narastao i odrastao u zadnjih par godina. Thank you to Marina, for many kind words and her gentle view towards everybody. Thank you to my grandpas, my uncles and the whole family Radovčić.

The biggest support for me were my Croatian friends, who I am eternally grateful for. The Frogs: Barbara, Fran, Karaula, Tin, and Žugi, thank you for all the fun times, work discords, stupid jokes and random video game streams. The Shag: Barbara, Dora, Eva, and Mia, thank you for being there for me, for all the rants, declarations of love, personal conversations and spilled tea. Thank you to Mia and Šuša for being the best hosts, see you in Amsterdam soon! Barbara, I have to mention you for the third time, thank you for our wonderful friendship and for all the academic and personal support.

I am grateful to the Observatory community for being very friendly, inclusive and for always rooting for one another. I will miss this beautiful place and all the fun social activities that we organised. Thank you Angelina, Antonio, David, Deepali, Dragana, Gabriella, Giulia, Henrik, Jan-Erik, Jörg, Nicolas, Marco, Martin, Philipp, Pia, Thomas, Thorben, Tobi, Victor and everybody else for this wonderful work environment.

Thank you to all my swordfighting and archery friends from Hammaborg. You understand that sometimes after a hard week, you just need to hit stuff with a sword. Thank you Marcel and Vadim, for being pleasant people to live with and making my life in Hamburg much less lonely.

I am very grateful to all my collaborators for believing in my work and for their contributions to the published papers, especially Aritra Basu, Björn Adebahr, Martin Vollmann, Finn Welzmüller, and Dominik Bomans. I am very honoured to be a part of the nearby galaxies group of the LOFAR MKSP, the support and friendly discussions in our meetings are a great example of how scientific collaboration should look like.

6 Acknowledgments

7 Bibliography

- Abdelhameed, A. H., Angloher, G., Bauer, P., et al. 2019, *Phys. Rev. D*, 100, 102002
- Abdo, A. A., Ackermann, M., Ajello, M., et al. 2010, *JCAP*, 2010, 014
- Abramowski, A., Acero, F., Aharonian, F., et al. 2011, *Phys. Rev. Lett.*, 106, 161301
- Ackermann, M., Ajello, M., Allafort, A., et al. 2012, *Phys. Rev. Lett.*, 108, 011103
- Ackermann, M., Albert, A., Anderson, B., et al. 2015, *Phys. Rev. Lett.*, 115, 231301
- Acosta-Pulido, J. A., Agudo, I., Alberdi, A., et al. 2015, arXiv e-prints, arXiv:1506.03474
- Adams, E. A. K., Adebahr, B., Connor, L., et al. 2020, in *American Astronomical Society Meeting Abstracts*, Vol. 235, American Astronomical Society Meeting Abstracts #235, 136.07
- Adams, E. A. K., Adebahr, B., de Blok, W. J. G., et al. 2022, *A&A*, 667, A38
- Adebahr, B., Krause, M., Klein, U., Heald, G., & Dettmar, R. J. 2017, *A&A*, 608, A29
- Adebahr, B., Krause, M., Klein, U., et al. 2013, *A&A*, 555, A23
- Adriani, O., Barbarino, G. C., Bazilevskaya, G. A., et al. 2009, *Nature*, 458, 607
- Aghanim, N., Akrami, Y., Ashdown, M., et al. 2020, *A&A*, 641, A6
- Aguilar, M., Alberti, G., Alpat, B., et al. 2013, *Phys. Rev. Lett.*, 110, 141102
- Aharonian, F., Akhperjanian, A., Bazer-Bachi, A., et al. 2008, *Astroparticle Physics*, 29, 55
- Alcock, C., Allsman, R. A., Alves, D. R., et al. 2000, *ApJ*, 542, 281–307
- Alloin, D., Collin-Souffrin, S., Joly, M., & Vigroux, L. 1979, *A&A*, 78, 200
- Anantharamaiah, K. R., Viallefond, F., Mohan, N. R., Goss, W. M., & Zhao, J. H. 2000, *ApJ*, 537, 613
- Ando, S., Geringer-Sameth, A., Hiroshima, N., et al. 2020, *Physical Review D*, 102
- Aprile, E., Aalbers, J., Agostini, F., et al. 2017, *Physical Review Letters*, 119
- Baars, J. W. M., Genzel, R., Pauliny-Toth, I. I. K., & Witzel, A. 1977, *A&A*, 61, 99
- Balazs, C., Bringmann, T., Kahlhoefer, F., & White, M. 2024, arXiv e-prints, arXiv:2411.05062
- Basu, A., Beck, R., Schmidt, P., & Roy, S. 2015, *MNRAS*, 449, 3879
- Basu, A., Mitra, D., Wadadekar, Y., & Ishwara-Chandra, C. H. 2012, *MNRAS*, 419, 1136

7 Bibliography

- Basu, A., Mitra, D., Wadadekar, Y., & Ishwara-Chandra, C. H. 2012, MNRAS, 419, 1136
- Basu, A., Roychowdhury, S., Heesen, V., et al. 2017, MNRAS, 471, 337
- Beck, R. 2015, A&A Rev., 24, 4
- Beck, R., Brandenburg, A., Moss, D., Shukurov, A., & Sokoloff, D. 1996, Ann. Rev. A&A, 34, 155
- Beck, R. & Krause, M. 2005, Astronomische Nachrichten, 326, 414
- Beck, R., Poezd, A. D., Shukurov, A., & Sokoloff, D. D. 1994, A&A, 289, 94
- Beck, R. & Wielebinski, R. 2013, Magnetic Fields in Galaxies, ed. T. D. Oswalt & G. Gilmore, Vol. 5, 641
- Bendo, G. J., Joseph, R. D., Wells, M., et al. 2002, AJ, 124, 1380
- Berkhuijsen, E. M., Urbanik, M., Beck, R., & Han, J. L. 2016, A&A, 588, A114
- Bertone, G., Cirelli, M., Strumia, A., & Taoso, M. 2009, JCAP, 2009, 009
- Binney, J. & Merrifield, M. 1999, Galactic Astronomy (Princeton: Princeton University Press)
- Birnboim, Y., Balberg, S., & Teyssier, R. 2015, MNRAS, 447, 3678
- Bismark, A. 2019, PhD thesis
- Blandford, R. & Eichler, D. 1987, Phys. Rep., 154, 1
- Blasi, P. 2013, A&A Rev., 21, 70
- Boquien, M., Buat, V., & Perret, V. 2014, A&A, 571, A72
- Braun, R., Oosterloo, T. A., Morganti, R., Klein, U., & Beck, R. 2007, A&A, 461, 455
- Bresolin, F., Garnett, D. R., & Kennicutt, Jr., R. C. 2004, ApJ, 615, 228
- Bringmann, T., Depta, P. F., Hufnagel, M., Ruderman, J. T., & Schmidt-Hoberg, K. 2021, Physical Review Letters, 127
- Bringmann, T., Edsjö, T., Gondolo, P., Ullio, P., & Bergström, L. 2018, Journal of Cosmology and Astroparticle Physics, 2018, 033–033
- Bronger, T. 2003, File:Ursa major constellation map.png — Wikipedia, The Free Encyclopedia, https://en.m.wikipedia.org/wiki/File:Ursa_major_constellation_map.png, [Online; accessed 11-February-2025]
- Brown, L. W. 1973, ApJ, 180, 359
- Brussaard, P. J. & van de Hulst, H. C. 1962, Rev. Mod. Phys., 34, 507
- Burkert, A. 1995, ApJ Let., 447, L25
- Caprioli, D., Amato, E., & Blasi, P. 2010, Astroparticle Physics, 33, 307
- Caswell, J. L. & Wills, D. 1967, MNRAS, 135, 231

- Chapman, E. & Jelić, V. 2019, The Cosmic 21-cm Revolution: Charting the first billion years of our Universe, Foregrounds and their mitigation
- Cherenkov Telescope Array Consortium, Acharya, B. S., Agudo, I., et al. 2019, Science with the Cherenkov Telescope Array
- Cheung, C., Elor, G., Hall, L. J., & Kumar, P. 2011, Journal of High Energy Physics, 2011, 42
- Chyży, K. T., Jurusik, W., Piotrowska, J., et al. 2018, A&A, 619, A36
- Cid Fernandes, R., Mateus, A., Sodré, L., Stasinska, G., & Gomes, J. M. 2011, STARLIGHT: Spectral Synthesis Code, Astrophysics Source Code Library, record ascl:1108.006
- Clowe, D., Bradač, M., Gonzalez, A. H., et al. 2006, ApJ Let., 648, L109
- Colafrancesco, S., Profumo, S., & Ullio, P. 2006, A&A, 455, 21
- Colafrancesco, S., Profumo, S., & Ullio, P. 2007, Phys. Rev. D, 75, 023513
- Colafrancesco, S., Regis, M., Marchegiani, P., et al. 2015, in Advancing Astrophysics with the Square Kilometre Array (AASKA14), 100
- Collins Dictionary of Astronomy. 2006, synchrotron emission. (n.d.), <https://encyclopedia2.thefreedictionary.com/synchrotron+emission>, [Online; accessed 25-February-2025]
- Colombo, D., Meidt, S. E., Schinnerer, E., et al. 2014, ApJ, 784, 4
- Condon, J. J. 1992, Ann. Rev. A&A, 30, 575
- Condon, J. J., Cotton, W. D., & Broderick, J. J. 2002, AJ, 124, 675
- Condon, J. J., Cotton, W. D., Greisen, E. W., et al. 1998, AJ, 115, 1693
- Condon, J. J. & Ransom, S. M. 2016, Essential Radio Astronomy
- Conway, J. E., Elitzur, M., & Parra, R. 2018, ApJ, 865, 70
- Cook, R. H. W., Seymour, N., Spekkens, K., et al. 2020, Monthly Notices of the Royal Astronomical Society, 494, 135
- Cornwell, T. J. & Perley, R. A. 1992, A&A, 261, 353
- Corwin, H. G. 1995, NED Team Report, 1, 1
- Cotton, W. D. 2017, PASP, 129, 094501
- Cox, D. P. 2005, Ann. Rev. A&A, 43, 337
- Crocker, R. M., Bell, N. F., Balázs, C., & Jones, D. I. 2010, , 81, 063516
- de Gasperin, F., Dijkema, T. J., Drabent, A., et al. 2019, A&A, 622, A5
- de Gasperin, F., Edler, H. W., Williams, W. L., et al. 2023, A&A, 673, A165
- de Gasperin, F., Williams, W. L., Best, P., et al. 2021, A&A, 648, A104

7 Bibliography

- de Jong, M. L. 1965, *ApJ*, 142, 1333
- de Jong, T., Chu, S., & Dalgarno, A. 1975, *ApJ*, 199, 69
- de Jong, T., Klein, U., Wielebinski, R., & Wunderlich, E. 1985, *A&A*, 147, L6
- de La Beaujardière, O., Kazés, I., Le Squeren, A. M., & Nguyen-Quang-Rieu. 1968, *Annales d'Astrophysique*, 31, 387
- de Vaucouleurs, G., de Vaucouleurs, A., Corwin, Herold G., J., et al. 1991, *Third Reference Catalogue of Bright Galaxies*
- Deeg, H.-J., Duric, N., & Brinks, E. 1997, *A&A*, 323, 323
- Delhaize, J., Smolčić, V., Delvecchio, I., et al. 2017, *A&A*, 602, A4
- Delos, M. S. & White, S. D. M. 2023, *JCAP*, 2023, 008
- Dénes, H., Hess, K. M., Adams, E. A. K., et al. 2022, *A&A*, 667, A40
- Dettmar, R. J. 1992, *Fundamentals of Cosmic Physics*, 15, 143
- DMLimit Plotter. SuperCDMS, <https://supercdms.slac.stanford.edu/science-results/dark-matter-limit-plotter>
- Dodorico, S., Rosa, M., & Wampler, E. J. 1983, *A&A Suppl. Ser.*, 53, 97
- Dopita, M. A., Pereira, M., Kewley, L. J., & Capaccioli, M. 2002, *ApJ Suppl.*, 143, 47
- Draine, B. T. 2011, *Physics of the Interstellar and Intergalactic Medium*
- Drukier, A. & Stodolsky, L. 1984, *Phys. Rev. D*, 30, 2295
- Durrer, R. & Neronov, A. 2013, *A&A Rev.*, 21, 62
- Edler, H. W., Roberts, I. D., Boselli, A., et al. 2024, *A&A*, 683, A149
- Einasto, J. & Haud, U. 1989, *A&A*, 223, 89
- Elia, D., Molinari, S., Schisano, E., et al. 2022, *ApJ*, 941, 162
- Ensslin, T. A., Biermann, P. L., Klein, U., & Kohle, S. 1998, *A&A*, 332, 395
- Erceg, A., Jelić, V., Haverkorn, M., et al. 2022, *A&A*, 663, A7
- Erceg, A., Jelić, V., Haverkorn, M., et al. 2024, *A&A*, 688, A200
- Fabbrichesi, M., Gabrielli, E., & Lanfranchi, G. 2021, *The Physics of the Dark Photon*
- Farnes, J. S., Green, D. A., & Kantharia, N. G. 2013, *arXiv e-prints*, arXiv:1309.4646
- Federrath, C. 2015, *MNRAS*, 450, 4035
- Finkbeiner, D. P. & Weiner, N. 2007, *Phys. Rev. D*, 76, 083519

- Fletcher, A. 2010, in *Astronomical Society of the Pacific Conference Series*, Vol. 438, *The Dynamic Interstellar Medium: A Celebration of the Canadian Galactic Plane Survey*, ed. R. Kothes, T. L. Landecker, & A. G. Willis, 197
- Fletcher, A., Beck, R., Shukurov, A., Berkhuijsen, E. M., & Horellou, C. 2011, *MNRAS*, 412, 2396
- Förster Schreiber, N. M., Genzel, R., Lutz, D., & Sternberg, A. 2003, *ApJ*, 599, 193
- Gaisser, T. K., Engel, R., & Resconi, E. 2016, *Cosmic Rays and Particle Physics*
- Gajović, L., Adebahr, B., Basu, A., et al. 2024, *A&A*, 689, A68
- Gajović, L., Heesen, V., Brüggem, M., et al. 2025, arXiv e-prints, arXiv:2502.08713
- Gajović, L., Welzmüller, F., Heesen, V., et al. 2023, *A&A*, 673, A108
- Gaskins, J. M. 2016, *Contemporary Physics*, 57, 496
- Geringer-Sameth, A., Koushiappas, S. M., & Walker, M. 2015, *ApJ*, 801, 74
- Ghisellini, G., Guilbert, P. W., & Svensson, R. 1988, *ApJ Let.*, 334, L5
- Gioia, I. M., Gregorini, L., & Klein, U. 1982, *A&A*, 116, 164
- Gómez-Vargas, G. A., Cuoco, A., Linden, T., et al. 2014, *Nuclear Instruments and Methods in Physics Research A*, 742, 149
- Gómez-Vargas, G. A., Sánchez-Conde, M. A., Huh, J.-H., et al. 2013, *JCAP*, 2013, 029
- González Delgado, R. M. & Pérez, E. 1997, *ApJ Suppl.*, 108, 199
- González-Lópezlira, R. A., Pflamm-Altenburg, J., & Kroupa, P. 2013, *ApJ*, 770, 85
- Gordon, K. D., Engelbracht, C. W., Rieke, G. H., et al. 2008, *ApJ*, 682, 336
- Gould, R. J. 1975, *ApJ*, 196, 689
- Graeve, R., Klein, U., & Wielebinski, R. 1990, *A&A*, 238, 39
- Green, D. A. 2014, *Bulletin of the Astronomical Society of India*, 42, 47
- Griest, K. 1991, *ApJ*, 366, 412
- Groeneveld, C., van Weeren, R. J., Miley, G. K., et al. 2022, *A&A*, 658, A9
- Gupta, Y., Ajithkumar, B., Kale, H. S., et al. 2017, *Current Science*, 113, 707
- Haffner, L. M., Dettmar, R. J., Beckman, J. E., et al. 2009, *Reviews of Modern Physics*, 81, 969
- Hales, S. E. G., Waldram, E. M., Rees, N., & Warner, P. J. 1995, *MNRAS*, 274, 447
- Hall, L. J., Jedamzik, K., March-Russell, J., & West, S. M. 2010, *Journal of High Energy Physics*, 2010, 80
- Han, J. L. 2017, *Ann. Rev. A&A*, 55, 111

7 Bibliography

- Hanasz, M., Lesch, H., Naab, T., et al. 2013, *ApJ Let.*, 777, L38
- Hawking, S. 1971, *Monthly Notices of the Royal Astronomical Society*, 152, 75
- Heald, G. 2015, in *Astrophysics and Space Science Library*, Vol. 407, *Magnetic Fields in Diffuse Media*, ed. A. Lazarian, E. M. de Gouveia Dal Pino, & C. Melioli, 41
- Heesen, V. 2021, *Ap&SS*, 366, 117
- Heesen, V. & Brügger, M. 2021, *Phys. Rev. D*, 103, 048301
- Heesen, V., Buie, E., I., Huff, C. J., et al. 2019, *A&A*, 622, A8
- Heesen, V., de Gasperin, F., Schulz, S., et al. 2023, *A&A*, 672, A21
- Heesen, V., Rafferty, D. A., Horneffer, A., et al. 2018, *Monthly Notices of the Royal Astronomical Society*, 476, 1756
- Heesen, V., Schulz, S., Brügger, M., et al. 2024a, *A&A*, 682, A83
- Heesen, V., Staffehl, M., Basu, A., et al. 2022, *A&A*, 664, A83
- Heesen, V., Wiegert, T., Irwin, J., et al. 2024b, *A&A*, 691, A273
- Heiles, C. & Haverkorn, M. 2012, *SSR*, 166, 293
- Helou, G., Soifer, B. T., & Rowan-Robinson, M. 1985, *ApJ Let.*, 298, L7
- Hindson, L., Kitchener, G., Brinks, E., et al. 2018, *ApJ Suppl.*, 234, 29
- Hinshaw, G., Larson, D., Komatsu, E., et al. 2013, *ApJ Suppl.*, 208, 19
- Hippelein, H. H. 1986, *A&A*, 160, 374
- Hiramatsu, D., Tsuna, D., Berger, E., et al. 2023, *ApJ Let.*, 955, L8
- Hitschfeld, M., Kramer, C., Schuster, K. F., Garcia-Burillo, S., & Stutzki, J. 2009, *A&A*, 495, 795
- Hodge, P. W. 1969, *ApJ Suppl.*, 18, 73
- Hodge, P. W., Gurwell, M., Goldader, J. D., & Kennicutt, Robert C., J. 1990, *ApJ Suppl.*, 73, 661
- Hofmann, W. & Hinton, J. A. 2020, *Cosmic Particle Accelerators*, ed. S. Myers & H. Schopper (Cham: Springer International Publishing), 827–863
- Holschneider, M., Kronland-Martinet, R., Morlet, J., & Tchamitchian, P. 1989, *Proceedings of the International Conference*
- Hoof, S., Geringer-Sameth, A., & Trotta, R. 2020, *Journal of Cosmology and Astroparticle Physics*, 2020, 012
- Hooper, D., Kelso, C., & Queiroz, F. S. 2013, *Astroparticle Physics*, 46, 55
- Hoopes, C. G., Walterbos, R. A. M., & Bothun, G. D. 2001, *ApJ*, 559, 878
- Hryczuk, A. & Laletin, M. 2021, *Journal of High Energy Physics*, 2021, 26

- Hu, N., Wang, E., Lin, Z., et al. 2018, *ApJ*, 854, 68
- Hu, T., Shao, Z., & Peng, Q. 2013, *ApJ Let.*, 762, L27
- Hu, W., Barkana, R., & Gruzinov, A. 2000, *Phys. Rev. Let.*, 85, 1158
- Hummel, E. 1980, *A&A Suppl. Ser.*, 41, 151
- Hummel, E. 1991, *A&A*, 251, 442
- Hütten, M. & Kerszberg, D. 2022, TeV Dark Matter searches in the extragalactic gamma-ray sky
- Ibarra, A. 2015, *Nuclear and Particle Physics Proceedings*, 267-269, 323
- Ibata, R. A., Wyse, R. F. G., Gilmore, G., Irwin, M. J., & Suntzeff, N. B. 1997, *The Astronomical Journal*, 113, 634
- Ignesti, A., Vulcani, B., Poggianti, B. M., et al. 2022, *ApJ*, 924, 64
- Intema, H. T. 2014, in *Astronomical Society of India Conference Series*, Vol. 13, *Astronomical Society of India Conference Series*, 469
- Intema, H. T., Jagannathan, P., Mooley, K. P., & Frail, D. A. 2017, *A&A*, 598, A78
- Intema, H. T., van der Tol, S., Cotton, W. D., et al. 2009, *A&A*, 501, 1185
- Ishibashi, W. & Courvoisier, T. J. L. 2011, *A&A*, 525, A118
- Israel, F. P., Goss, W. M., & Allen, R. J. 1975, *A&A*, 40, 421
- Israel, F. P. & Kennicutt, R. C. 1980, *Astrophysical Letters*, 21, 1
- Israel, F. P. & Mahoney, M. J. 1990, *ApJ*, 352, 30
- Jaeckel, J. & Ringwald, A. 2010, *Annual Review of Nuclear and Particle Science*, 60, 405
- Jelić, V., de Bruyn, A. G., Pandey, V. N., et al. 2015, *A&A*, 583, A137
- Johnston-Hollitt, M., Govoni, F., Beck, R., et al. 2015, in *Advancing Astrophysics with the Square Kilometre Array (AASKA14)*, 92
- Jungman, G., Kamionkowski, M., & Griest, K. 1996, *Physics Reports*, 267, 195–373
- Kapahi, V. K. & Ananthakrishnan, S. 1995, *Bulletin of the Astronomical Society of India*, 23, 265
- Kapińska, A. D., Staveley-Smith, L., Crocker, R., et al. 2017, *ApJ*, 838, 68
- Karachentsev, I., Lebedev, V., & Shcherbanovski, A. 1985, *Bulletin d'Information du Centre de Données Stellaires*, 29, 87
- Kennicutt, R., Armus, L., Bendo, G., et al. 2003a, *PASP*, 115, 928
- Kennicutt, R. C., Bresolin, F., & Garnett, D. R. 2003b, *ApJ*, 591, 801
- Kennicutt, R. C. & Evans, N. J. 2012, *Ann. Rev. A&A*, 50, 531

7 Bibliography

- Kennicutt, R. C., Hao, C.-N., Calzetti, D., et al. 2009, *ApJ*, 703, 1672
- Kennicutt, Jr., R. C. 1998, *Ann. Rev. A&A*, 36, 189
- Kennicutt, Jr., R. C. & Hodge, P. W. 1986, *ApJ*, 306, 130
- Kim, J. E. 1987, *Phys. Rep.*, 150, 1
- Klein, U. & Fletcher, A. 2015, *Galactic and Intergalactic Magnetic Fields*
- Klein, U., Lisenfeld, U., & Verley, S. 2018, *A&A*, 611, A55
- Klein, U., Wielebinski, R., & Morsi, H. W. 1988, *A&A*, 190, 41
- Knapen, J. H. 1998, *MNRAS*, 297, 255
- Kolmogorov, A. N., Levin, V., Hunt, J. C. R., Phillips, O. M., & Williams, D. 1991, *Proceedings of the Royal Society of London. Series A: Mathematical and Physical Sciences*, 434, 9
- Konar, C., Hardcastle, M. J., Jamrozy, M., & Croston, J. H. 2013, *MNRAS*, 430, 2137
- Korsmeier, M. & Cuoco, A. 2016, *Phys. Rev. D*, 94, 123019
- Kramer, E. D., Kuflik, E., Levi, N., Outmezguine, N. J., & Ruderman, J. T. 2021, *Phys. Rev. Lett.*, 126, 081802
- Kuril'Chik, V. N. 1966, *SOVAST*, 10, 1
- Kutkin, A. M., Oosterloo, T. A., Morganti, R., et al. 2023, *A&A*, 676, A37
- Kuźniak, M. 2023, *arXiv e-prints*, arXiv:2312.10828
- Lacki, B. C. 2013, *MNRAS*, 431, 3003
- Lacki, B. C. 2014, *MNRAS*, 444, L39
- Lacki, B. C., Thompson, T. A., & Quataert, E. 2010, *ApJ*, 717, 1
- Lal, D. V., Lyskova, N., Zhang, C., et al. 2022, *ApJ*, 934, 170
- Lane, W. M., Cotton, W. D., Helmboldt, J. F., & Kassim, N. E. 2012, *Radio Science*, 47, RS0K04
- Lara-López, M. A., Pilyugin, L. S., Zaragoza-Cardiel, J., et al. 2023, *A&A*, 669, A25
- Lara-López, M. A., Zinchenko, I. A., Pilyugin, L. S., et al. 2021, *ApJ*, 906, 42
- Lavis, N., Sarkis, M., Beck, G., & Knowles, K. 2023, , 108, 123536
- Lequeux, J. 2005, *The Interstellar Medium*
- Li, J.-T., Beck, R., Dettmar, R.-J., et al. 2016, *MNRAS*, 456, 1723
- Lisanti, M. 2017, in *Theoretical Advanced Study Institute in Elementary Particle Physics: New Frontiers in Fields and Strings*, 399–446
- Lisenfeld, U. & Völk, H. J. 2000, *A&A*, 354, 423

- Longair, M. S. 2011, *High Energy Astrophysics*, Cambridge University Press, 3rd Edition, chapter 19
- Maggio, C. 2021, PhD thesis, Barcelona, Autònoma U.
- MAGIC Collaboration. 2016, *JCAP*, 2016, 039
- Markevitch, M., Gonzalez, A. H., Clowe, D., et al. 2004, *ApJ*, 606, 819
- Martin, N. F., de Jong, J. T. A., & Rix, H.-W. 2008, *ApJ*, 684, 1075
- Martín-Hernández, N. L., van der Hulst, J. M., & Tielens, A. G. G. M. 2003, *A&A*, 407, 957
- Marvil, J., Owen, F., & Eilek, J. 2015, *AJ*, 149, 32
- Massey, R., Kitching, T., & Richard, J. 2010, *Reports on Progress in Physics*, 73, 086901
- McDaniel, A., Jeltema, T., Profumo, S., & Storm, E. 2017, *Journal of Cosmology and Astroparticle Physics*, 2017, 027
- McGaugh, S. S. 2015, *Canadian Journal of Physics*, 93, 250
- McQuinn, K. B. W., Skillman, E. D., Dolphin, A. E., Berg, D., & Kennicutt, R. 2016, *ApJ*, 826, 21
- Meyer, M., Robotham, A., Obreschkow, D., et al. 2017, *PASA*, 34, 52
- Milgrom, M. 1983, *ApJ*, 270, 365
- Mo, H., van den Bosch, F. C., & White, S. 2010, *Galaxy Formation and Evolution*
- Mulcahy, D. D., Fletcher, A., Beck, R., Mitra, D., & Scaife, A. M. M. 2016, *A&A*, 592, A123
- Mulcahy, D. D., Horneffer, A., Beck, R., et al. 2014, *A&A*, 568, A74
- Mulcahy, D. D., Horneffer, A., Beck, R., et al. 2018, *A&A*, 615, A98
- Murphy, E. J. 2009, *The Astrophysical Journal*, 706, 482
- Murphy, E. J., Helou, G., Braun, R., et al. 2006, *ApJ Let.*, 651, L111
- Murphy, E. J., Porter, T. A., Moskalenko, I. V., Helou, G., & Strong, A. W. 2012, *ApJ*, 750, 126
- NASA, ESA, & STScI. 2005, Out of This Whirl: the Whirlpool Galaxy (M51) and Companion Galaxy, <https://hubblesite.org/contents/media/images/2005/12/1677-Image.html>, [Online; accessed 11-February-2025]
- NASA, ESA, & STScI. 2009, Hubble Image of M101, <https://hubblesite.org/contents/media/images/2009/07/2477-Image.html>, [Online; accessed 11-February-2025]
- Navarro, J. F., Frenk, C. S., & White, S. D. M. 1997, *ApJ*, 490, 493–508
- Nieuwenhuizen, T. M. 2017, *Fortschritte der Physik*, 65, 201600050
- Niklas, S. 1995, PhD thesis
- Niklas, S., Klein, U., & Wielebinski, R. 1997, *A&A*, 322, 19

7 Bibliography

- Offringa, A. R., McKinley, B., Hurley-Walker, N., et al. 2014, MNRAS, 444, 606
- Offringa, A. R. & Smirnov, O. 2017, MNRAS, 471, 301
- Oosterloo, T. A., Vedantham, H. K., Kutkin, A. M., et al. 2020, A&A, 641, L4
- Paczynski, B. 1986, ApJ, 304, 1
- Pagel, B. E. J., Edmunds, M. G., Blackwell, D. E., Chun, M. S., & Smith, G. 1979, MNRAS, 189, 95
- Pasini, T., Edler, H. W., Brügggen, M., et al. 2022, A&A, 663, A105
- Peccei, R. D. & Quinn, H. R. 1977a, Phys. Rev. D, 16, 1791
- Peccei, R. D. & Quinn, H. R. 1977b, Phys. Rev. Lett., 38, 1440
- Penny, S. J., Conselice, C. J., De Rijcke, S., & Held, E. V. 2009, Astronomische Nachrichten, 330, 991
- Perley, R. A. & Butler, B. J. 2013, ApJ Suppl., 204, 19
- Perley, R. A. & Butler, B. J. 2017, ApJ Suppl., 230, 7
- Petit, H., Hua, C. T., Bersier, D., & Courtes, G. 1996, A&A, 309, 446
- Planck Collaboration, Ade, P. A. R., Aghanim, N., et al. 2016a, A&A, 586, A138
- Planck Collaboration, Ade, P. A. R., Aghanim, N., et al. 2016b, A&A, 594, A19
- Poggianti, B. M. & Barbaro, G. 1997, A&A, 325, 1025
- Pohl, M. & Schlickeiser, R. 1990, A&A, 239, 424
- Pohl, M., Schlickeiser, R., & Hummel, E. 1991a, A&A, 250, 302
- Pohl, M., Schlickeiser, R., & Lesch, H. 1991b, A&A, 252, 493
- Rafferty, D. and Mohan, N. 2019, PyBDSF 1.10.2 Documentation, <https://pybdsf.readthedocs.io/en/latest/>, Last accessed on 22.03.2023
- Ramírez-Olivencia, N., Varenus, E., Pérez-Torres, M., et al. 2022, A&A, 658, A4
- Read, J. I. & Trentham, N. 2005, Philosophical Transactions of the Royal Society of London Series A, 363, 2693
- Regis, M., Colafrancesco, S., Profumo, S., et al. 2014, Journal of Cosmology and Astroparticle Physics, 2014, 016–016
- Regis, M., Korsmeier, M., Bernardi, G., et al. 2023, JCAP, 2023, 030
- Regis, M., Reynoso-Cordova, J., Filipović, M. D., et al. 2021, Journal of Cosmology and Astroparticle Physics, 2021, 046
- Regis, M., Richter, L., Colafrancesco, S., et al. 2015, Monthly Notices of the Royal Astronomical Society, 448, 3747–3765

- Reynolds, R. J. 2004, *Advances in Space Research*, 34, 27
- Rishbeth, H. 1958, *MNRAS*, 118, 591
- Roberts, I. D., van Weeren, R. J., Lal, D. V., et al. 2024, *A&A*, 683, A11
- Rogstad, D. H. & Shostak, G. S. 1971, *A&A*, 13, 99
- Roy, S. & Pramesh Rao, A. 2006, in *Journal of Physics Conference Series*, Vol. 54, 156–160
- Roy, S. & Rao, A. P. 2004, *MNRAS*, 349, L25
- Rubin, V. C. & Ford, W. Kent, J. 1970, *ApJ*, 159, 379
- Rybicki, G. B. & Lightman, A. P. 1986, *Radiative Processes in Astrophysics*, 2nd edn. (London: John Wiley & Sons, Ltd), 1–50
- Ryle, M., Smith, F. G., & Elsmore, B. 1950, *MNRAS*, 110, 508
- Sabatini, G., Bovino, S., Giannetti, A., et al. 2021, *A&A*, 652, A71
- Sánchez-Conde, M. A., Cannoni, M., Zandanel, F., Gómez, M. E., & Prada, F. 2011, *Journal of Cosmology and Astroparticle Physics*, 2011, 011
- Sandage, A. & Binggeli, B. 1984, *AJ*, 89, 919
- Sanglard, V., Benoit, A., Bergé, L., et al. 2005, *Phys. Rev. D*, 71, 122002
- Santoro, F., Kreckel, K., Belfiore, F., et al. 2022, *A&A*, 658, A188
- Sault, R. J., Teuben, P. J., & Wright, M. C. H. 1995, in *Astronomical Society of the Pacific Conference Series*, Vol. 77, *Astronomical Data Analysis Software and Systems IV*, ed. R. A. Shaw, H. E. Payne, & J. J. E. Hayes, 433
- Schlafly, E. F. & Finkbeiner, D. P. 2011, *ApJ*, 737, 103
- Schleicher, D. R. G., Banerjee, R., Sur, S., et al. 2010, *A&A*, 522, A115
- Schuster, K. F., Kramer, C., Hitschfeld, M., Garcia-Burillo, S., & Mookerjee, B. 2007, *A&A*, 461, 143
- Shimwell, T. W., Hardcastle, M. J., Tasse, C., et al. 2022, *A&A*, 659, A1
- Shimwell, T. W., Röttgering, H. J. A., Best, P. N., et al. 2017, *A&A*, 598, A104
- Shimwell, T. W., Tasse, C., Hardcastle, M. J., et al. 2019, *A&A*, 622, A1
- Sigl, G. 2017, *Astroparticle Physics: Theory and Phenomenology*, 1st edn. (Atlantis Studies in Astroparticle Physics and Cosmology)
- Skillman, E. D. & Israel, F. P. 1988, *A&A*, 203, 226
- Spergel, D. N., Verde, L., Peiris, H. V., et al. 2003, *ApJ Suppl.*, 148, 175
- Stasińska, G., Collin-Souffrin, S., Joly, M., & Alloin, D. 1981, *A&A*, 93, 362

7 Bibliography

- Steer, D. G., Dewdney, P. E., & Ito, M. R. 1984, *A&A*, 137, 159
- Steigman, G., Dasgupta, B., & Beacom, J. F. 2012, *Physical Review D*, 86
- Stein, M., Heesen, V., Dettmar, R. J., et al. 2023, *A&A*, 670, A158
- Storm, E., Jeltama, T. E., Splettstoesser, M., & Profumo, S. 2017, *ApJ*, 839, 33
- Strigari, L. E. 2018, *Reports on Progress in Physics*, 81, 056901
- Strigari, L. E., Bullock, J. S., Kaplinghat, M., et al. 2008, *Nature*, 454, 1096
- Strömgren, B. 1939, *ApJ*, 89, 526
- Swarup, G., Ananthakrishnan, S., Kapahi, V. K., et al. 1991, *Current Science*, 60, 95
- Tabatabaei, F. S., Schinnerer, E., Krause, M., et al. 2017, *ApJ*, 836, 185
- Tabatabaei, F. S., Schinnerer, E., Murphy, E. J., et al. 2013, *A&A*, 552, A19
- Tadhunter, C. 2016, *A&A Rev.*, 24, 10
- Tasse, C. 2014, *A&A*, 566, A127
- Tasse, C., Hugo, B., Mirmont, M., et al. 2018, *A&A*, 611, A87
- Terlouw, J. P. & Vogelaar, M. G. R. 2015, Kapteyn Package, version 2.3, Kapteyn Astronomical Institute, Groningen, available from <http://www.astro.rug.nl/software/kapteyn/>
- Thompson, T. A., Quataert, E., Waxman, E., Murray, N., & Martin, C. L. 2006, *The Astrophysical Journal*, 645, 186
- Tingay, S. J. & de Kool, M. 2003, *AJ*, 126, 723
- Tremblin, P., Anderson, L. D., Didelon, P., et al. 2014, *A&A*, 568, A4
- van Cappellen, W. A., Oosterloo, T. A., Verheijen, M. A. W., et al. 2022, *A&A*, 658, A146
- van der Kruit, P. C. 1977, *A&A*, 59, 359
- van Diepen, G., Dijkema, T., & Offringa, A. 2018, DPPP: Default Pre-Processing Pipeline
- van Haarlem, M. P., Wise, M. W., Gunst, A. W., et al. 2013, *A&A*, 556, A2
- van Weeren, R. J., Shimwell, T. W., Botteon, A., et al. 2021, *A&A*, 651, A115
- van Weeren, R. J., Williams, W. L., Hardcastle, M. J., et al. 2016, *ApJ Suppl.*, 223, 2
- Varenius, E., Conway, J. E., Martí-Vidal, I., et al. 2016, *A&A*, 593, A86
- Varenius, E., Conway, J. E., Martí-Vidal, I., et al. 2015, *A&A*, 574, A114
- Venkattu, D., Lundqvist, P., Pérez Torres, M., et al. 2023, *ApJ*, 953, 157
- Viti, S., Bayet, E., Hartquist, T. W., et al. 2013, in *Astrophysics and Space Science Proceedings*, Vol. 34, *Cosmic Rays in Star-Forming Environments*, ed. D. F. Torres & O. Reimer, 7

- Voelk, H. J. 1989, *A&A*, 218, 67
- Voigtländer, P., Kamphuis, P., Marcelin, M., Bomans, D. J., & Dettmar, R. J. 2013, *A&A*, 554, A133
- Vollmann, M. 2021, *Journal of Cosmology and Astroparticle Physics*, 2021, 068
- Vollmann, M., Heesen, V., W. Shimwell, T., et al. 2020, *MNRAS*, 496, 2663
- Vollmann, M., Welzmüller, F., & Gajović, L. 2024, *JCAP*, 2024, 046
- Vorontsov-Vel'Yaminov, B. A. & Arkhipova, V. P. 1962, *Morphological catalogue of galaxies*, C01, 0
- Walter, F., Brinks, E., de Blok, W. J. G., et al. 2008, *AJ*, 136, 2563
- Weinberg, S. 1978, *Phys. Rev. Lett.*, 40, 223
- Werhahn, M., Pfrommer, C., & Girichidis, P. 2021, *MNRAS*, 508, 4072
- Weżgowiec, M., Beck, R., Hanasz, M., et al. 2022, *A&A*, 664, A108
- White, R. L. & Becker, R. H. 1992, *ApJ Suppl.*, 79, 331
- Wiener, J., Zweibel, E. G., & Oh, S. P. 2013, *ApJ*, 767, 87
- Wilczek, F. 1978, *Phys. Rev. Lett.*, 40, 279
- Willman, B., Geha, M., Strader, J., et al. 2011, *The Astronomical Journal*, 142, 128
- Wills, K. A., Pedlar, A., Muxlow, T. W. B., & Wilkinson, P. N. 1997, *MNRAS*, 291, 517
- Yoast-Hull, T. M., Gallagher, J. S., & Zweibel, E. G. 2016, *MNRAS*, 457, L29
- Yun, M. S., Reddy, N. A., & Condon, J. J. 2001, *ApJ*, 554, 803
- Zweibel, E. G. 2013, *Physics of Plasmas*, 20, 055501
- Zwicky, F. 1933, *Helvetica Physica Acta*, 6, 110

7 Bibliography

A Thermal subtraction

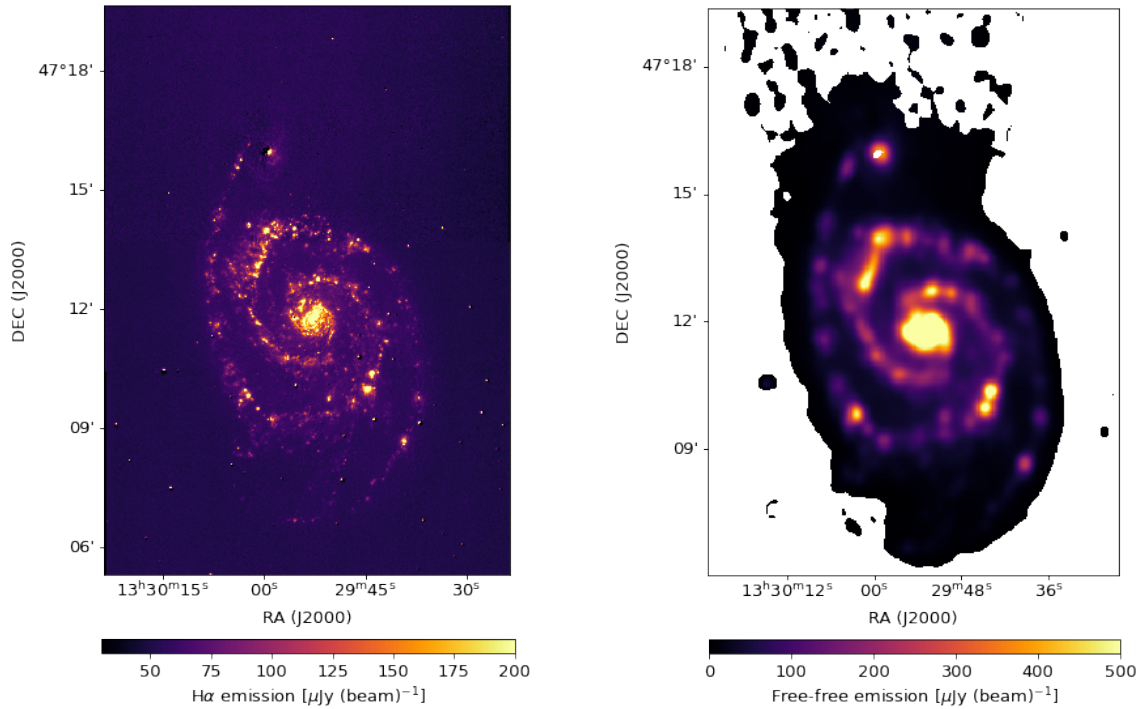


Figure A.1: Intermediate data products in the subtraction of thermal emission in M51. Left panel: Initial continuum-subtracted H α map obtained with the Kitt Peak National Observatory 2.1-m telescope using the narrow-band H α -filter KP1563 (Kennicutt et al. 2003a). The angular resolution is $1''.35 \times 1''.35$ and the rms noise is $\approx 50 \mu\text{Jy beam}^{-1}$. The map was downloaded from the ancillary data at the SINGS webpage.¹ Right panel: Extinction corrected prediction of the free-free emission at 1370 MHz in M51. This emission was scaled to the appropriate frequency with the spectral index $\alpha = 0.1$. The map shown here was subtracted from the radio maps to get the non-thermal emission. The beam size is $17''.5 \times 15''.0$.

¹<http://irsa.ipac.caltech.edu/data/SPITZER/SINGS/>

A Thermal subtraction

B Point spectra

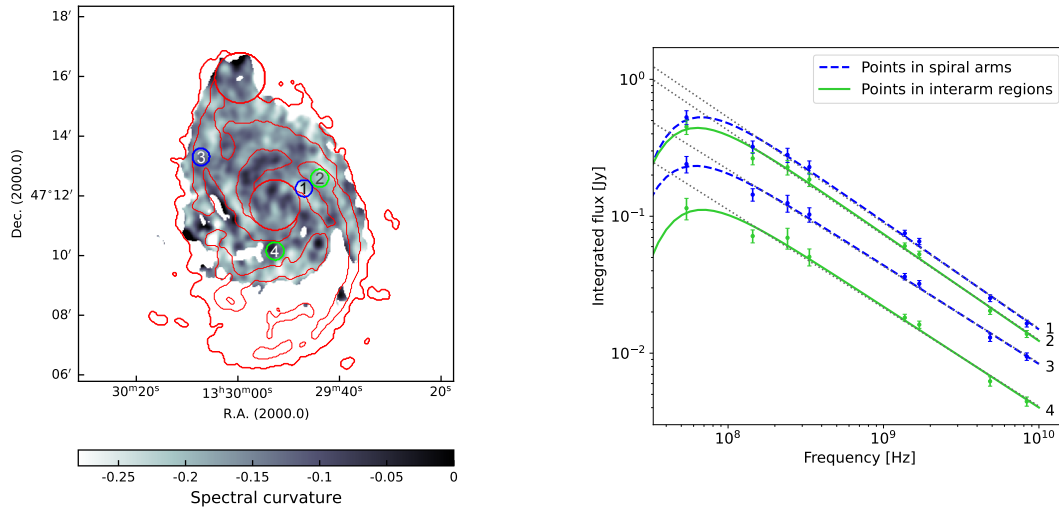


Figure B.1: Individual point spectra. Left panel: The location of individual spectra from spiral arms (inter-arm regions) marked by green (blue) circles on top of the spectral curvature map. The size of the circles corresponds to the beam size. Red contours at the total gas-mass density of 8 and 25 $M_{\odot} \text{pc}^{-2}$ define the borders of the spiral arm and inter-arm regions, respectively (Sect. 2.3.3). Right panel: Non-thermal radio continuum spectra for representative beam-sized regions marked in the left panel. Each spectrum is labelled with its corresponding number. Dotted lines show the power-law fits for frequencies ≥ 144 MHz. The individual spectra show the same trends as the integrated spectra in Fig. 2.9.

B Point spectra

C Mask for the integrated spectrum

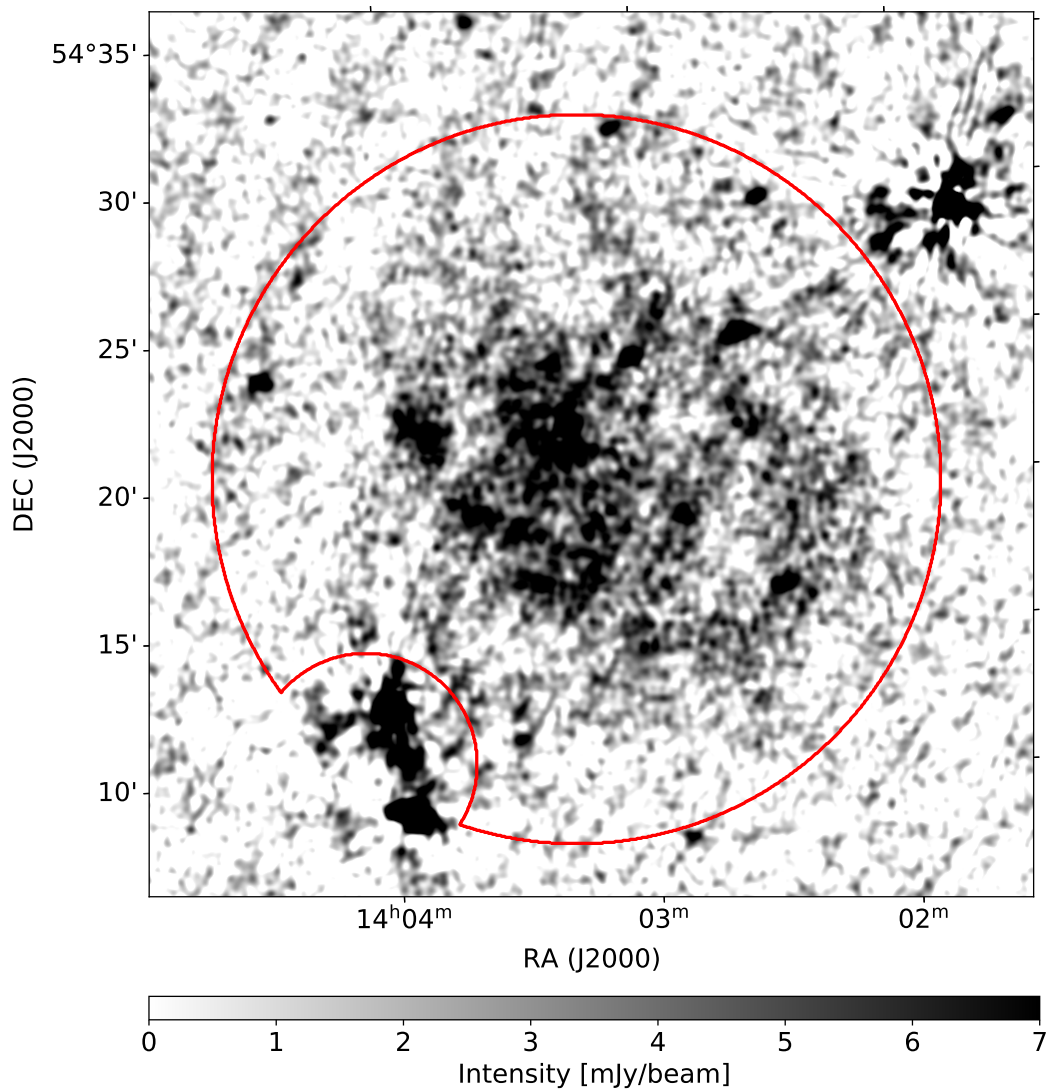


Figure C.1: The region in which we calculated the integrated spectrum of M101. The region is plotted in red on top of the 54 MHz LBA map. The artefacts around background sources are most prominent in the LBA map so we use that map to make sure the artefacts are excluded.

C Mask for the integrated spectrum

D Archival integrated flux density measurements for M 101

Table D.1: Integrated flux density of M 101 from the literature and our observations.

Frequency [MHz]	Flux density [Jy]	Instrument type	Background sources removed	Beam size	Reference
54 ^a	5.02 ± 0.51	Interferometer	+	$26''.5 \times 20''$	1
57	6.5 ± 2.5	Interferometer	-	$7' \times 6'$	2
144 ^a	3.18 ± 0.32	Interferometer	+	$26''.5 \times 20''$	3
178	2.4 ± 0.5	Interferometer	-	$23' \times 18'$	4
610	1.4 ± 0.1	Interferometer	+	$1' \times 1'12''$	5
750	1.3 ± 0.3	Single dish	-	$18'30'' \times 18'30''$	6
920	1.3 ± 0.2	Transit	-	$\sim 8'$ in E-W direction	7
1370 ^a	0.537 ± 0.027	Interferometer	+	$15''.1 \times 11''.0$	1
1400	0.75 ± 0.04	Interferometer	-	$45'' \times 45''$	8
1400	0.81 ± 0.10	Single dish	-	$11'40'' \times 11'40''$	9
1400	0.8 ± 0.1	Interferometer	-	$4' \times 4'$	10
1410	0.82 ± 0.21	Single dish	-	$10' \times 10'$	6
1415	0.85 ± 0.13	Interferometer	-	$4' \times 30'$	11
2700	0.52 ± 0.06	Single dish	+	$\sim 4'30'' \times 4'30''$	12
2700	0.48 ± 0.03	Single dish	+	$4'24'' \times 4'24''$	13
4750	0.335 ± 0.020	Single dish	+	$2'27'' \times 2'27''$	12
4850	0.31 ± 0.02	Single dish	+	$2'30'' \times 2'30''$	13
4850 ^a	0.308 ± 0.015	Combined	+	$30'' \times 30''$	14
10700	0.207 ± 0.020	Single dish	+	$1'30'' \times 1'30''$	12

References: (1) This paper; (2) Israel & Mahoney (1990); (3) Shimwell et al. (2022); (4) Caswell & Wills (1967); (5) Israel et al. (1975); (6) de Jong (1965); (7) Kuril'Chik (1966); (8) Condon et al. (2002); (9) White & Becker (1992); (10) Rogstad & Shostak (1971); (11) de La Beaujardière et al. (1968); (12) Graeve et al. (1990); (13) Berkhuijsen et al. (2016); (14) Weżgowiec et al. (2022).

^(a) Map used in this work.

D Archival integrated flux density measurements for M 101

E Spectral index error map

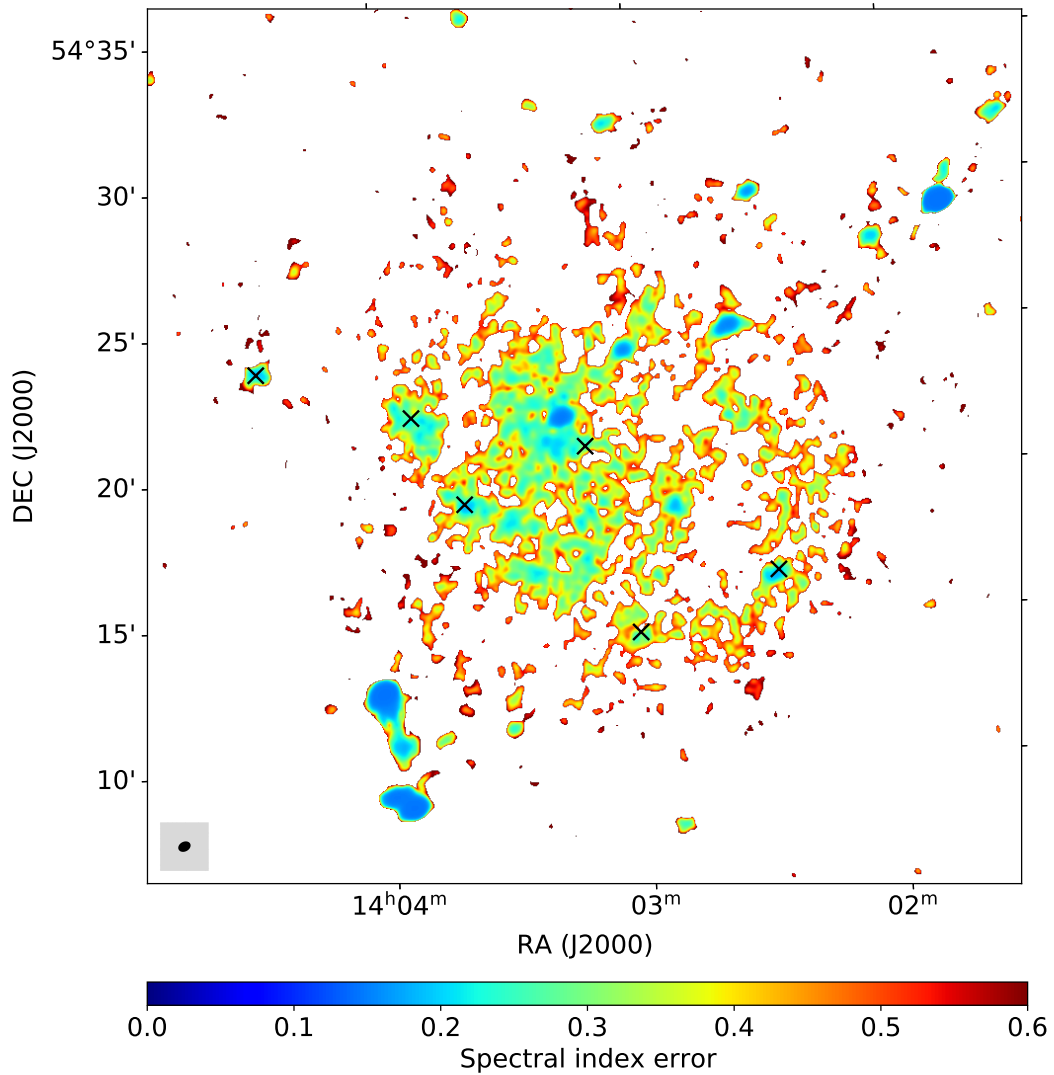


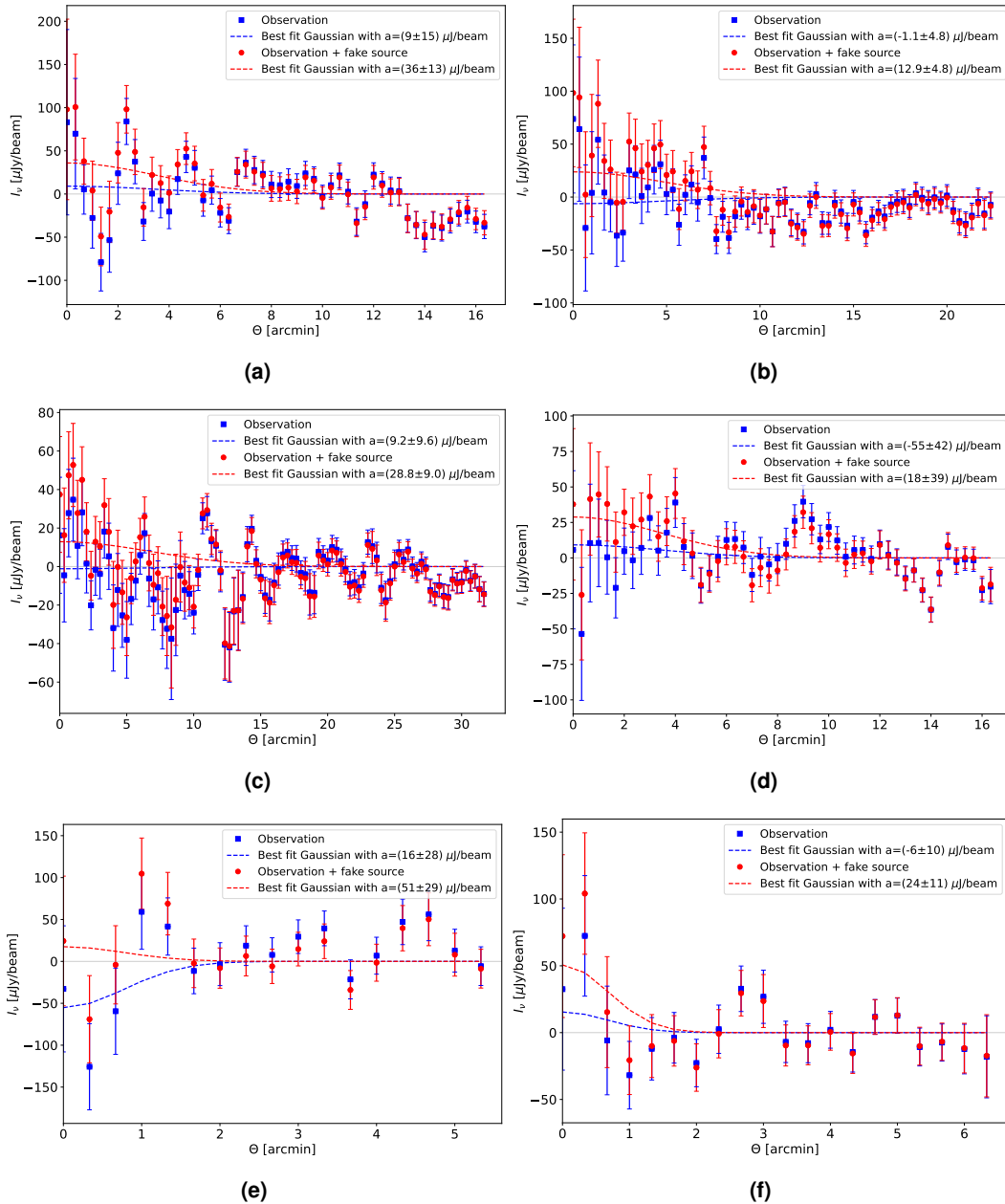
Figure E.1: Spectral index error map between 54 MHz and 144 MHz. White areas below below 2σ are excluded. The beam size is shown with the black ellipse in the bottom left corner. The centres of the studied H II regions are marked with an x to make them easier to find.

E Spectral index error map

F Results for the individual galaxies

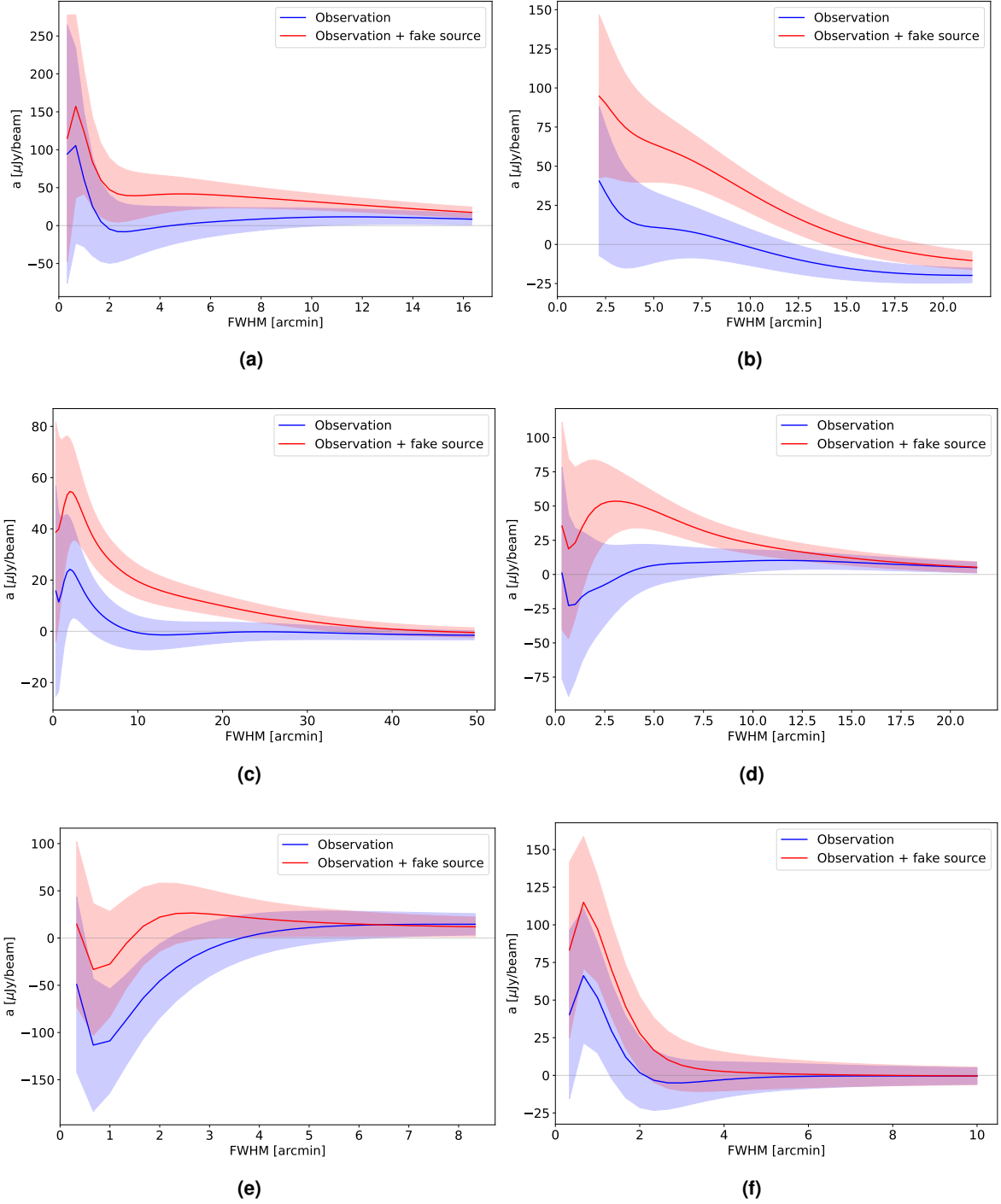
F.1 Radial intensity profiles

Figure F.1: Radial intensity profiles from each of the six dSph galaxies: Canes Venatici I (panel a), Ursa Major I (b), Ursa Major II (c), Ursa Minor (d), Willman I (e), and Canes Venatici II (f). Blue indicates purely observational data, and red indicates data with an additional flux density from a fake source. The individual flux densities are listed in Table 4.2. The dashed lines show the best-fitting Gaussians with a FWHM of r_* . The half-light radii are listed in Table 4.1.



F.2 Fitting plots

Figure F.2: Best-fitting Gaussian amplitudes for the radial intensity profiles in Figs. F.1a- F.1f: Canes Venatici I (panel a), Ursa Major I (b), Ursa Major II (c), Ursa Minor (d), Willman I (e), and Canes Venatici II (f). Blue indicates purely observational data, and red indicates data with an additional fake source. The added individual flux densities are listed in Table 4.2. The shaded areas are 1σ intervals.



G Reimaging parameters

Table G.1: Parameters used to reimage each of the six galaxies.

dSph	Lower uv -cut [λ]	Robustness	Wavelet scale	Baseline-av. factor
CVnI	160	-0.2	564	8.5221
UMaI	60	-0.2	319	5.6113
UMaII	60	-0.2	149	7.0936
UMi	160	-0.2	181	7.0025
WII	400	-0.2	21	5.2477
CVnII	400	-0.2	74	10.3342

G Reimaging parameters

H Stacked limits excluding the galaxy Willman I

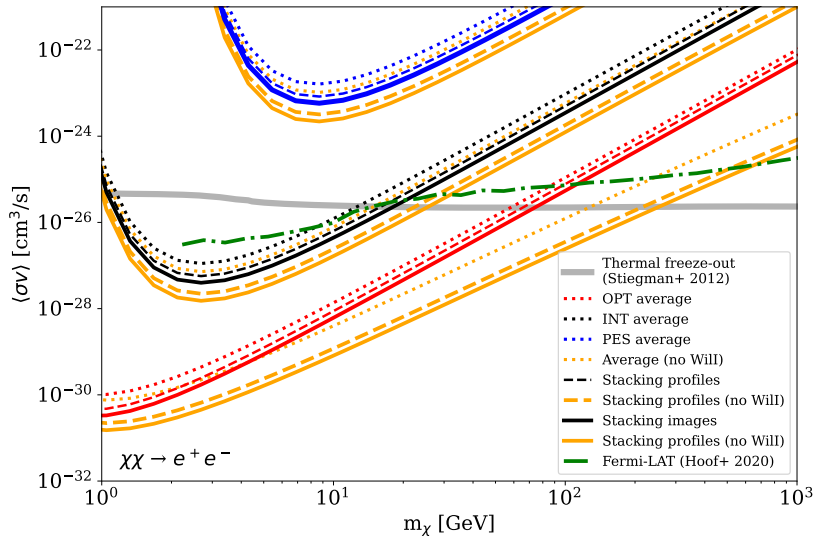


Figure H.1: Upper limits on the WIMP annihilation cross section from stacking without the galaxy Willman I (in orange) compared to the results of stacking all galaxies (colors have the same meaning as in Fig. 4.6).